Cochlea-Inspired Channelizing Filters for Wideband Radio Systems

by

Christopher J. Galbraith

A dissertation submitted in partial fulfillment
of the requirements for the degree of
Doctor of Philosophy
(Electrical Engineering)
in The University of Michigan
2008

Doctoral Committee:
Professor Kamal Sarabandi, Co-Chair
Professor Gabriel M. Rebeiz, Co-Chair, University of California, San Diego
Professor Karl Grosh
Professor Fawwaz T. Ulaby

To my family.

Acknowledgements

The completion of this dissertation would not have been possible without the help and encouragement of many people. First, my advisor Prof. Gabriel Rebeiz is due immense thanks for his role as my teacher and friend. Working for Gabriel provides a student with outstanding resources in the form of state-of-the-art labs, connections to academia and industry, and his own constant technical and moral support. As important, Gabriel provides an environment and training that places paramount importance on producing high quality research and achieving deep technical understanding. I am also thankful to Gabriel for connecting me with so many aspects of the research community. With his support, I have attended conferences and visited research laboratories all over the country, enriching my experience of our profession and inspiring me through exposure to great people and institutions, and their monumental technical achievements.

I also sincerely thank my other committee members for their interest and valuable expertise, time, and effort in advising my dissertation work. Prof. Kamal Sarabandi has been one of my most influential professors, instilling in me the importance of electromagnetics in all realms of electrical engineering and serving as a remarkable example of what one can accomplish when they possess a mastery of both physical concepts and the underlying mathematics. He is also a very generous and gifted teacher. It is an honor for me to have him serve as my committee co-chair. Prof. Karl Grosh has been an invaluable resource in the basic theory and direction of my dissertation research. He has always been eager to offer suggestions and critical advice, and I thank him for all of his support and encouragement. Finally, I thank Prof. Fawwaz Ulaby

for his interest in my work and for serving on my committee. Prof. Ulaby has had a profound influence on my education at Michigan through his example as a leader in research and a world-class educator.

The work in this dissertation got off the ground quickly in large part due to the cochlear modeling work of Prof. Grosh's former students Prof. Rob White and Dr. Lei Cheng. I thank Rob and Lei for their great help and encouragement. In the EECS Department, I thank Beth Stalnaker and Becky Turanski for their expert and always-cheerful help in navigating the graduate program, while keeping my funding and benefits intact. And, I owe many debts to Karla Johnson in the Radiation Laboratory for the continuous help she provides to all of us Radlab students.

The Radiation Laboratory at The University of Michigan is a wonderful place for a graduate student, in large part due to the nice and talented people. I am thankful for my friends there who made research so productive and graduate school life so much more bearable, and often great fun. In particular, former TICS group members Dr. Timothy Hancock, Prof. Kamran Entesari, Prof. Abbas Abbaspour-Tamijani, Dr. Bernhard Schoenlinner, Dr. Bryan Hung, Dr. Tauno Vähä-Heikkilä, Dr. Jad Rizk, and Dr. Andy Brown were outstanding mentors during my first years in graduate school. Of my contemporaries in Gabriel's research group at Michigan, Michael Chang, Carson White, Byung-Wook Min, Sang-June Park, Mohammed El-Tanani, and Alex Grichener have all been excellent companions, classmates, occasional roommates, as well as technical consultants. For the past two years working among Gabriel's new group at the University of California, San Diego, I have been very fortunate to share a sunny office and gorgeous lab with new friends Tiky Yu, Jason May, Dr. Bala Lakshminarayanan, Ramadan Al-Halabi, Dr. Jeong-Geun Kim, Sang-Young Kim, Kwang-Jin Koh, Isak Reines, Berke Cetinoneri, Yusuf Atesal, and Yu-Chin Ou. The new UCSD students are arriving faster than I can name them, but I thank them, too, for being excellent office and lab mates.

It is with great pleasure that I acknowledge my favorite distraction at Michigan: The University of Michigan Amateur Radio Club. Amateur Radio is as old as modern radio itself (the club was first established at Michigan in 1913) and tends to attract radio engineers who just can't get enough hands-on experimentation in their work or school lives. It also attracts non-engineers which, thankfully, makes for a community with wide-ranging interests and expertise and a common fascination with radio. I've had some very fun times at the W8UM "shack" in the EECS building thanks to the other club members including Jon Suen, Richard French, fellow Radlab-er Dr. Lora Schulwitz, and many others. And, I am forever grateful to Dean David Munson, Dean Tony England, Prof. Brian Gilchrist, and Adjunct Professor Bill Becher for their immense support of the club.

Before graduate school, I was fortunate to have two summer internships at TRW Space and Electronics (now Northrop Grumman Space Technology) that sparked my interest in filters and multiplexers, gave me excellent experience in monolithic microwave circuit design, and connected me with a great number of excellent engineers and wonderful people. I thank Sheila Bloodgood and Dr. Cheng-Chih Yang for these memorable and defining opportunities.

I would also like to thank several people at M.I.T. Lincoln Laboratory (MIT-LL) who have given me tremendous support in the last three years of my dissertation work. I am very grateful to Dr. Mark Gouker for supporting our goals and funding much of the cochlear channelizer research. While visiting MIT-LL for design reviews and using their measurement facilities, Rick Drangmeister and Dr. Timothy Hancock were very helpful (a natural extension of Tim's role in his Radlab student years). I also thank Vladimir Bolkhovski for fabricating my circuits in MIT-LL's precision multi-chip module process and Peter Murphy for his precise assembly assistance.

Finally, I thank my family. Early on, they must have known that my peculiar interests might lead to something productive. I thank my Dad for allowing me free

reign of the family house's roof and yards for antenna projects and driving me to radio stores when I was young. And, I thank my Mom who always encouraged me to pursue my passion and education. My brother Rob was also encouraging, despite my routine requests to him (always granted) for help in climbing trees and pruning wire dipoles. More recently, I thank my sister Anne and brother-in-law Felipe who were always up for a drive to Ann Arbor for an Indian dinner, and, again my parents who have always maintained a welcoming house to come home to, especially around the holidays. I am very grateful to have such a loving and supportive family. Without them, I surely would not have had the financial and emotional resources to maintain an extended life as a student.

Chris Galbraith

Ann Arbor, MI

November 12, 2007

Table of Contents

List of Tables

List of Figures

List of Appendices

Appendix

Chapter 1

Introduction

Wireless technology has advanced rapidly in the past 120 years. We have come a long way since the discovery of propagating electromagnetic waves by Maxwell's theoretical genius and the experimental work of Hertz and Tesla, and many others. The broadcast radio, and later, satellite telecommunications industries have provided steady technological development, while the war time and military applications have since fueled astonishing radio engineering advancements in short periods of time. Today, we are very fortunate to have access to a vast amount of well-developed theory. This, combined with modern electronic fabrication methods and materials, makes wireless engineering and technology a very mature, rewarding, and exciting pursuit.

Even with so much progress, problems remain without adequate solutions. Analytical formulations are found for some problems, either due to their simple nature but often by virtue of workers' extremely hard work and uncommon insight. Since computers have become available, many problems that have defied attempts at analytical solution have become solvable through computer-programmed brute force solution or with the assistance of computer aided design (CAD) tools. Even after applying all known theory and available computing resources, some problems persist and call for, at least in part, other means of solution. In this dissertation, one such problem is approached by means of a biological inspiration. In the course of its solution, the theory and practice developed by many people in scientific and engineering disciplines is gratefully used along with computer tools, but, credit for the end product's most

basic structure is due to Nature.

1.1 Motivation: Channelization in Radio Systems

Many commercial and military radio systems depend on channelization, where a signal is subdivided into several signals, each with a smaller bandwidth. This process is also called multiplexing and can be accomplished with a multiplexing filter, or *multiplexer*. Channelization is used in communications systems to allow a receiver, transmitter, or antenna to simultaneously accommodate multiple signals or *channels*. For example, in telecommunications satellite transponders, an input multiplexer is placed at the uplink antenna port in order to channelize the input frequency band before each channel is up- or down-converted, routed via a switch matrix and sent to separate high power amplifiers. Then, the channels are recombined in an output multiplexer that feeds the downlink antenna [1]. Military applications such as electronic support measures (ESM) receivers also require channelization. ESM receivers are used to simultaneously monitor a wide bandwidth and detect and classify signals with a high probability of interception [2, 3]. A typical unit uses a multiplexer at the antenna port to channelize the receiver bandwidth. Then, each channel output feeds a receiver chain and detector whose output provides intercepted signal information to electronic countermeasure (ECM) systems such as jammers [4]. Especially in airborne systems, ESM receiver multiplexing filters must be compact and lightweight [5, 6].

Various wideband receiver system block diagrams are shown in Fig. 1.1. In the scanning superheterodyne receiver, the local oscillator (LO) frequency is swept, giving a wide bandwidth of coverage though instantaneous detection occurs only one narrow, intermediate frequency (IF), bandwidth at a time (Fig. 1.1a). A multi-channel superheterodyne overcomes the narrow-band limitation by placing many receiver front ends in parallel, but whose improvement in instantaneous bandwidth requires a com-

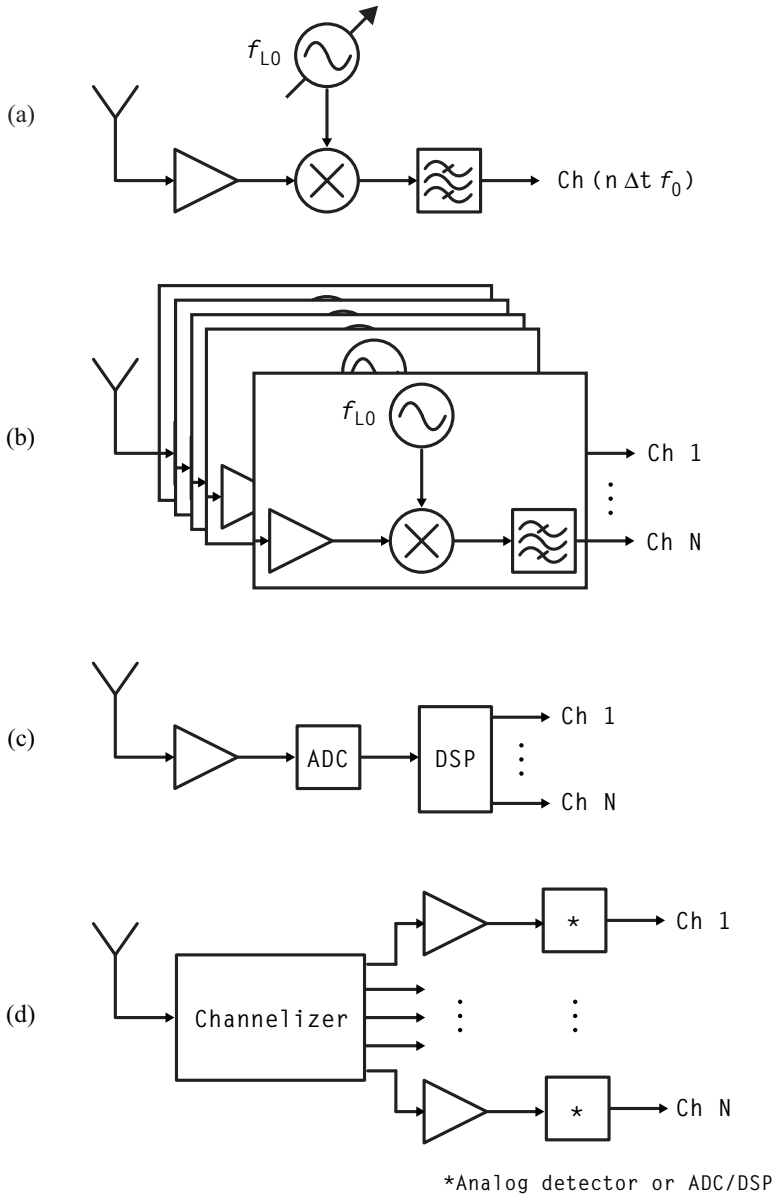

Figure 1.1: Wideband receiver systems: (a) scanning analog superheterodyne, (b) multi-channel analog superheterodyne, (c) wideband digital, and (d) narrow-band analog or digital with analog preselection.

mensurate increase in electronic components and power (Fig. 1.1b). A wideband direct-conversion digital receiver is realized by converting the received signal to the digital domain with an analog to digital converter (ADC) with subsequent channel filtering and detection implemented by digital signal processing (DSP) (Fig. 1.1c). With conventional Nyquist ADCs, such a system's instantaneous bandwidth is less

than one half of the ADC's sampling rate ($f_s/2$) to prevent aliasing [7]. Currently, commercially available ADCs limit a wideband digital receiver's bandwidth to about 1 GHz. Another simultaneous wideband receiver approach uses an analog channelizing filter and either an array of analog receivers or low sampling rate and low-bit ADCs (Fig.1.1d). In the first case, analog detectors on each channel output provide instantaneous spectrum activity monitoring. When each detector is replaced with a relatively low-cost and low-power digital receiver (ADC and DSP chain), this scheme provides simultaneous detection over the entire receiver bandwidth. Using a technique called bandpass sampling, where a signal is down-converted during analog-to-digital conversion, each ADC's sampling rate must only be twice the channel bandwidth (not the entire receiver bandwidth). Also, since the channelizer reduces adjacent-channel interference, the ADC's spurious-free dynamic range (SFDR) requirement, and thus number of required bits, is also significantly reduced [8, 9]. The systems using a front-end channelizing filter promise high receiver performance over a very large bandwidth in a small size and with low cost.

The human auditory system also relies on channelization. The cochlea, located within the inner ear is an amazing audio frequency multiplexing filter. It contains over $3,000$ channels covering a frequency range greater than 1000:1 in a very compact package. The goal of this work is to apply the basic fluid-dynamic cochlear structure to the problem of designing wideband radio frequency (RF) and microwave multiplexers.

1.2 Multiplexers and Channelizers

A multiplexer is an $N+1$ port device, with a common port and N channel ports. The common port can be used as a signal input or output. In the input case, the common port's signal is sub-divided and sent to the channel (output) ports. In the output case, the common port carries the combined signals of all channel (input) ports. In-

put multiplexers are intended for receiver applications and usually low power levels (below 1 W), while output multiplexers are used for transmit applications often in excess of 100 W per channel. Multiplexers with $N = 2$ and $N = 3$ are called diplexers and triplexers, respectively. A duplexer is a diplexer that connects a receiver and transmitter to an antenna at the common port (other duplexers exist that do not use a multiplexer). Multiplexers with adjacent channel passbands are called contiguous, while those with non-channelized frequency bands (called "guard bands") in between channels are called non-contiguous. Input multiplexers with many contiguous channels are often referred to as channelizers due to their usage in channelizer receiver front-ends [4, 10]. Along with other monumental advances in radio and radar engineering, the first modern microwave multiplexers were developed at the M.I.T. Radiation Laboratory during World War II by Fano and Lawson [11, 12]. Since then, multiplexer theory and design has received significant attention and in 2007 remains an important field in radio engineering.

Multiplexers are characterized by their electrical parameters including frequency coverage, input return loss over the covered band, number of channels, whether the channels are contiguous or non-contiguous, channel-to-channel isolation, power handling, and linearity (usually in terms of intermodulation distortion). Individual multiplexer channels are further described by their bandwidth, insertion loss, passband shape, stop-band rejection, and phase response with respect to the common port. Channel properties are closely related to the channel filters. Non-electrical multiplexer characteristics are also important and include physical size and mass, design procedure complexity, post-fabrication tuning requirements, and fabrication cost.

1.2.1 Filter and Multiplexer Technologies

All multiplexer properties are influenced by the technology used where circuits are commonly implemented using waveguide, lumped-element, planar (microstrip,

stripline, coplanar waveguide) and coaxial transmission lines. Waveguide, dielectric resonator, and coaxial-based combline or interdigital types have excellent electrical performance (insertion loss, rejection, isolation, power handling) by virtue of their low-loss, high quality factor (Q, ranging from $1,000$ to $100,000$) resonators but are large, heavy, expensive, and require tuning. In applications that require very small fractional bandwidth channels, low loss, and high power handling, waveguide multiplexers are often the only option. Lumped-element and transmission line multiplexers are small, lightweight, and inexpensive, but have higher insertion loss due to typical resonator Qs of 100 to $1,000$). Superconducting technologies (mainly applied to planar and waveguide types) provide large improvements in electrical performance at a cost of size, mass, cost, and power consumption. In addition, surface acoustic wave (SAW) filters and multiplexers are used when their high insertion loss can be tolerated, and film bulk acoustic wave resonator (FBAR) duplexers have been recently developed for cellular handsets (at $\sim$2 GHz). A summary of widely used filter types and their range of application is shown in Fig. 1.2 (from [13]).

1.2.2 Multiplexer Circuit Topologies

A multiplexer is a collection of separate channel filters and a means of connecting each filter to a common port. The method of connection must also provide a means of tuning out interactions among the individual filters. Without such tuning, the filter responses are altered resulting in distorted channel passbands and poor multiplexer input return loss [14, 15].

The most common multiplexer circuit topologies include common port (series and parallel types), channel dropping, directional filters, and manifold multiplexers (Fig. 1.3).

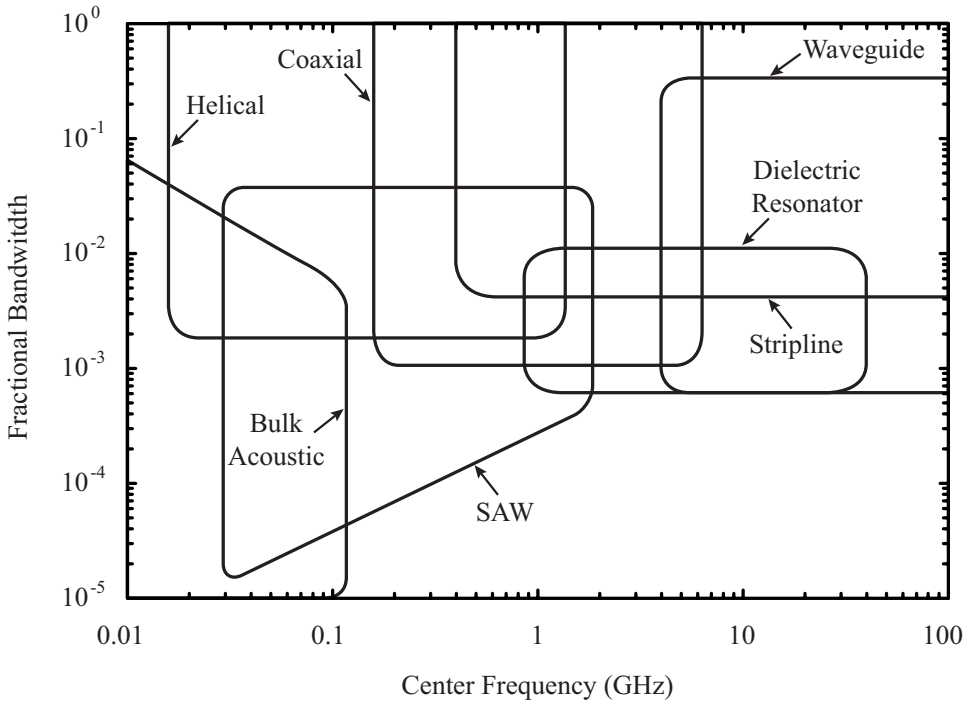

Figure 1.2: Popular filter technologies used in RF and microwave applications, including multiplexers.

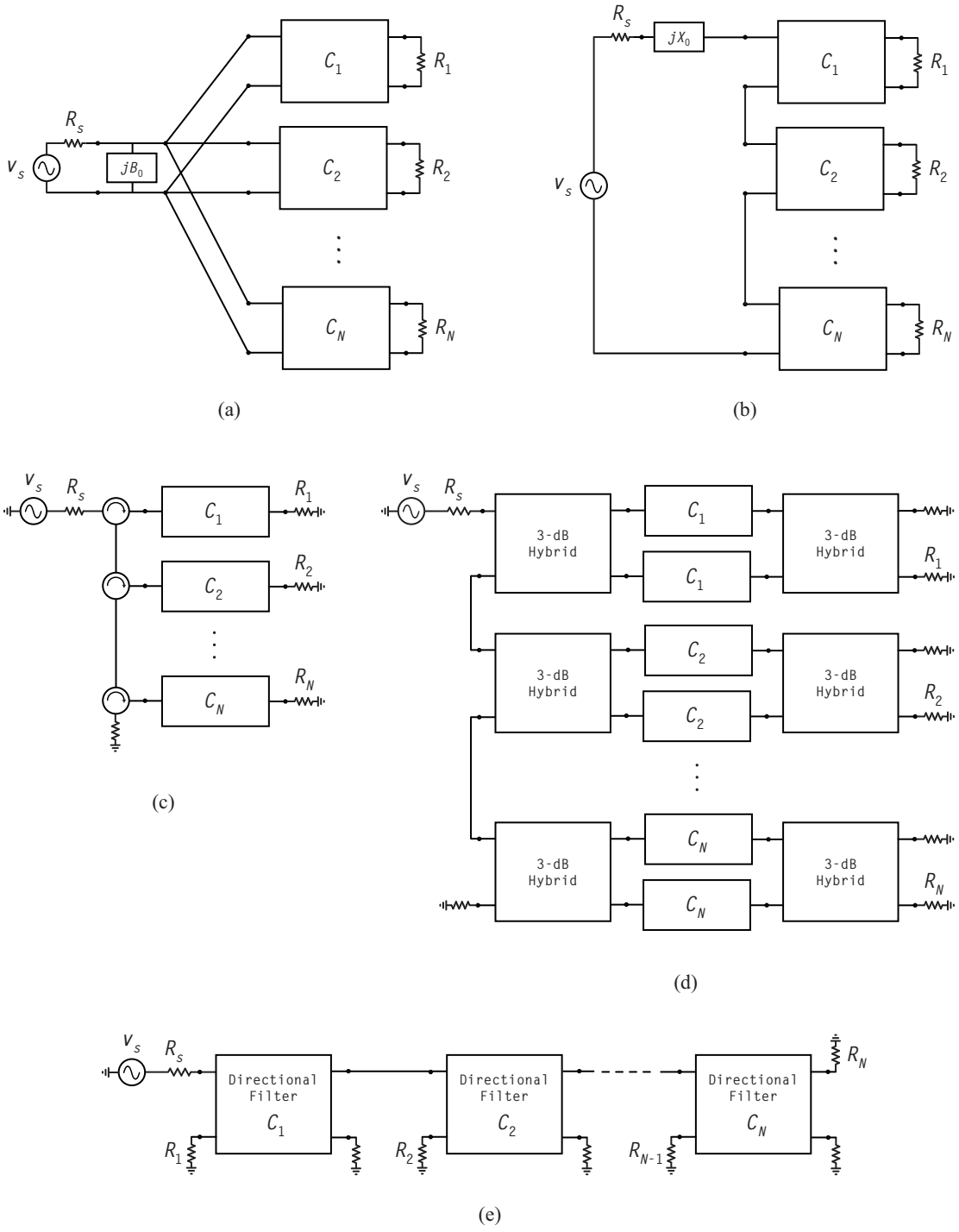

Figure 1.3: Common multiplexer topologies (not including manifold types) used at RF, microwave, and millimeter-wave frequencies: (a) common port parallel, (b) common port series, (c) channel dropping circulator, (d) channel dropping hybrid, and (e) directional filter. Channel filters (C_n) are standard types with the exception of the directional filters used in (e).

Common port types connect all of the channel filters across (parallel) or through (series) a common set of terminals (Figs. 1.3a and 1.3b). Immittance compensation networks are inserted at the common port or the first one or two channel filter resonators are modified to reduce filter interactions [11, 16]. While their simple structure is attractive from a practical standpoint, common port multiplexers are limited to applications with few channels (due to limited connection area at the junction) and require computer optimization [17–20]. Channel dropping architectures use circulators or hybrids (Figs. 1.3c and 1.3d) to isolate and preserve the responses of interconnected channel filters [21, 22]. These types are useful for large numbers of channels due to their modularity, but circulator types require large, heavy, and expensive ferrite components and hybrid types have the largest size of all multiplexers and are very sensitive to process variations [23]. Directional filters are also employed in multiplexers to prevent channel filter interactions (Fig. 1.3e) [24, 25]. While this scheme is useful for the special class of directional filters, most modern filters are non-directional and cannot be used with this technique [11]. Manifold multiplexers are made by interconnecting individual channel filters through a transmission line or lumped network called a *manifold* (Fig. 1.4).

The manifold serves two purposes. First, it physically separates the channel filters. Second, each manifold section produces an impedance transformation from one channel to the next. This transformation, in combination with other immittance compensation networks included in the manifold or filters themselves (such as stubs or irises) is used to prevent interaction among the channel filters. Manifold multiplexers are by far the most popular topology in use today, mostly due to their small size and low loss. Representative examples of manifold multiplexers in the literature using various technologies include waveguide, combline (coaxial type) [14, 15, 26–31], conventional planar and lumped-element [6, 32, 33], and planar and waveguide superconducting versions [5, 34–36].

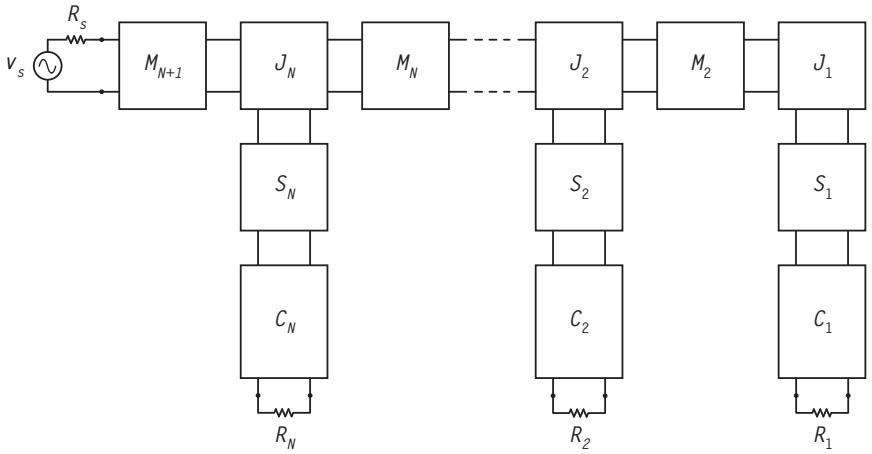

Figure 1.4: The manifold multiplexer topology. Channel filters (C_n) are standard types, while M_n and S_n are transmission line or waveguide sections and J_n are junctions that may also include immittance compensation networks such as stubs or lumped-elements.

1.2.3 Manifold Multiplexer Design and Optimization

Manifold multiplexer design involves synthesizing separate filters for each channel, creating a manifold to interconnect the channels, and optimizing the entire multiplexer using Computer Aided Design (CAD) software. Channel filter design follows standard modern filter synthesis procedures, using either direct-coupled resonator filter theory [17, 37] or synthesis through a coupling matrix and circuit or CAD electromagnetic optimization [38–41]. The manifold is then constructed using the filter technology (e.g. microstrip, waveguide, etc.) and the complete filter-manifold structure is optimized in simulation software [10]. Once designed and built, most non-planar multiplexers require manual tuning.

While the multiplexer design process is relatively simple for 2 to 5 channels, optimization time and circuit complexity increase rapidly when the number of channels is increased. While each section of the manifold varies in length, the average channel-to-channel manifold length is about $\lambda_g/2$ (where λ_g is a guided wavelength). Since the total manifold length increases with additional channels and a longer manifold has increased frequency sensitivity, there exists a limit on the maximum number of channels where optimization of all multiplexer components is not possible [34]. In general, multiplexers more than 10 channels are challenging design problems and often impossible (even with CAD tools) unless the channels are very narrow and the total multiplexer bandwidth is small. One elegant solution for the multi-channel problem is the log-periodic multiplexer of Rauscher which uses an infitite-array prototype to reduce the number of design variables, making optimization of a many channel multiplexer relatively simple [42–44]. However, this scheme still requires optimization and relatively complicated immittance networks between the channel filters.

1.3 Research Goals

This work presents a different approach to planar manifold channelizer design where the channelizer circuit is obtained from an electrical-mechanical analogy of a cochlear model. The electrical circuit's critical characteristic are identified, including channel filter input impedance and manifold structure, and are applied to various technologies, producing several cochlea-like channelizers at frequencies ranging from 20 MHz to 7 GHz (Fig. 1.5). The ultimate outcome is an improved RF cochlea

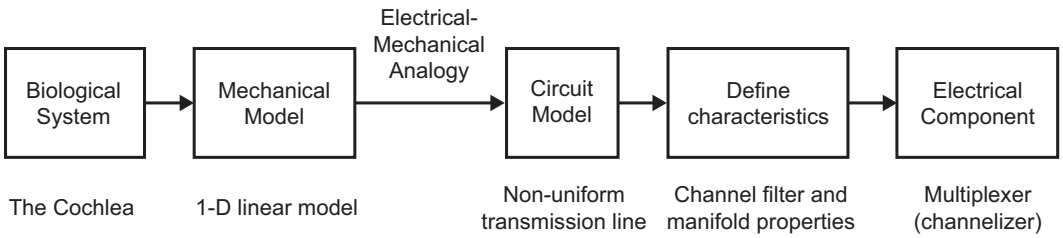

Figure 1.5: Flow of research from biological inspiration to electrical component.

that combines the cochlear circuit structure with higher-order channel filters. These biologically-inspired multiplexers use interactions among channel filters to produce a high-order upper stop-band response, even with single resonator channel filters. The needed channel interaction is provided by a low-value series inductance between adjacent channel filters resulting in a compact physical layout, a simple design procedure, and an unlimited number of channels. Because the channelizers are completely passive, they offer excellent linearity and zero d-c power consumption.

1.4 Dissertation Overview

The dissertation describes the theoretical background and experimental results obtained in creating radio frequency cochleas. Chapter 2 presents a transmission line circuit model of the cochlea derived from applying an electrical-mechanical analogy

to a one-dimensional mechanical cochlea model. Following directly from the transmission line model, Chapter 3 develops the required circuit element relationships and a procedure for designing single-order cochlear channelizers, as well as presents two experimental RF cochleas covering 20 to 90 MHz whose channels possess cochlea-like bandpass responses. Chapter 4 includes the design and results of a planar microwave cochlea channlelizer covering 2 to 7 GHz suitable for an ultra-wideband receiver preselector. In Chapter 5, the theory and design of improved, higher-order cochlear channelizers is given along with a design procedure for and experimental results of a 200 to 1000 MHz version. Finally, Chapter 6 summarizes the work and provides ideas and motivation for future cochlea-like multiplexer work. Appendices are also included with computer codes to assist in cochlear channelizer design, and theory and experiment of microwave planar transformers explored in the course of other dissertation research.

Chapter 2

Cochlear Modeling

2.1 The Mammalian Cochlea

The cochlea is the electro-mechanical transducer located in the inner ear that converts acoustical energy (sound waves) into nerve impulses sent to the brain (Fig. 2.1). The cochlea is an amazing channelizing filter with approximately 3,000 distinct channels covering a three decade frequency range, and can distinguish frequencies which differ by less than 0.5%. [45, 46].

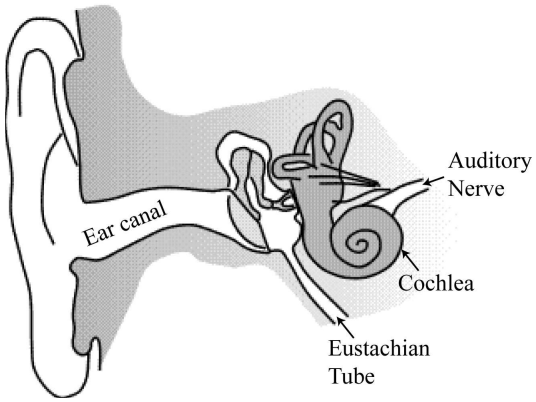

Figure 2.1: The periphery of the human auditory system. The basilar membrane is contained within the cochlea.

The filtering characteristics of the cochlea rely on the propagation of a coupled fluid-structure wave that results in a localized spatial response for each frequency. In the biological cochlea, active processes enhance the frequency response of the system;

we only consider the basic hypothesis for how the passive system works. The structure (the basilar membrane and organ of Corti) can be thought of as a flexible membrane comprised of a series of parallel beams upon which a fluid rests (Fig. 2.2). In the

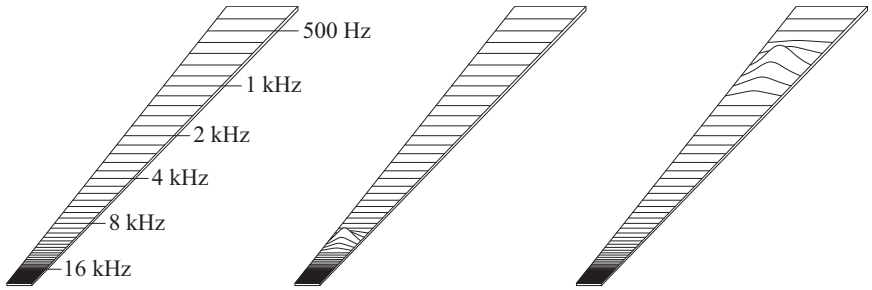

Figure 2.2: (a) The "unwound" basilar membrane acts as a continuum of resonant beams, shown with input signals of (b) high frequency and (c) low frequency.

biological cochlea and in the unwound idealization, acoustic input occurs closest to the narrowest beams at the stapes (or footplate). Other than the stapes and the flexible membrane, the fluid is acoustically trapped. The stapes vibration excites the cochlear fluid which in turn gives rise to a structural acoustic traveling wave down the length of the flexible membrane. Because the resonant frequencies of the flexible membrane are organized from high frequency (where the acoustic information is input) to low frequency, the spatial response of the membrane is frequency selective and spatially organized with the peak of the response occurring at different locations for different frequencies. Specialized cells called inner hair cells are arrayed down the length of the cochlea. These cells rate encode firing of the auditory nerve to the amplitude of the fluid motion [47].

The work presented in this dissertation is the first attempt to create a passive RF channelizing filter using a model derived from cochlear mechanics. Previous efforts on achieving cochlear-like filtering have focused on using VLSI techniques to implement

active circuit realizations of a cochlear-mechanics model at audio frequencies [48],[49]. More recently, high frequency integrated circuit techniques and network synthesis of cochlea-like active filters has been used to extend active cochleas to RF and microwave frequencies [50], [51]. In contrast, the work presented here is passive and uses shunt-connected resonators coupled by series inductors to create a cochlea-like response.

2.2 One-Dimensional Mechanical Model

In the simplest mechanical model of the cochlea, a one-dimensional fluid interacts with a variable impedance locally-reacting structure. The impedance of this structure can be expressed as a function of its mass (m), damping (r), and stiffness (k), where all parameters are functions of position along the structure and are expressed per unit area,

$$Z(x) = j\omega m(x) + r(x) + \frac{k(x)}{j\omega} = \frac{-P(x)}{v_{bm}(x)} \tag{2.1}$$

where $P(x)$ is the fluid pressure immediately above the structure (at $z = 0$) and v_{bm} is the structure velocity. An inviscid, incompressible, one-dimensional fluid model produces a simple relationship between pressure and membrane velocity,

$$\frac{d^2P(x)}{dx^2} = -j\omega\frac{\rho}{H}\, v_{bm}(x) \tag{2.2}$$

where ρ is the fluid density and H is the duct height. Eliminating v_{bm} from (2.1) and (2.2) and rearranging yields an equation for the basilar membrane pressure,

$$\frac{d^2P(x)}{dx^2} + \frac{\dfrac{\rho}{Hk(x)}}{1 + j\omega\dfrac{r(x)}{k(x)} - \omega^2\dfrac{m(x)}{k(x)}}\,\omega^2 P(x) = 0. \tag{2.3}$$

This is a highly dispersive waveguide problem, where the coupled effects of the mechanical membrane and the fluid loading create the dispersion relation. Structural

acoustic waves traveling along the basilar membrane experience a delay relative to the input, with a phase velocity that varies as a function of position as well as frequency. As the traveling wave approaches the resonant section of the membrane, wave velocity decreases rapidly and the wave ceases to propagate. Further, since the membrane properties change slowly with respect to wavelength, little energy is reflected back to the input. In effect, the basilar membrane acts as a dispersive delay line for traveling structural acoustic waves, with a spatially-dependent cutoff frequency.

2.2.1 An Electrical-Mechanical Analogy

The equation of motion in the mechanical domain given by (2.3) can be rewritten in terms of electrical parameters by using a mechanical-electrical analogy. In general, there is a choice regarding the relationship between mechanical and electrical parameters, although several physically meaningful analogies are common. In this case, we replace basilar membrane fluid pressure (P) in the mechanical domain with voltage (V) in the electrical domain:

$$V(x) \longleftrightarrow P(x). \tag{2.4}$$

Other substitutions follow from this choice, including:

$$\begin{aligned} L_2(x) &\longleftrightarrow m(x) \\ C(x) &\longleftrightarrow \frac{1}{k(x)} \\ R(x) &\longleftrightarrow r(x) \\ L_1(x) &\longleftrightarrow \frac{\rho}{H}. \end{aligned} \tag{2.5}$$

The result of this analogy is an equation of motion in the electrical domain given

by

$$\frac{d^2V(x)}{dx^2} + \frac{L_1(x)C(x)}{1 + j\omega R(x)C(x) - \omega^2 L_2(x)C(x)}\,\omega^2\,V(x) = 0 \tag{2.6}$$

where V is the voltage along the transmission line, L_1 and C are the series inductance and shunt capacitance per unit length, $1/R$ is the shunt conductance per unit length, and $1/\omega L_2$ is the shunt inductive susceptance per unit length. For the discrete lumped element model, these lead to component values based on the level of discretization as shown in Fig. 2.3. Note that V, L_1, L_2, C, and R are functions of position along the transmission line.

In the analogy to the mechanical model, the series inductance L_1 plays the role of the fluid coupling while the shunt resonator elements L_2, C, and R play the role of the variable impedance structure. For this model, the variable x describes a normalized

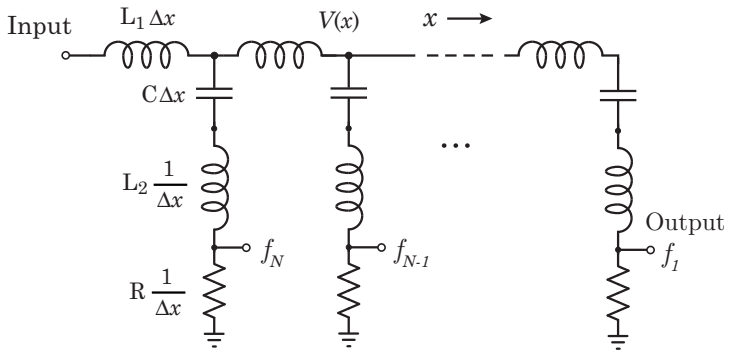

Figure 2.3: Discretized transmission line model of the mammalian cochlea.

position along the circuit, with $x = 0$ corresponding to the circuit input and $x = 1$ referring to the location immediately to the left of the final channelizer section. In terms of channel number n, the channelizer input refers to $n = N$ (highest frequency) while the last channel corresponds to $n = 1$ (lowest frequency), so that

$$x = 1 - \frac{n}{N}, \quad 0 \le x \le 1, \quad 1 \le n \le N.$$

The channelizer operates as a low-pass transmission line structure shunt-loaded

by series-resonator sections. Each resonator appears as a short-circuit at its resonant frequency and an open-circuit off resonance. The highest frequency channel resonator is located *closest* to the input while the lowest frequency channel is located at the end of the transmission line. Since the highest frequency components are removed from the input signal first, the rejection on each channel's upper side is much steeper than on the lower side. This response is characteristic of mammalian cochleas and is demonstrated later in simulated and measured results.

2.2.2 Non-Uniform Transmission Line Theory

One can also arrive at (2.6) through transmission line theory. Considering a small segment of an infinitely long transverse electromagnetic (TEM) wave transmission line of the general form shown in Fig. 2.4 where $Z(x)\Delta x$ is an impedance in series with

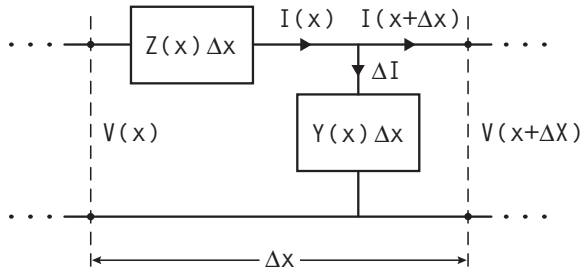

Figure 2.4: Lumped-element segment used to derive the differential equation describing a non-uniform transmission transmission line.

one conductor and $Y(x)\Delta x$ is an admittance in each segment's shunt arm. Writing an expression for the voltage across $Z(x)$,

$$V(x) - IZ(x)\Delta x = V(x + \Delta x) \tag{2.7}$$

and the current through $Y(x)$,

$$I(x) - I(x + \Delta x) = V(x + \Delta x)Y(x)\Delta x \tag{2.8}$$

rearranging and letting the segment's length tend toward zero, recognizing

$$\lim_{\Delta x \to 0} \frac{V(x + \Delta x) - V(x)}{\Delta x} = \frac{dV}{dx} \tag{2.9}$$

$$\lim_{\Delta x \to 0} \frac{I(x + \Delta x) - I(x)}{\Delta x} = \frac{dI}{dx} \tag{2.10}$$

one gets first-order equations for the voltage and current along the non-uniform line,

$$\frac{dV}{dx} + Z(x)I = 0 \tag{2.11}$$

$$\frac{dI}{dx} + Y(x)V = 0. \tag{2.12}$$

Differentiating (2.11) and (2.12) with respect to x and using (2.7) gives second-order equations in only V or I,

$$\frac{d^2V}{dx^2} - \frac{1}{Z}\frac{dZ}{dx}\frac{dV}{dx} - YZV = 0 \tag{2.13}$$

$$\frac{d^2I}{dx^2} - \frac{1}{Y}\frac{dZ}{dx}\frac{dI}{dx} - YZI = 0. \tag{2.14}$$

Using $Z = j\omega L_1(x)$ and $Y = (1/j\omega C + j\omega L_2 + R)^{-1}$ in (2.13) gives (2.6) with one additional term whose value is proportional to the variation of $Z(x)$ with x,

$$\frac{d^2V(x)}{dx^2} - \frac{1}{Z(x)}\frac{dZ}{dx}\frac{dV}{dx} + \frac{L_1(x)C(x)}{1 + j\omega R(x)C(x) - \omega^2 L_2(x)C(x)}\,\omega^2\,V(x) = 0 \tag{2.15}$$

where,

$$\frac{1}{Z(x)}\frac{dZ}{dx} = \frac{1}{j\omega L_1(x)}\frac{d}{dx}\left[j\omega L_1(x)\right]. \tag{2.16}$$

For long discretized transmission lines (and channelizers with many channels) whose sections are exponentially-scaled with length (2.16) tends to be very small (i.e. L_1 changes very slowly with x), though it must be included in (2.15) if one is interested in calculating exact solutions of the non-uniform line [52].

Chapter 3

Single-order RF Cochlear Channelizers

This chapter applies the previously developed transmission line cochlear model to the design of two cochlear channelizing filters covering the 20 to 90 MHz band in 20 contiguous channels. Theory, a design procedure, and results are including for both fractional and constant bandwidth channelizers. In addition, the time-domain behavior of these channelizers is examined.

Applications of these channelizing filters include wideband, contiguous-channel receivers for signal intelligence or spectral analysis. In its simplest form, the channelizing filter is used to decompose a wideband input signal into contiguous channels, whose outputs are then fed to separate amplifiers, mixers, and detectors, providing simultaneous reception over the entire input bandwidth. By using a less complex receiver chain (for instance, an envelope detector) at each filter output, this wideband receiver becomes a spectrum analyzer.

3.1 Channelizer Circuit Design

To arrive at an actual channelizer design, we must choose the element values for the cochlea-like circuit described by (2.6). For this, we rely on earlier modeling efforts for the case of a channelizer whose channels have a constant fractional bandwidth. An alteration of this model allows the design of constant absolute bandwidth filters described later.

3.1.1 Constant Fractional Bandwidth Formulation

In a constant fractional bandwidth channelizing filter, each filter section has the property,

$$\frac{\Delta f}{f_0} \equiv \frac{1}{Q} = \text{constant} \tag{3.1}$$

where f_0 and Δf are the center frequency and bandwidth of a particular channel, and Q is approximately the loaded quality factor of the series resonant circuit channel filter; the channel filter's actual Q is slightly lower due to the loading of adjacent channels. The channel bandwidth definition used in this design is the difference in (upper and lower) passband frequencies where adjacent channel transmission responses cross each other. For a channelizer with constant fractional bandwidth channels, the functional dependence between the coefficients in (2.3) and (2.6) is given by [53] and [54]. Written in terms of the channelizer circuit elements these relations are:

$$L_2(x)C(x) = A_1 e^{\alpha x} \tag{3.2}$$

$$R(x)C(x) = A_2 e^{0.5\alpha x} \tag{3.3}$$

$$L_1(x)C(x) = A_3 e^{\alpha x}. \tag{3.4}$$

Note that (3.2)–(3.4) define an exponential scaling of resonator component values required to implement series resonator channels with a constant fractional bandwidth. In these functions, A_1, A_2, A_3, and α are constants to be determined, while L_1, L_2, C, and R are the desired channelizer circuit elements. Using (3.2), the series resonator branches have a resonant frequency given by,

$$f_0 = \frac{1}{2\pi\sqrt{L_2(x)C(x)}} = \frac{1}{2\pi\sqrt{A_1 e^{\alpha x}}} \tag{3.5}$$

so that their resonant frequencies decrease exponentially as we go from left (input) to right along the channelizer circuit. Also, note that the loaded Q of each series LCR

resonator can be written

$$Q = \frac{X}{R} = \frac{2\pi f_0 L_2}{R} = \frac{1}{R(x)}\sqrt{\frac{L_2(x)}{C(x)}} \tag{3.6}$$

so that by using (3.2) and (3.3) in (3.6), we find that the each resonator has an identical loaded Q, where

$$Q = \frac{\sqrt{A_1}}{A_2}. \tag{3.7}$$

Since the fractional bandwidth of each resonator is just the reciprocal of the loaded Q, the functional dependence of (3.2)–(3.4) results in a channelizer whose channels exhibit a constant fractional bandwidth.

The number of channels N needed can be estimated as a function of the desired total bandwidth with a given channel fractional bandwidth. First, consider two adjacent channels, each crossing over at 2 dB below below each channel's identical maximum transmission value. The two channels' center frequencies are related by

$$f_{n+1} = f_n + \frac{\Delta f_{n+1}}{2} + \frac{\Delta f_n}{2}, \quad 1 \leq n \leq N. \tag{3.8}$$

Using (3.1) to write Δf in terms of fractional bandwidth $(1/Q)$, this becomes

$$\frac{f_{n+1}}{f_n} = \frac{1 + 1/2Q}{1 - 1/2Q}. \tag{3.9}$$

For an N channel channelizer the maximum and minimum frequencies are related by

$$\frac{f_{max}}{f_{min}} = \frac{f_N}{f_1} = \left(\frac{1 + 1/2Q}{1 - 1/2Q}\right)^{N-1} \tag{3.10}$$

and,

$$N = 1 + \frac{\ln\left(\dfrac{f_N}{f_1}\right)}{\ln\left(\dfrac{1 + 1/2Q}{1 - 1/2Q}\right)}. \tag{3.11}$$

Note that since the series resonator channel filters are coupled to and loaded by adjacent resonators, each channel filter's loaded Q is less than that of the isolated series resonator. Consequently, one needs to use a slightly larger value of Q in the design process to produce the desired fractional bandwidth channels. For example, as illustrated later, channels with 8.2% fractional bandwidth ($Q = 12.2$) use resonators with a Q of 15.6 (28% higher). One uses the actual channel filter Q in (3.11).

3.1.2 Determination of Coefficients

The coefficients A_1, A_2, A_3, and α are determined by four design choices, including:

$$\begin{aligned} f_1 &\equiv \text{Lowest channel center frequency} \\ f_N &\equiv \text{Highest channel center frequency} \\ 1/Q &\equiv \text{Channel fractional bandwidth} \\ \theta &\equiv \text{Transmisson phase at each channel's center frequency} \end{aligned}$$

The choice of θ is arbitrary, and its value affects the input impedance and overall channelizer response. The design must therefore be simulated with various θ values until the desired response is achieved. Interestingly, the channelizer exhibits a characteristic S_{11} spiral which moves along the real axis of the Smith Chart as one varies θ from zero to values approaching roughly 2π (Fig. 3.1). The channelizer minimum and maximum channel center frequencies and channel fractional bandwidth are chosen based on the application.

The resonator nearest the channelizer input ($x = 0$) is tuned at the highest frequency (f_N). Using (3.2) with $x = 0$, and (3.5), A_1 is given by

$$A_1 = \frac{1}{(2\pi f_N)^2}. \tag{3.12}$$

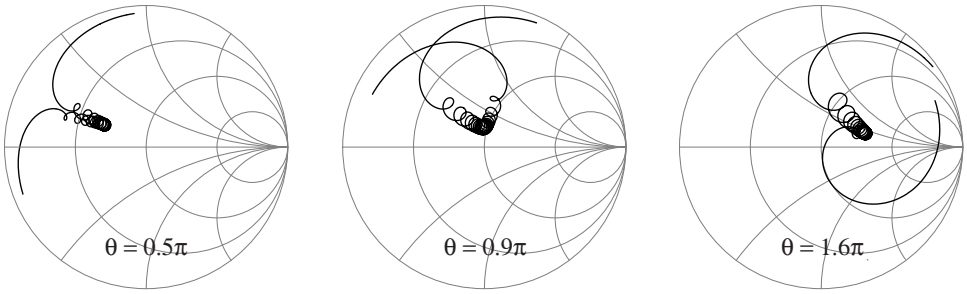

Figure 3.1: Channelizer S_{11} for three values of θ. A θ value of 0.9π (b) produces an input return loss of less than -10 dB over the band from 20–90 MHz. The Smith Chart impedance is 50 Ω.

Next, to determine A_2, one uses the desired channel fractional bandwidth and (3.6) to arrive at

$$A_2 = \frac{\sqrt{A_1}}{Q}. \tag{3.13}$$

To find α, (3.2) and (3.12) are used at the channelizer input ($x = 0$) and final section ($x = 1$) where

$$x = 1 \;\Rightarrow\; A_1 e^{\alpha} = \frac{1}{(2\pi f_1)^2}$$
$$x = 0 \;\Rightarrow\; A_1 = \frac{1}{(2\pi f_N)^2}$$

such that

$$\alpha = \ln\left(\frac{f_N}{f_1}\right)^2. \tag{3.14}$$

Finally, A_3 is found using a numerical technique and the previously determined constants. The Wentzel-Kramers-Brillouin (W.K.B.) approximation suggests that if $g(x)$ changes slowly enough with x, then we can approximate the solution to

$$\frac{d^2}{dx^2}u(x) + g(x) \cdot u(x) = 0 \tag{3.15}$$

at some $x = x_0$ by the solution

$$u(x_0) = U_0 e^{j\int_0^{x_0}\sqrt{g(x)}dx} = U_0 e^{j\theta}. \tag{3.16}$$

Comparing (3.15) with (2.6), we let

$$g(x) = \frac{L_1(x)C(x)}{1 + j\omega R(x)C(x) - \omega^2 L_2(x)C(x)}\,\omega^2$$

and

$$u(x) = V(x).$$

Thus, we can find the phase of (3.16) using

$$\theta \approx \int_0^{x_0} \sqrt{g(x)}\; dx. \tag{3.17}$$

In (3.17), θ is the phase of $u(x)$ at location x_0 which is the location of a resonator with a center frequency f_0. The transmission phase at the center frequency of each resonator θ is assumed to be constant in analogy with physiological cochlear response data [55, 56].

Having found A_1, A_2, and α, and choosing a value of θ, (3.17) is numerically integrated along the channelizer length (x) for each value of x_0. For each point x_0 along x an integral is evaluated and the needed term $L_1(x)C(x)$ is found. The result is an arbitrary function which is then fit to the desired form of (3.4), giving the value of A_3.

Having found the four constants A_1, A_2, A_3, and α, each circuit component of the constant fractional bandwidth channelizer is determined from (3.2)–(3.4). In our designs, the value of $R(x)$ is made constant for each resonator section to ensure a constant impedance at each output port. Therefore, first $C(x)$ is determined from

(3.3), then $L_1(x)$ and $L_2(x)$ are calculated from (3.4) and (3.2).

3.1.3 Constant Absolute Bandwidth Formulation

In many cases, a channelizer filter with a constant absolute bandwidth (Δf) outputs is needed. In this case, the number of channels needed to cover a specified bandwidth is given by

$$N = 1 + \frac{f_N - f_1}{\Delta f}. \tag{3.18}$$

Such a channelizer results from modifying the functional dependence of the channel center frequencies from exponential to linear.

For a constant channel bandwidth, the channel center frequencies are given by

$$f_0 = B_1 + B_2 x. \tag{3.19}$$

Equating this with the resonant frequency of a series LCR resonator results in

$$L_2(x)C(x) = \frac{1}{\left[2\pi\left(B_1 + B_2 x\right)\right]^2}. \tag{3.20}$$

Using (3.19) and (3.20) in (3.6), we obtain

$$R(x)C(x) = \frac{\Delta f}{2\pi\left(B_1 + B_2 x\right)^2}. \tag{3.21}$$

Combining (3.20) and (3.21) leads to,

$$L_2(x) = \frac{R(x)}{2\pi\Delta f} \tag{3.22}$$

and for resonators with identical output impedance ($R(x)$), the resonator inductance value ($L_2(x)$) is also fixed and inversely proportional to the channel bandwidth. Note that this relationship places a practical restriction on the realizable bandwidth of the

constant absolute bandwidth design, for a given channel bandwidth, due to inductor parasitics: the channelizer's maximum frequency must be below the inductor's self-resonant frequency.

Suggested by the form of (3.21), the last relationship among the circuit elements is chosen as

$$L_1(x)C(x) = \frac{1}{\left[2\pi\left(B_3 + B_4 x\right)\right]^2}. \tag{3.23}$$

This was found empirically to result in a channelizer with constant absolute bandwidth channels as well as a good input impedance match over the entire channelizer bandwidth.

3.1.4 Determination of Coefficients

For the channelizer with constant absolute bandwidth channels, the coefficients B_1, B_2, B_3, and B_4 are determined from the chosen values of:

$$\begin{aligned} f_1 &\equiv \text{Lowest channel center frequency} \\ f_N &\equiv \text{Highest channel center frequency} \\ \Delta f &\equiv \text{Channel absolute bandwidth} \\ \theta &\equiv \text{Transmission phase at each channel's center frequency} \end{aligned}$$

Since the highest frequency resonator appears at the channelizer input ($x = 0$), using (3.19) we find that,

$$B_1 = f_N. \tag{3.24}$$

At the lowest frequency resonator ($x = 1$), again using (3.19), we find that

$$B_2 = f_1 - f_N. \tag{3.25}$$

Finally, the constants B_3 and B_4 are determined by using the same numerical integration and curve fitting procedure used in the constant fractional bandwidth design. However, in the constant absolute bandwidth case (3.23) is substituted in the kernel $g(x)$ of (3.17). Again here, the choice of the phase at each center channel (θ) is adjusted by trial-and-error in simulation to optimize channelizer input return loss.

Having found B_1, B_2, B_3, and B_4, the channelizer circuit elements are determined. With $R(x)$ constant, $L_2(x)$ is given by (3.22), $C(x)$ is found using (3.20), and $L_1(x)$ is given by (3.23).

3.2 Experimental Results

Two channelizer prototypes were designed, built, and measured to demonstrate the cochlea-inspired channelizer topology. Each circuit was realized in a modified version of the discretized transmission-line model as shown in Fig. 3.2. As shown

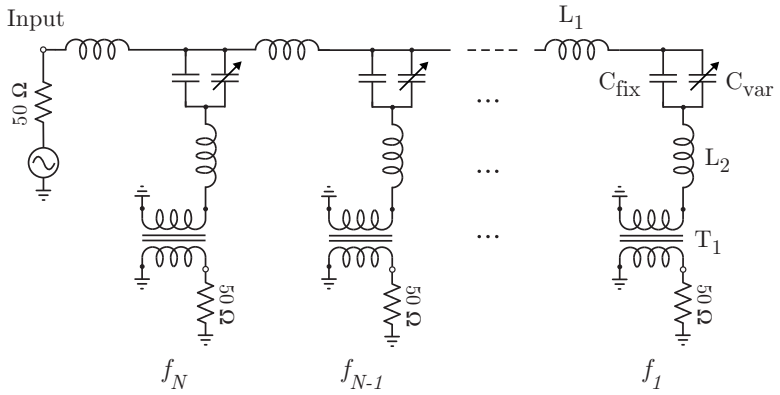

Figure 3.2: Schematic diagram of the channelizer prototypes. In this implementation, the resonator capacitances are formed by the parallel combination of C_{fix} and C_{var} to allow fine tuning.

later in simulated and measured results, this discretization results in ripples in the filter transmission and reflection.

In the first built versions of the channelizer, component and printed circuit board

(PCB) parasitics caused unwanted in-band resonances, emphasizing the need for accurate simulation. For the prototypes presented here, circuit simulations were performed in Agilent ADS [57] using manufacturer provided S-parameters of all lumped components except for the RF transformers. The RF transformer S-parameter blocks were generated from a de-embedded fixture measurement. Board parasitics were accounted for using an S-parameter block derived from a full-wave Sonnet model [58]. The resulting simulations accurately predicted parasitic resonances.

3.2.1 Constant Fractional Bandwidth Channelizer

A 20-channel channelizer with constant fractional bandwidth channels covering 20–90 MHz is shown in Fig. 3.3. The series inductances L_1 are air-wound inductors

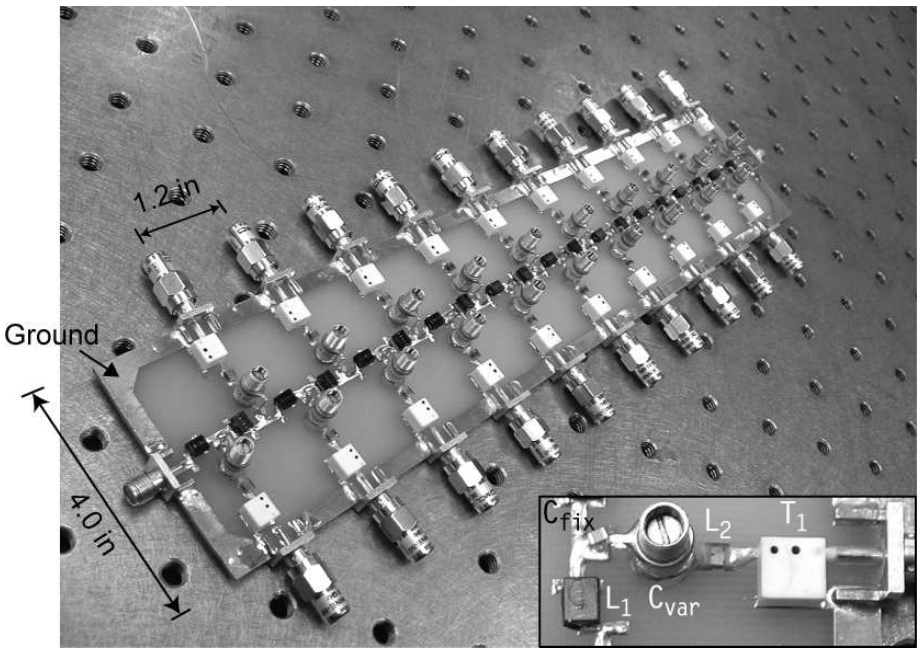

Figure 3.3: Photograph of the 20-channel, 20–90 MHz channelizing filter with constant fractional bandwidth channels. The inset shows a single channel layout.

(Coilcraft Midi Spring) with Q of 60–100 over the channelizer bandwidth. The shunt

resonator sections are designed for a loaded Q of 16 and $|X_L|$=$|X_C|$=200 Ω at resonance, resulting in an effective impedance of 12.5 Ω. This is transformed to 50 Ω through a 1:2 turns ratio RF transformer (Coilcraft TTWB) at each channel output. The shunt resonator inductors L_2 (Coilcraft 0805CS) are ceramic body wire-wound surface-mount components with Q of 25–40 at the channel center frequencies. To take into account the tolerance in the component values and since the capacitors and inductors are commercially available in discrete values, the resonator capacitances C are implemented with the parallel combination of a fixed surface-mount capacitor (ATC 600F) and a coaxial trimmer capacitor (Sprague GAA). The trimmer capacitor was included to ease the tolerance requirement of the other components—a design using all fixed-value components (±2%) is certainly possible. The total capacitor Q is greater than 200 over the channelizer bandwidth. Channelizer component design values range from 30 nH to 37 nH for L_1, 310 nH to 1570 nH for L_2, and 8 pF to 40 pF for C (Fig. 3.4). The circuit is constructed on a 61 mil FR-4 PCB (Fig. 3.3) with the ground located along the perimeter of the PCB to reduce shunt parasitic capacitance. Simulations on two-sided PCB identified significant layout parasitics that gave undesirable spurious responses within the filter pass-band.

3.2.2 Measurements

The channelizer is tuned by adjusting the trimmer capacitors on individual channel resonators until nulls in the measured S_{11} match the simulated response (Fig. 3.5). The tuning procedure involved first setting each trimmer at maximum capacitance, then adjusting for the desired response by lowering the appropriate trimmer value beginning with the highest frequency channel. Channelizer measured and simulated S_{21} for each channel ($S_{(n+1)1}$ for $1 \leq n \leq 20$) are shown in Fig. 3.6. Measured insertion loss at the center of each channel ranges from 2.5 dB to 5.3 dB, with an average of 4.8 dB.

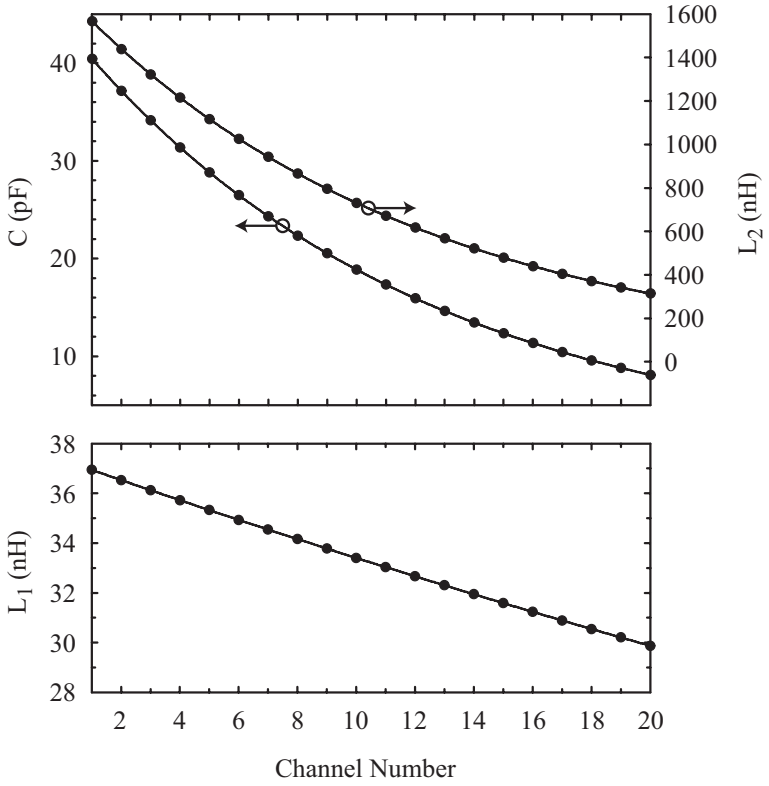

Figure 3.4: Component values for L_1, L_2, and C for the 20–90 MHz constant fractional bandwidth (8%) channelizer.

A sample of three separate channel responses is shown in Fig. 3.7. Focusing on channel 10, we notice the characteristic cochlear response. The pass-band slope is first-order (20 dB/decade) below the channel center frequency and over fifth-order (100 dB/decade) immediately above the channel center frequency due to the low-pass nature of the dispersive transmission-line. Note that for frequencies outside of the channelizer bandwidth, each channel has a characteristic single LCR response. This can be seen as an increase in S_{21} for all channels beginning at both 20 MHz and 90 MHz. Also, the self-resonance of the resonator inductors produces a parasitic resonance at 150 MHz. The measured center frequencies and channel responses match simulation closely. Adjacent channel S_{21} cross at approximately 2 dB below each channel's center frequency (Table 3.1). Each channel's 2-dB crossover bandwidth is 8.2±0.1%. Spurious responses above 100 MHz are due to resonances of the lumped

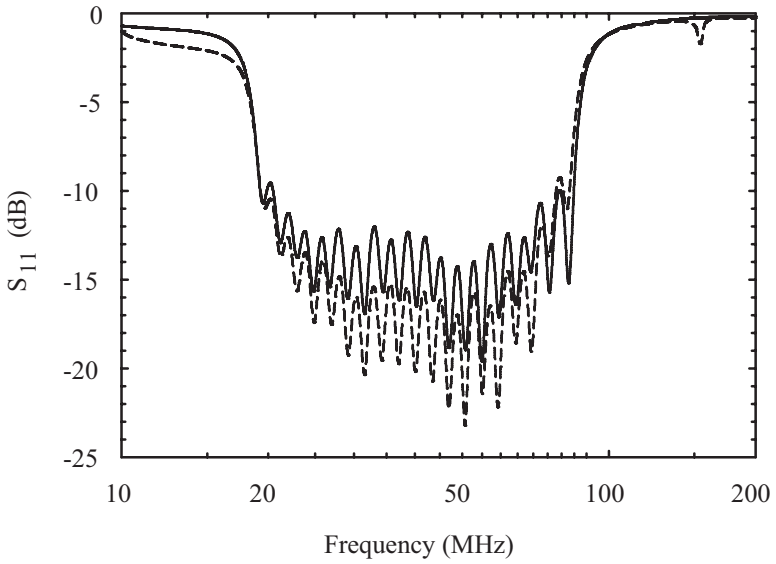

Figure 3.5: Measured (solid) and simulated (dashed) S_{11} of the 20-channel constant fractional bandwidth channelizer.

inductors as well as PCB parasitic shunt capacitance.

Table 3.1: Channelizer Center Frequencies (in MHz)

Ch	f_c	Ch	f_c	Ch	f_c	Ch	f_c
1	19.2	6	28.7	11	42.4	16	62.4
2	20.8	7	31.1	12	46.0	17	67.3
3	22.5	8	33.5	13	49.6	18	72.6
4	24.4	9	36.3	14	53.8	19	78.2
5	26.5	10	39.4	15	58.0	20	84.3

To understand the channelizer loss, consider the power distribution at the center frequency of channel 10 (39.4 MHz) (Table 3.2). The percent of the input power appearing at the individual outputs is calculated from each channel's measured $|S_{21}|^2$. Likewise, the reflected power at the channelizer input is given by $|S_{11}|^2$. At 39.4 MHz, 33.2% of the power arrives at the channel 10 output (-4.8 dB), 32.3% appears at all other channel outputs (Fig. 3.8), and 3.5% is reflected at the channelizer input. Summing the powers results in 69.0% of the input power. Thus, the filter dissipates

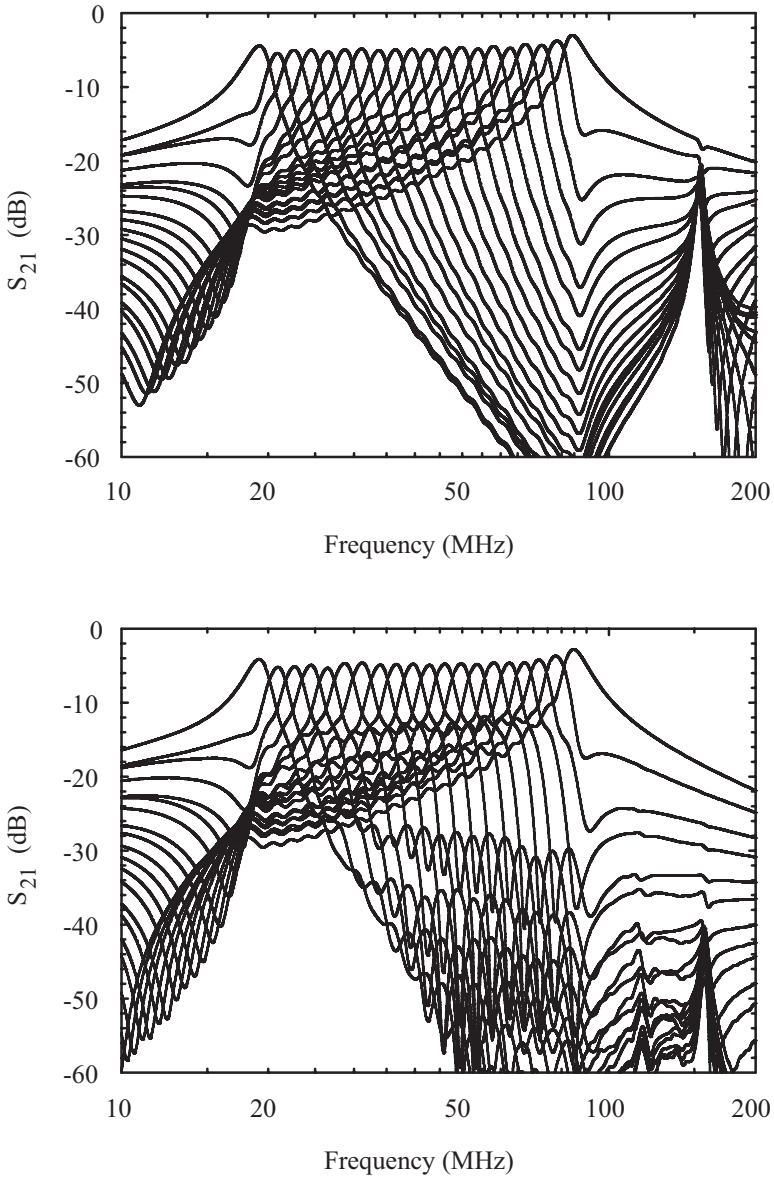

Figure 3.6: Simulated (top) and measured (bottom) S_{21} for each channel of the channelizing filter.

31.0% of the input power corresponding to an effective loss of 1.6 dB.

3.2.3 Constant Absolute Bandwidth Channelizer

The 20-channel channelizer with constant absolute bandwidth channels covering roughly 20–90 MHz is shown in Fig. 3.9. This design also uses high-Q surface-mount

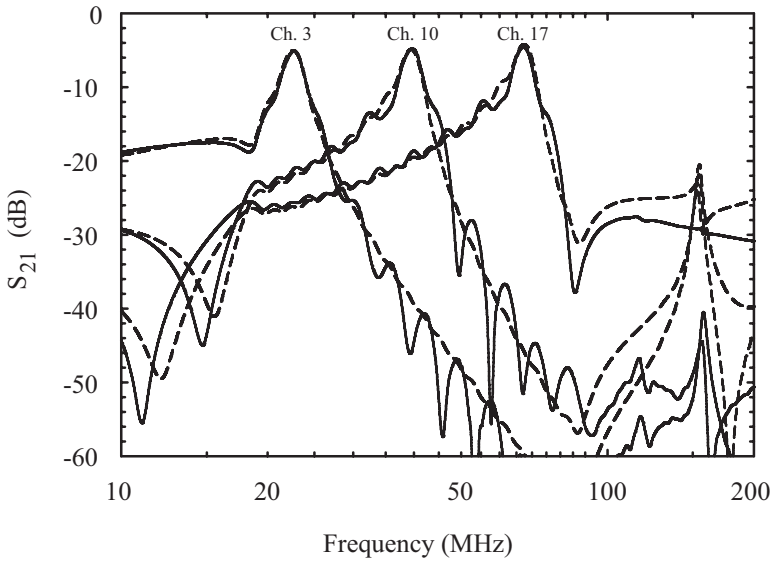

Figure 3.7: Measured (solid) and simulated (dashed) S_{21} of the constant fractional bandwidth channelizer for channels 3 (22.5 MHz), 10 (39.4 MHz), and 17 (67.3 MHz). Ripples are due to parasitics and resonances of the lumped components.

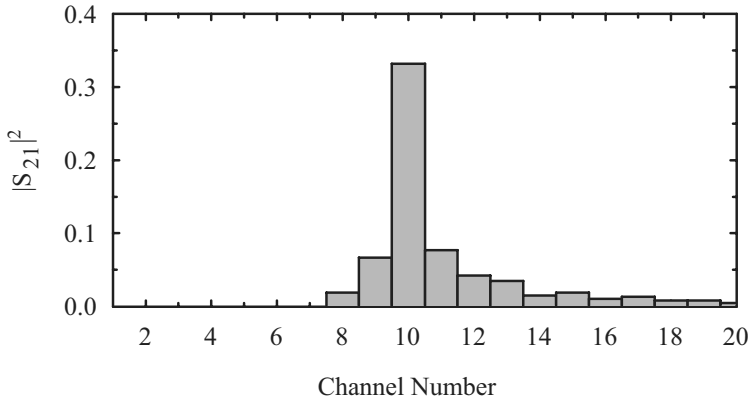

Figure 3.8: Measured power distribution at the center frequency of channel 10 (39.4 MHz) among all 20 channels.

components throughout, with air-coil inductors for both L_1 and L_2 (Coilcraft Midi and Maxi Spring). In contrast to the constant fractional bandwidth case, the individual channel resonators have a loaded Q that varies with resonator center frequency, producing constant absolute channel bandwidth. The resonators are again designed

Table 3.2: Sample Channel Power Distribution for Channel 10

	Power (%)
Channel 10 Output	33.2 (−4.8 dB)
Sum of Channel 1–9, 11–20 Outputs	32.3
Reflected at Input	3.5
Sum of all Power Contributions	69.0
Power Dissipated	31.0

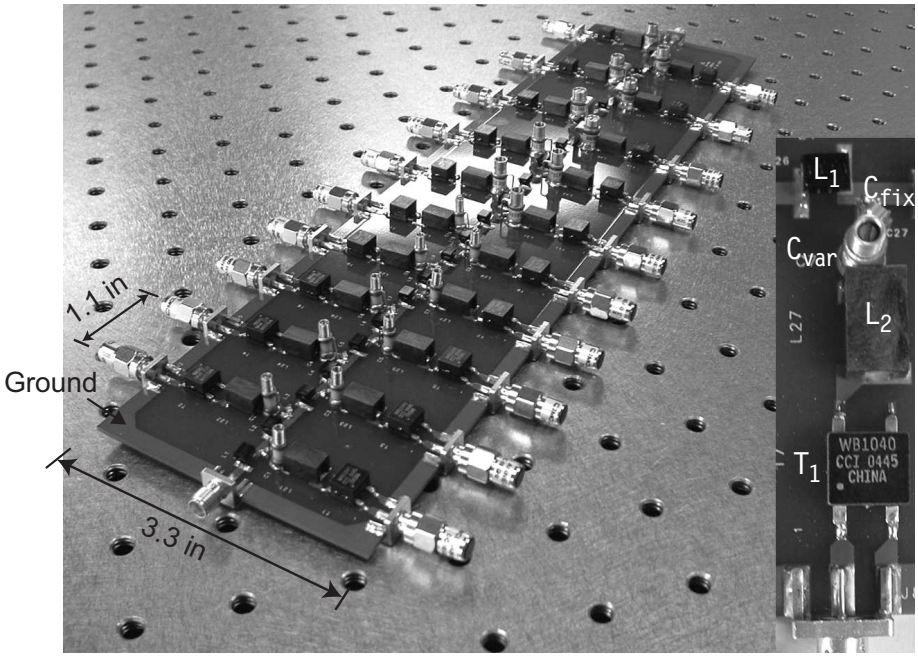

Figure 3.9: Photograph of the 20-channel, 20–90 MHz channelizing filter with constant absolute bandwidth channels. The inset shows a single channel layout.

for a series resistance, at resonance, of 12.5 Ω and 1:2 turns ratio RF transformers (Coilcraft WB1040) are used at each channel output to produce a 50 Ω output impedance. The resonator capacitances C also employ a parallel combination of a fixed capacitor (ATC 600F) and a coaxial trimmer capacitor (Sprague GAA) to allow for fine-tuning channel center frequencies. Channelizer component design values

range from 19 nH to 296 nH for L_1 and 5 pF to 150 pF for C, while L_2 is fixed at 422 nH (Fig. 3.10).

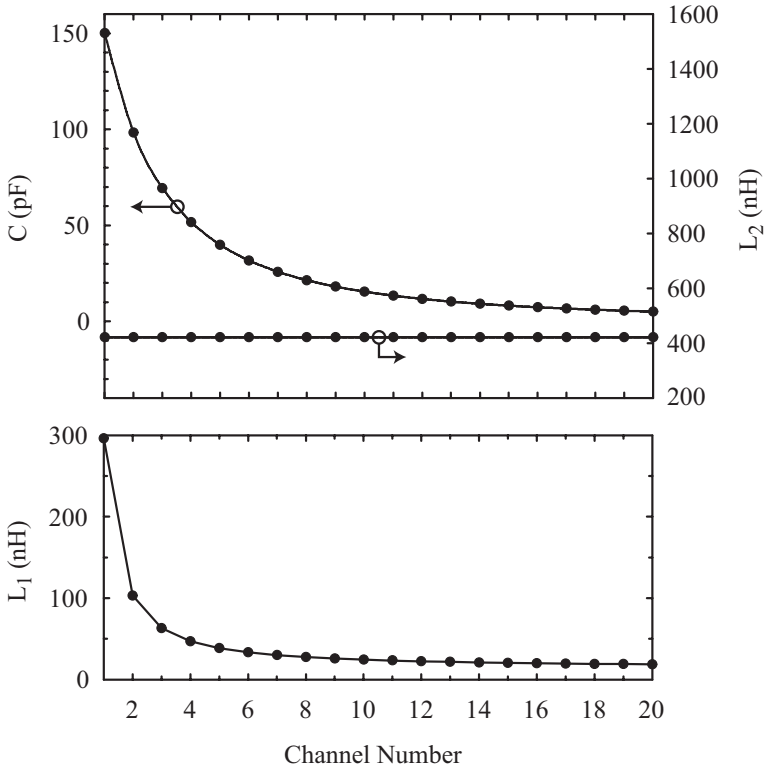

Figure 3.10: Component values for L_1, L_2, and C for the 20–90 MHz constant absolute bandwidth channelizer.

3.2.4 Measurements

The channelizer is tuned by adjusting the trimmer capacitors on individual channel resonators until nulls in the measured S_{11} match the simulated response (Fig. 3.11) assuring the correct resonator center frequencies. Measured and simulated S_{21} for each channel ($S_{(n+1)1}$ for $1 \leq n \leq 20$) are shown in Fig. 3.12 while a sample of three separate measured channel responses is shown in Fig. 3.13 showing good agreement with simulations. Measured insertion loss at the center of each channel ranges from 1.9 dB to 4.8 dB, with an average of 4.3 dB. The measured center frequencies

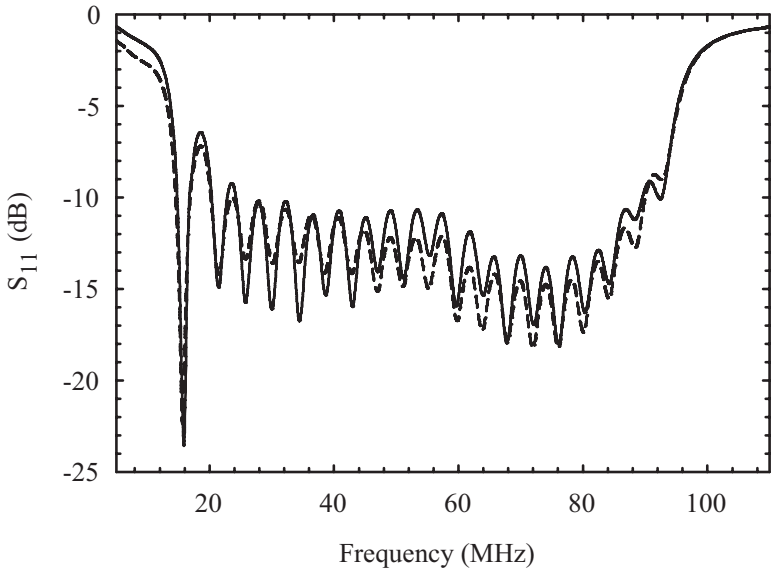

Figure 3.11: Measured (solid) and simulated (dashed) S_{11} of the 20-channel constant absolute bandwidth channelizer.

and channel responses again match simulation closely. As in the constant fractional bandwidth case, adjacent channel S_{21} responses cross at ~ 2 dB below each channel's center frequency (Table 3.3). Each channel's 2-dB crossover bandwidth is a nearly-constant 4 MHz, resulting in fractional bandwidths ranging from 26.0% (channel 1) to 4.3% (channel 20).

Table 3.3: Channelizer Center Frequencies (in MHz)

Ch	f_c	Ch	f_c	Ch	f_c	Ch	f_c
1	15.4	6	37.8	11	58.5	16	78.6
2	20.5	7	42.4	12	62.5	17	82.6
3	25.1	8	46.4	13	66.5	18	86.7
4	29.2	9	50.4	14	70.6	19	90.1
5	33.8	10	54.5	15	74.6	20	93.6

The power distribution at the center frequency of channel 10 (54.5 MHz) is shown in Table 3.4. The percent of the input power appearing at the individual outputs

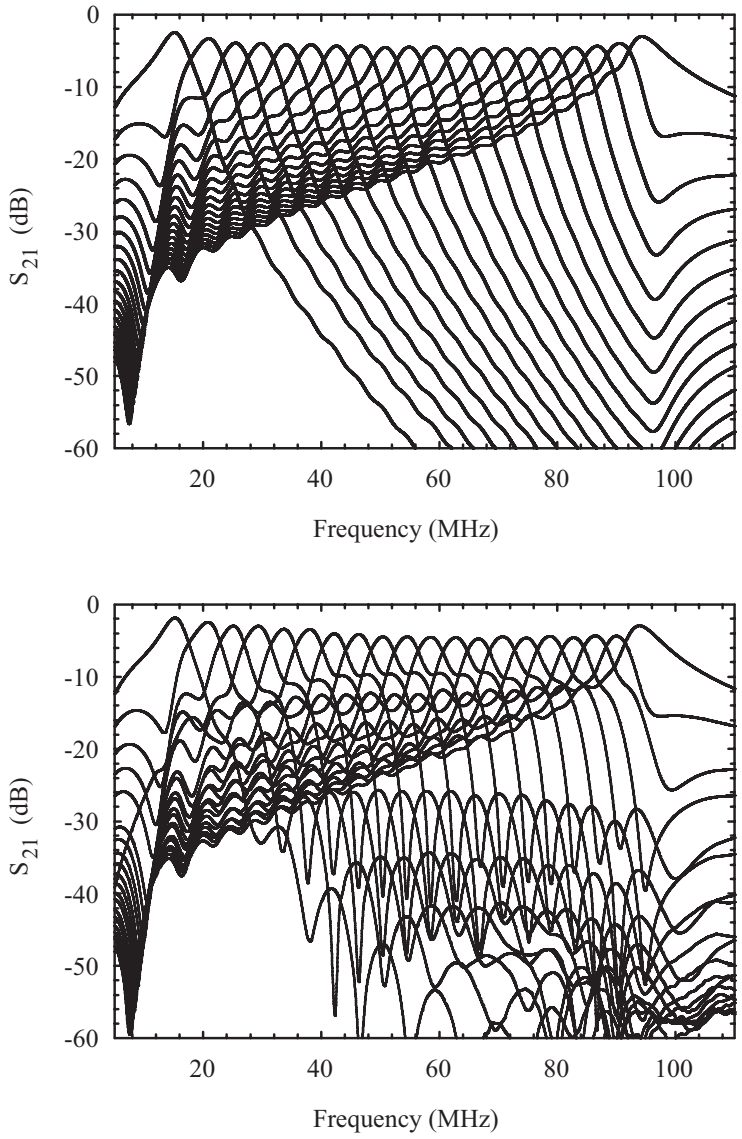

Figure 3.12: Simulated (top) and measured (bottom) S_{21} for each channel of the constant absolute bandwidth channelizing filter. The frequency scale is linear to show the constant absolute bandwidth response.

is calculated from each channel's measured $|S_{21}|^2$ and the reflected power at the channelizer input is given by $|S_{11}|^2$. At 54.5 MHz, 35.4% of the power arrives at the channel 10 output (-4.5 dB), 39.8% appears at all other channel outputs (Fig. 3.14), and 5.8% is reflected at the channelizer input. Summing the powers results in 81.0% of the input power. Thus, the filter dissipates 19.0% of the input power corresponding

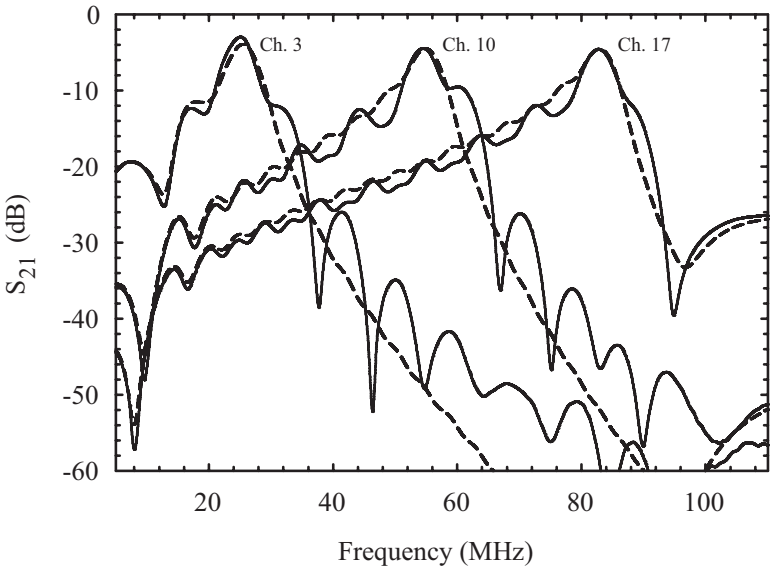

Figure 3.13: Measured (solid) and simulated (dashed) S_{21} of the constant absolute bandwidth channelizer for channels 3 (25.1 MHz), 10 (54.5 MHz), and 17 (82.6 MHz).

to an effective loss of 0.9 dB.

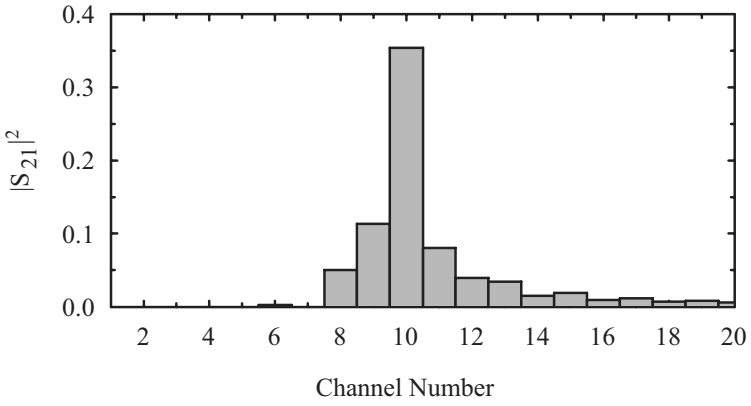

Figure 3.14: Measured power distribution at the center of channel 10 (54.5 MHz) among all 20 channels.

Table 3.4: Sample Channel Power Distribution for Channel 10

	Power (%)
Channel 10 Output	35.4 (−4.5 dB)
Sum of Channel 1–9, 11–20 Outputs	39.8
Reflected at Input	5.8
Sum of all Power Contributions	81.0
Power Dissipated	19.0

3.3 Channel Filter Properties

3.3.1 Channel Phase Response

From the results presented so far, we see that a channelizing filter based on cochlear modeling produces channels with near-uniform amplitude response; a characteristic $|S_{21}|$ scaled in frequency from one channel to the next. In addition, from data on biological cochlea measurements, we expect that the phase of S_{21} at each center frequency is nearly identical for all channels [55, 56]. This is shown in measured and simulated results for the RF channelizers (Fig. 3.15).

The uniformity among channel response in amplitude, phase, and phase constancy at the center frequency is determined by the number of sections physically preceding a particular channel. Typically a minimum of five sections are needed to set up the characteristic response. Since these initial sections are the higher frequency channels, the lower frequency sections of the channelizer have the most uniform response.

3.3.2 Transient Response

In many situations it is desirable to decompose a wideband input signal into narrower channels in real time. Transient simulations were done to demonstrate this channelizing filter's capability in such a system. These simulations were performed

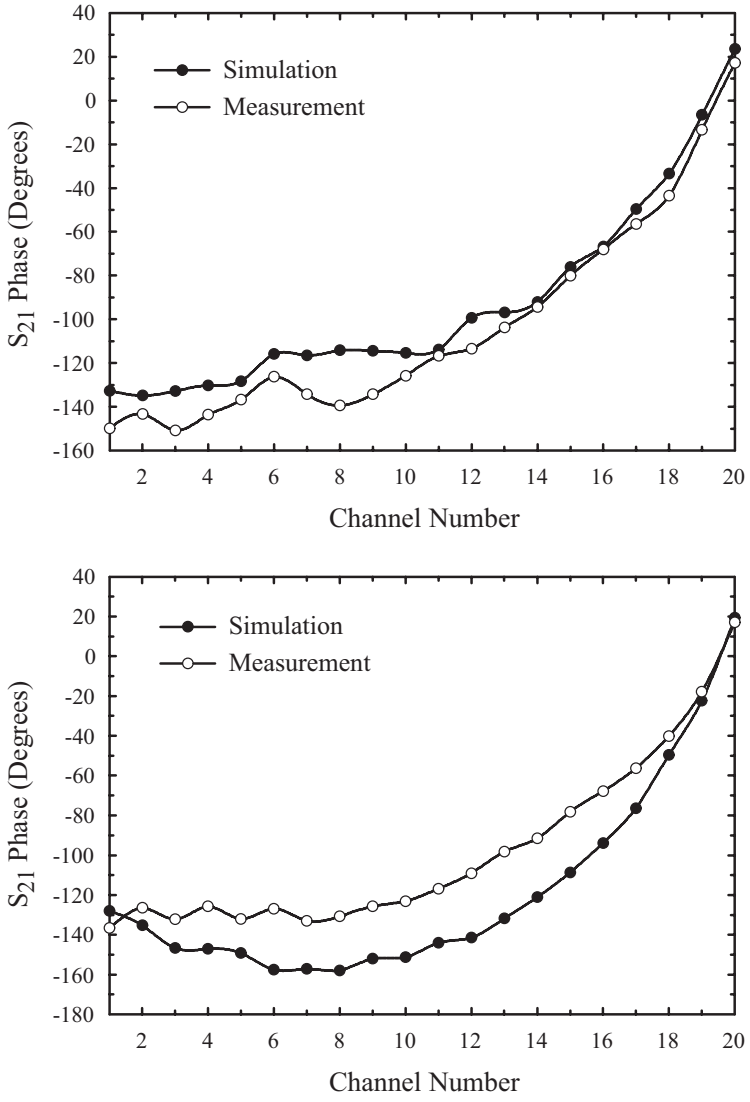

Figure 3.15: Measured and simulated phase of S_{21}, at each channel's center frequency, for the constant fractional bandwidth version (top) and the constant absolute bandwidth version (bottom). The data for each channel is taken at the center frequency of the particular channel.

using the constant absolute bandwidth channelizer. Finite Q, but otherwise ideal, lumped elements were used to reduce transient simulation complexity. Because the simulation did not include component or board parasitics, the channel responses were shifted slightly up in frequency compared with the previous S-parameter simulations.

A Gaussian monopulse filtered through a high-order maximally flat filter was

used to simulate a signal with a spectrum concentrated in the channelizer bandwidth (Fig. 3.16). A sample of the channel outputs is shown in Fig. 3.17. As expected,

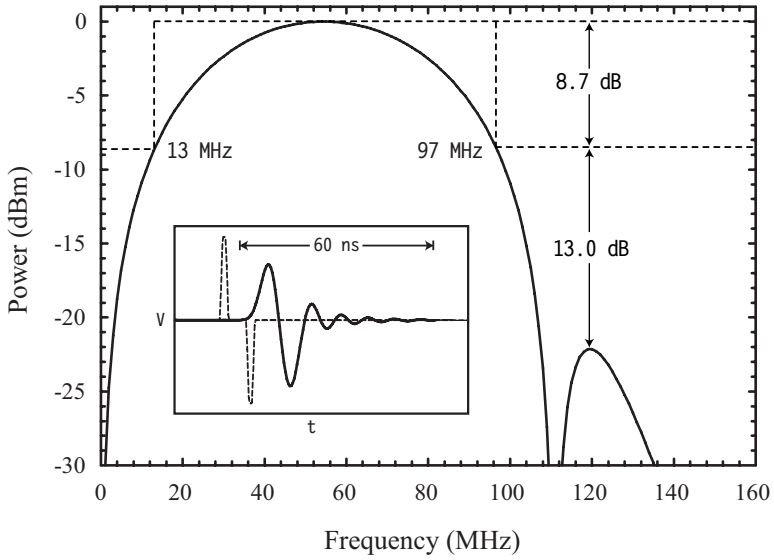

Figure 3.16: The simulated spectrum of the band-limited input signal used in the time-domain simulation (power adjusted to deliver 0 dBm at the band center). The inset shows the waveforms of pre-filter input monopulse (dashed) and the band-limited signal (solid) that is fed to the channelizer input.

each waveform is an exponentially decaying sinusoid of a frequency centered in the respective channel's passband. Thus, this type of channelizer can be used in a pulsed, wideband receiver where simultaneous reception is desired on every channel.

3.3.3 Radio System Applications

The cochlea has been the subject of intense modeling effort since the 1950s. Most of this research has focused on understanding mammalian cochlear dynamics. The work in this chapter has focused on adapting the cochlear structure to radio frequencies where we so often require channelization. To this end, the next obvious step is to increase the order of each channel's filter section to provide even more adjacent channel rejection.

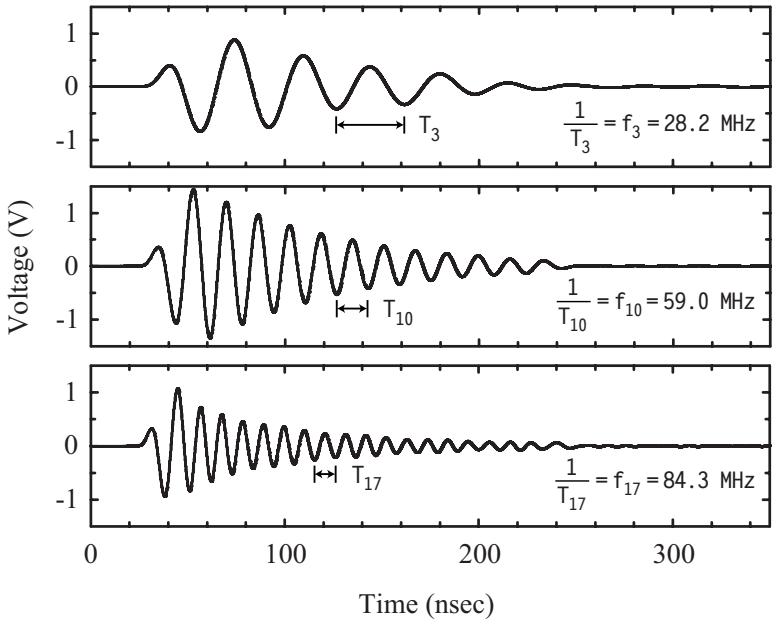

Figure 3.17: Three representative simulated waveforms that appear at channelizer output ports with the input signal shown in Fig. 3.16.

In theory, the cochlea-inspired channelizer topology can be applied to any frequency range. One obvious limitation is the effect of lumped component (especially inductor) self-resonances which produce undesirable responses within the total channelizer bandwidth. For channelizers covering many octaves, one must also mitigate the harmonic responses of distributed filter sections.

The cochlea-inspired channelizer circuit is a wide bandwidth contiguous channel multiplexer with a large number of channels. Conventional manifold type RF and microwave multiplexers using high-Q resonator technologies can achieve lower insertion loss and arbitrary pass-band responses, but with a limited number of channels (due to design complexity). Such high performance filters also come with a high cost and large size. In applications such as receiver front-end preselection and instantaneous spectrum monitoring, where lower stop-band rejection can be traded for a large number of channels, a cochlea-like channelizer fulfills the need with a straightforward design method.

Chapter 4

Microwave Planar Cochlear Channelizers

Channelization is also useful in higher frequency applications, such as ultra-wideband (UWB) systems. Often, only part of the spectrum is used at a time. In cases where strong adjacent channel interference exists, one can channelize the wideband input signal into narrow sub-bands which are then applied to active receiver stages (amplifiers, mixers, analog-to-digital converters). By virtue of its increased adjacent-channel rejection, such a preselection scheme increases receiver dynamic range and reduces intermodulation products. Alternatively, the same kind of preselector can be used to feed simple diode detectors resulting in a wideband instantaneous spectrum activity monitor (Fig. 4.1), which is important for UWB and/or cognitive radio systems.

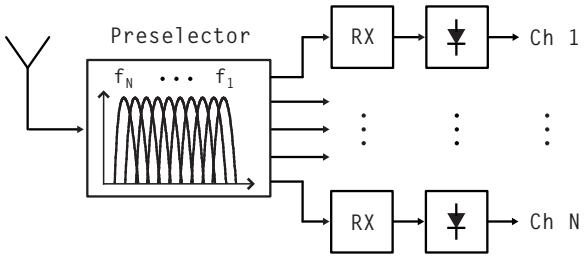

Figure 4.1: A spectrum activity monitoring receiver using a channelizing preselector filter.

In this chapter, a compact microwave channelizing preselector filter is presented covering 2–7 GHz in 15 channels suited for integration in UWB receiving systems. The filter is completely passive, and thus features high linearity and zero d-c power

consumption. In addition, an overview of component modeling used in the channelizer design is included.

4.1 Theory

The channelizer's structure is directly related to a 1-dimensional cochlear model whose lumped-element prototype schematic is shown in Fig. 4.2a [59]. Such a channel-

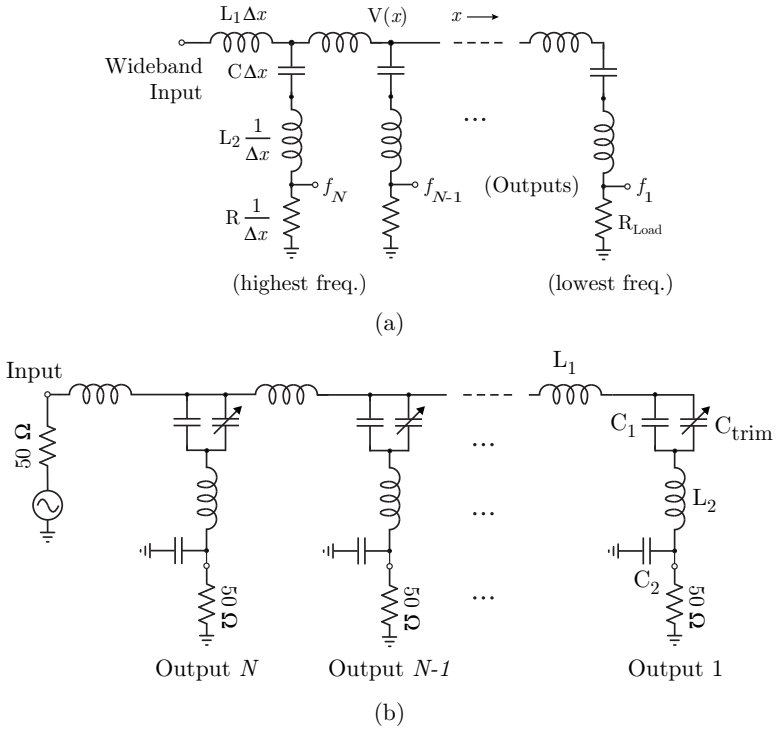

Figure 4.2: (a) Discretized, non-uniform transmission-line model of the basilar membrane (located within the cochlea). The channelizer is synthesized from this model. (b) Integrated channelizing filter schematic diagram. Trimmer capacitors are used to fine tune resonator center frequencies and an L-C matching network transforms the resonator output impedance to 50 Ω.

izer uses a cascade of shunt-connected series resonators coupled by series inductances. The series resonators form the individual channel filters whose upper stop-band response is enhanced by the presence of all higher frequency sections. The resulting

circuit offers a compact way of channelizing a wide bandwidth into many channels with a straightforward design method.

The silicon-based channelizer uses high-Q integrated lumped-element components to cover the 2–7 GHz band. The implemented circuit schematic is shown in Fig. 4.2b. The inclusion of an output L-C matching network at each resonator transforms the resonator's equivalent resistance at resonance ($R_{Load} = 6.25\ \Omega$ in this design) to a 50 Ω output port. The L-C network works well in each resonator's passband and offers additional stop-band rejection for out-of-band signals. In the actual layout, the matching network's inductor is absorbed within L_2, and the shunt capacitor C_2 is placed at each resonator's output terminal.

4.2 Circuit Design

The lumped element values, L_1, L_2, C, and R, for the channelizer circuit (Fig. 4.2a) are found from the functional dependence described in [59]. In this model four constants, α, A_1, A_2, and A_3 determine the LCR components of the channelizer by:

$$L_2(x)C(x) = A_1 e^{\alpha x} \tag{4.1}$$

$$R(x)C(x) = A_2 e^{0.5\alpha x} \tag{4.2}$$

$$L_1(x)C(x) = A_3 e^{\alpha x} \tag{4.3}$$

where x is the normalized transmission line length with $x = 0$ corresponding to the channelizer input. These constants are found with the specification of four design choices: minimum channel frequency f_1, maximum channel frequency f_N, number of channels N, and the transmission phase θ at each channel's center frequency (referred to the channelizer input). The parameter θ is assumed constant at the center of each channel based on measured acoustic cochlear data [55, 56], and primarily influences

the network's input impedance through the specification of the coupling inductances L_1.

The channelizer presented here is designed to cover 2 to 7 GHz in 15 channels (16% bandwidth) with an input impedance of 50 Ω. The required lumped-element values range from 2.10 nH to 7.60 nH for L_2, 220 fF to 1.25 pF for C_1, and 1.20 pF to 4.80 pF for C_2. In the prototype circuit covering several decades, L_1 increases exponentially with position along the channelizer. In designs covering less than two octaves, the variation is small enough that approximating L_1 with a single value works well. In this design, L_1 is a constant 0.7 nH inductor.

4.3 Layout and Fabrication

The lumped-element realization of this circuit is done using the M.I.T. Lincoln Laboratory Precision Multi-Chip Module (P-MCM) process. This technology offers high-Q suspended inductors and metal-insulator-metal (MIM) capacitors, along with three metal signal layers, a tantalum resistor layer, tungsten vias, and a 20 μm thick gold top metal layer (Fig. 4.3) [60].

The resonator inductors L_2 primarily determine the unloaded Q of the filter sections and thus the channel filter insertion loss. L_2 is implemented using suspended spiral inductors which have measured unloaded Qs of 35–45 from 2–7 GHz, for values of 2.10 nH to 7.60 nH, all using 20 μm wide lines and 20 μm spacing. The coupling inductors L_1 are standard spirals (not suspended), also use 20 μm width and spacing, and have Qs ranging from 25–30 from 2–7 GHz.

Two types of MIM capacitors are used. The resonator capacitors (C_1) are composed of signal 1 and signal 2 metal layers separated by 7.315 μm of SiO_2 (Fig. 4.3). This was chosen to result in reasonable dimensions for C_1 (0.22 pF to 1.25 pF). To facilitate post-fabrication resonator fine tuning, the top plates incorporate adjacent

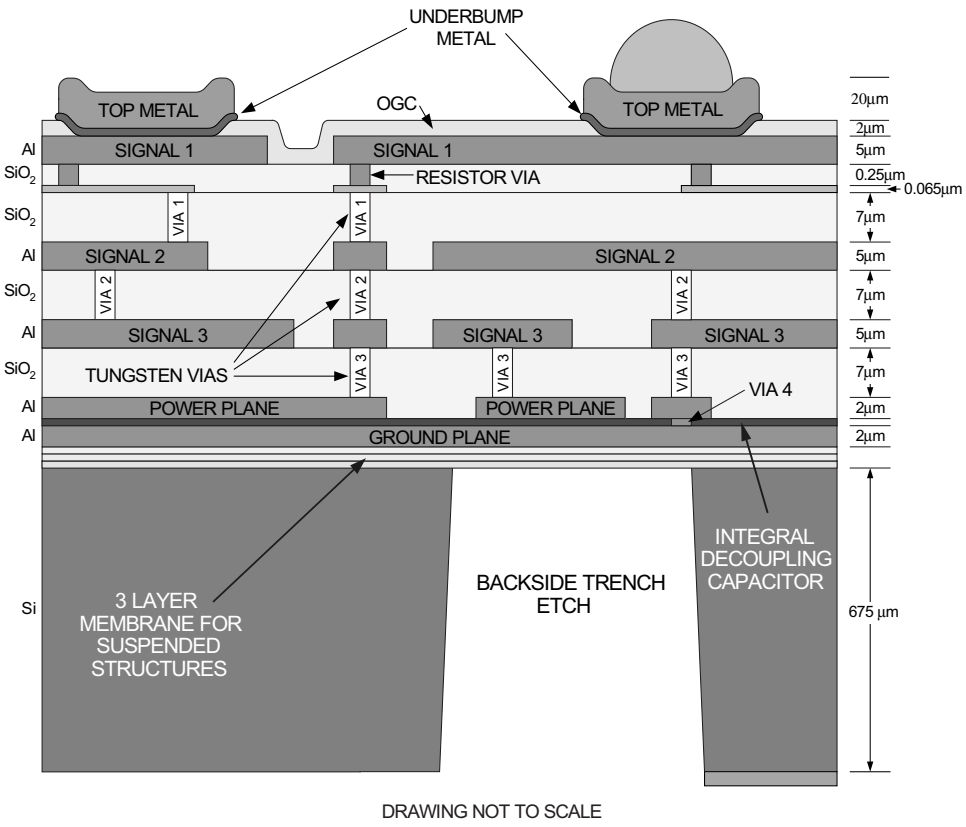

Figure 4.3: The Precision Multi-Chip Module (P-MCM) process developed by M.I.T. Lincoln Laboratory.

smaller plates that can be wire-bonded to increase the total resonator capacitance by up to 20% (Fig. 4.4). The shunt L-C matching network capacitors C_2 (1.2 pF to

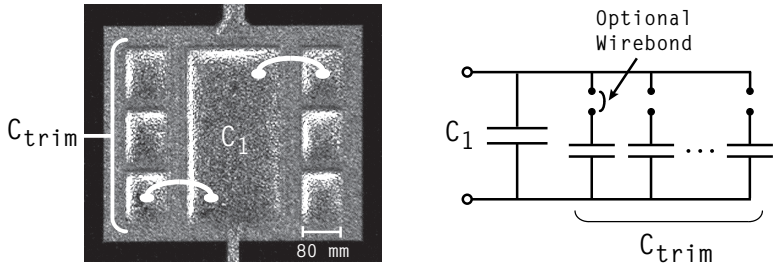

Figure 4.4: A close-up view of the resonator capacitor. The main top plate can be wire bonded to smaller auxiliary plates to increase capacitance and retune the resonator's center frequency.

4.8 pF) use the power and ground plane metal layers separated by 150 nm of Al_2O_3,

and both types of capacitors have a measured Q greater than 60 at their respective resonator's center frequencies.

On-chip resistors are used to terminate channels 1 and 15. This was done to allow testing of channels 2 through 14 with a 14-port wafer probe; as is well known, each channel must be terminated in 50 Ω for S-parameter measurements.

Each inductor, capacitor, and interconnect line is modeled with Sonnet software [58] and the results exported as S-parameters for analysis in Agilent ADS [57]. The entire circuit is then modeled in ADS.

4.4 Results

A microphotograph of the fabricated channelizer chip is shown in Fig. B.3. The channelizer input is on the left and the channel resonators extend rightward with decreasing center frequency. Wire bonds connecting opposite edges of the top-metal pattern mitigate in-band ground loop resonances. Ground-signal-ground (GSG) probe pads occupy the die perimeter (not shown) and connect to microstrip lines for the input and channel output ports.

A set of test structures including individual channel resonator sections is included on each sample wafer. The transmission response (S_{21}) of each resonator is measured and compared to simulation. In cases where the measured resonant frequency is higher than expected, additional top plate area is bonded to the respective resonator capacitor C_1 (Fig. 4.4).

The filter's S-parameters are measured using an on-wafer probing set-up. A 2-port short-open-load-thru (SOLT) calibration places the measurement reference planes at the GSG probe pads. A total of 14 GSG probes are available, allowing the simultaneous termination of 13 channel output ports (and one input port). The S-parameters of channels 2 through 14 are measured individually while all other channels are ter-

minated with 50 Ω loads through wafer probes. (Channels 1 and channel 15 are terminated with integrated resistors on the silicon wafer.)

The measured and simulated input reflection (S_{11}) for the complete channelizer is shown in Fig. 4.7 and the transmission response (S_{21}) for each channel is shown in Fig. 4.8 and Fig. 4.9.

Using the trimmer capacitor scheme, channels 2 through 14 are tuned to within -5.5% and $+2.2\%$ of their target center frequencies (most were within $\pm 2\%$). The S_{21} responses of each channel (Figs. 4.8 and 4.9) exhibit the cochlea-like response seen in previous RF channelizer designs [59] and biological cochlea data. The lower stop-band exhibits a 20 dB/decade second-order (single resonator) response while the upper stop-band rolls off at greater than 100 dB/decade. The enhanced response above the passband is due to additional poles created by higher frequency channels that appear before a particular channel resonator.

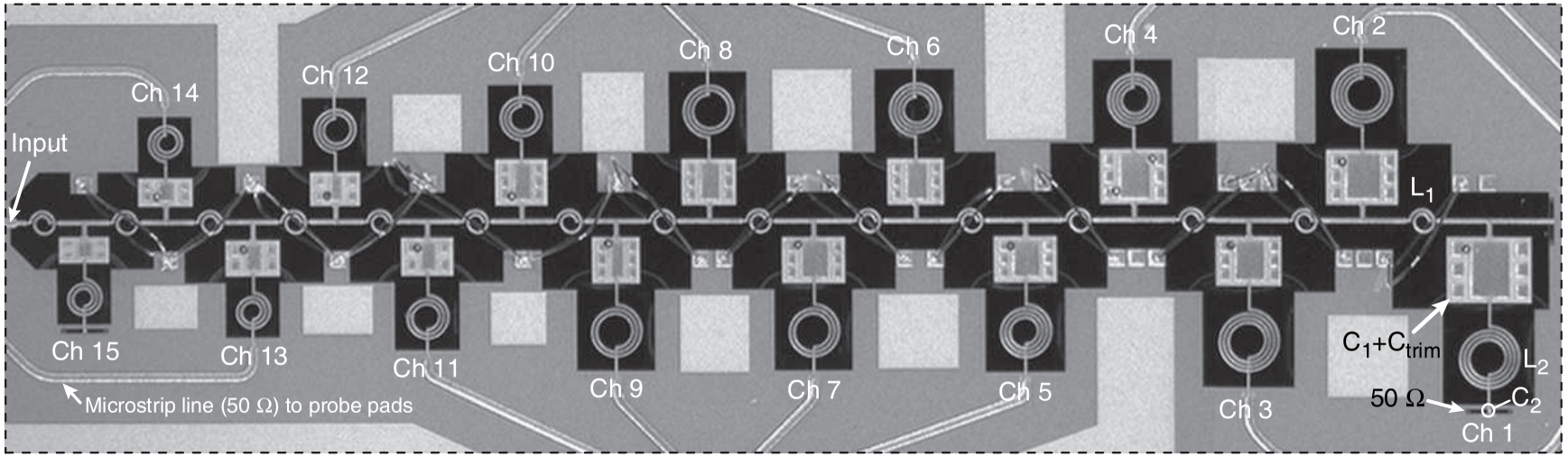

Figure 4.5: A microphotograph of the 15-channel channelizer. The chip measures 3.4 mm by 14.1 mm, not including the microstrip lines leading to probe pads (not shown). Channels 1 (furthest from input) and 15 (nearest to input) are internally terminated in 50 Ω. All other channels are probed using CPW probe pads (not shown). Diode detectors can be placed at each channel output for spectrum activity monitoring.

Figure 4.6: On-wafer S-parameter measurement set-up at M.I.T. Lincoln Laboratory. A channelizer under test is in the center of the wafer chuck. Four multi-port RF probes (total of 14 ports) allow a single two-port channel measurement while simultaneously terminated 13 other channels.

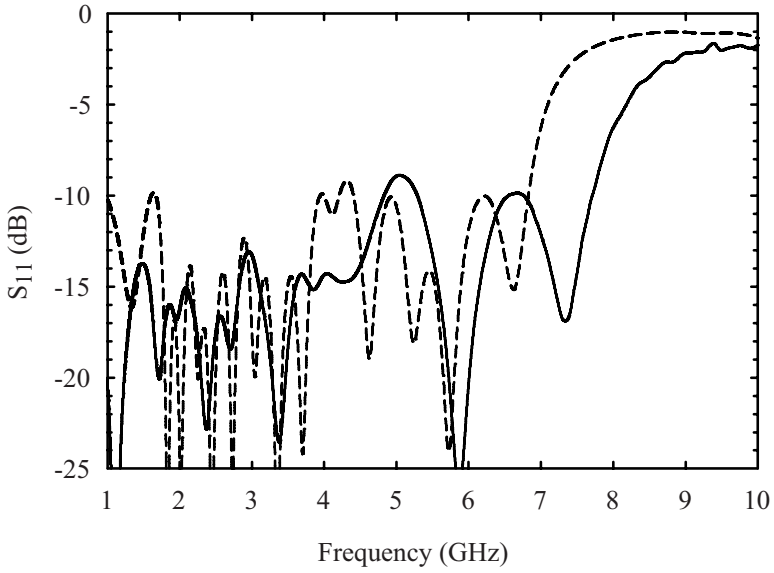

Figure 4.7: Reflection (S_{11}) response of the channelizer, for measured (solid) and simulated (dashed) results. All channels are terminated in 50 Ω.

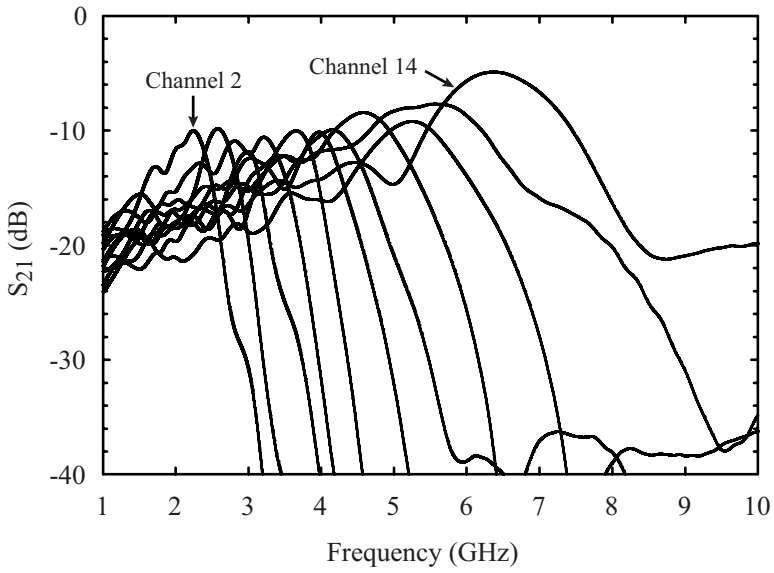

Figure 4.8: Measured transmission (S_{21}) response of channels 2 through 14.

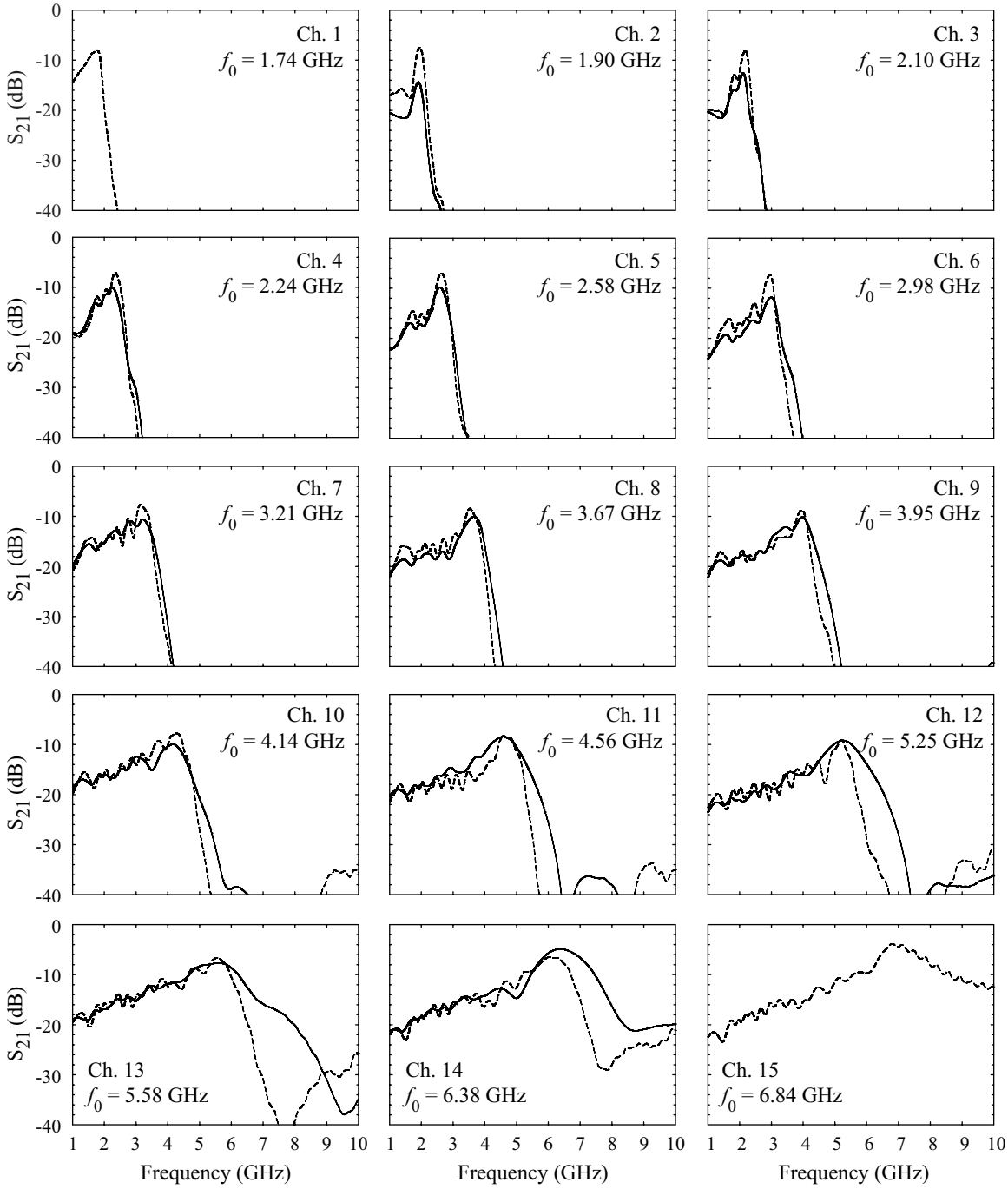

Figure 4.9: The transmission (S_{21}) response of the 15 channelizer channels, with measured (solid) and simulated (dashed) results. Channels 1 and 15 were not measured due to a limited number of available wafer probes (these channels are terminated on-chip).

The insertion loss of each channel ranges from 4.9 dB to 14.3 dB with most channels having an insertion loss of $\sim$ 9 dB, where 1 dB is due to the microstrip line length and coplanar waveguide (CPW) probe transition. The remaining loss is dominated by resonator inductor and capacitor conductor losses (the resonators have unloaded Qs of 25–30) and conductor and radiation loss of the high-impedance interconnect line which connects the channels. Modeling shows that the average insertion loss can be improved to 5 dB by modifying the interconnect line and shielding the circuit.

4.5 P-MCM Component Modeling

Success of the previously described channelizer depended on accurate modeling of the lumped-element components implemented in the P-MCM process. No scalable inductor, capacitor, or resistor models existed for this non-commercial process, though a good amount of measured data was available to compare with existing, general models and equations. The channelizer circuit was first designed with ideal components. The design process proceeded by using approximate formulas for lumped-elements [61] and then simulating each component in a moment-method simulator [58] using the technology stack-up shown in Fig. 4.3. Test structures, breaking out the each inductor and capacitor value used, were also fabricated in order to validate the modeling work. The full-wave models were simplified in some cases to lessen computer memory requirements. In particular, the suspended inductors were simulated with an air layer below the inductor, instead of a circular air cavity surrounded by silicon (Fig. 4.10). The simulation reference planes were placed immediately after the probe pad layout. The pads were de-embedded from the measured data by introducing -27 pF capacitors at each port.

A comparison of measured and simulated inductance values for all inductors is

shown in Fig. 4.11 (wideband) and Fig. 4.12 (narrow-band), while Fig. 4.13 compares the measured and simulated Q of the resonator inductors. Simulated inductance

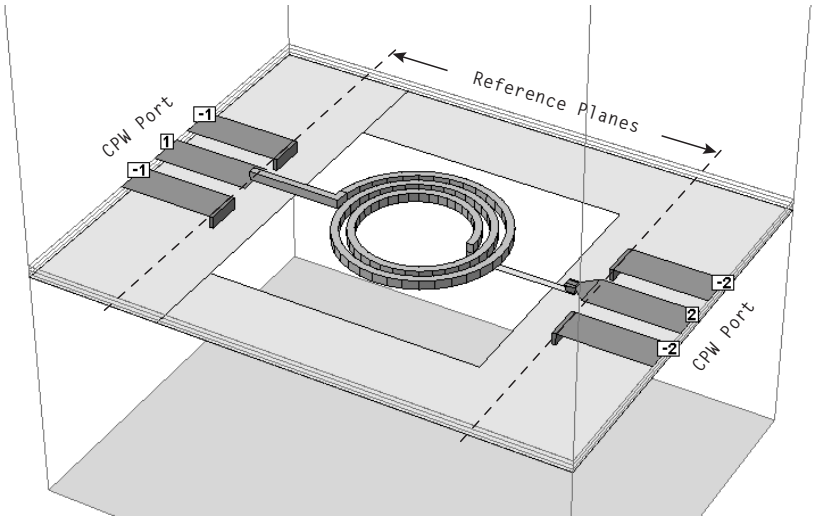

Figure 4.10: Suspended P-MCM inductor layout used in Sonnet full-wave simulation. Simulation data is de-embedded to the reference planes shown and compared to measured S-parameters.

values matched measurements within 2–4% while Q and self-resonant frequency (SRF) were also well predicted. Resonator capacitors were also modeled using a full-wave simulator (Fig. 4.14). The component value uncertainty was expected to be higher for the capacitors since the capacitance is proportional to $1/d$ (where d is the dielectric thickness) and the d process variation was specified as $\pm 10\%$. Still, simulated and measured capacitance matched within expectation (10–20%). Example capacitance data is shown in Fig. 4.15, along with a comparison of simulated and measured capacitor Q and SRF. Modeled Q is significantly higher than measurement as is due to underestimated conductor and dielectric losses in simulation and the inherent error in calculating large ($\gg 50\,\Omega$) and small ($\ll 50\,\Omega$) impedances with $50\,\Omega$ S-parameters.

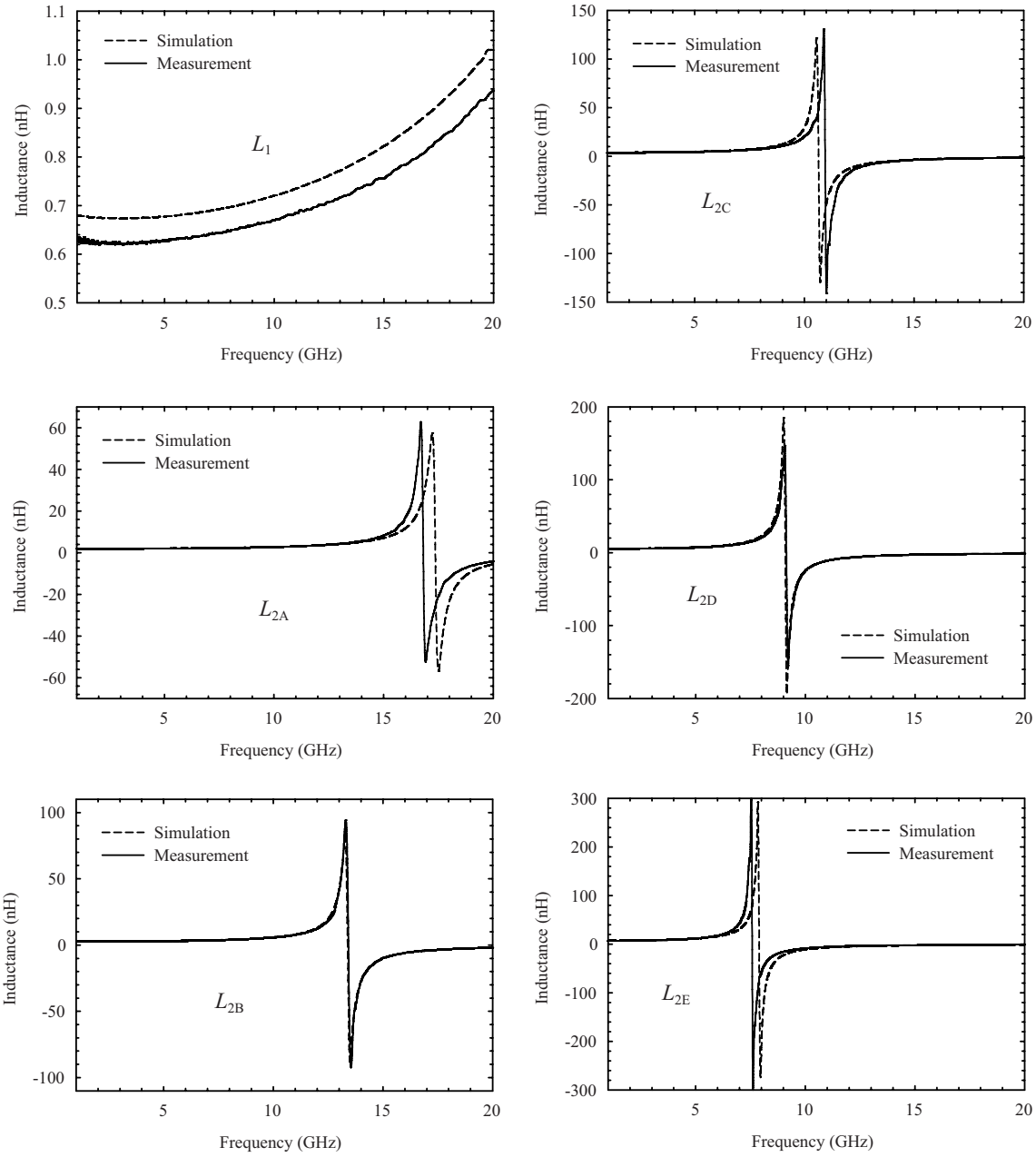

Figure 4.11: Simulated (dashed) and measured (solid) inductance of planar spiral inductors in the MIT-LL P-MCM process. L_1 is the standard inductor used in the channelizer manifold while L_{2x} are suspended inductors used in the resonator sections.

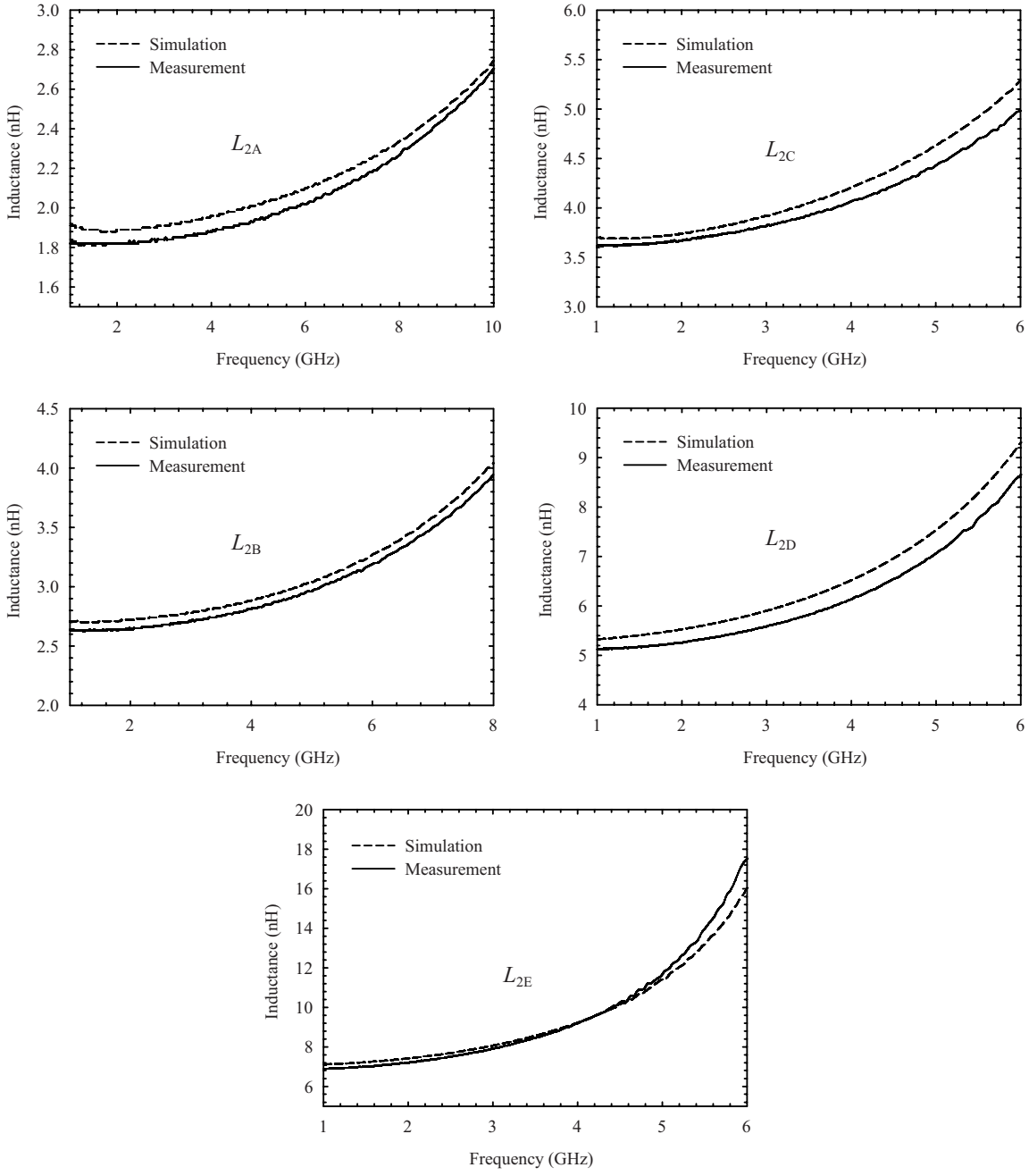

Figure 4.12: Simulated (dashed) and measured (solid) inductance of the suspended resonator inductors over their bands of use.

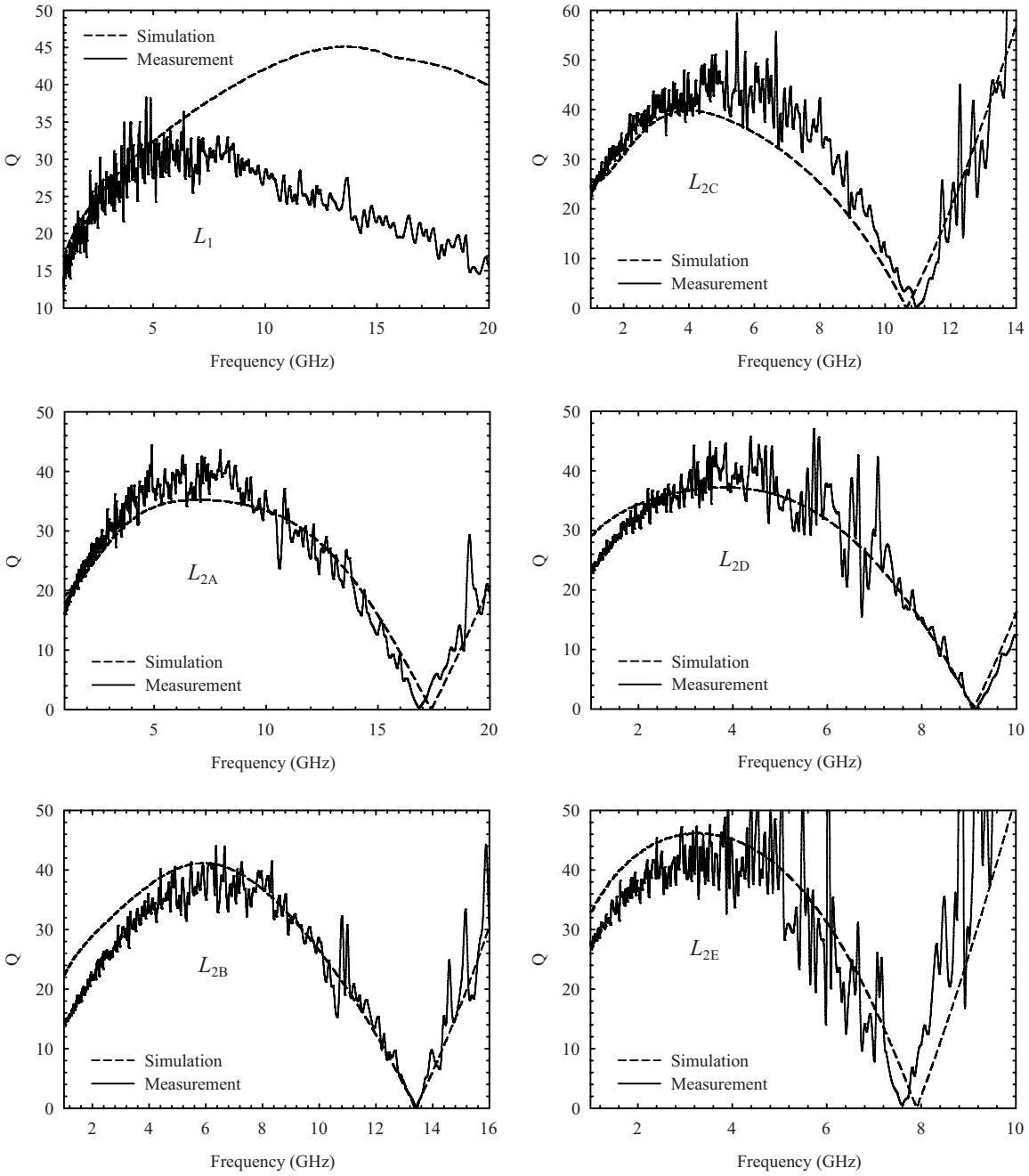

Figure 4.13: Simulated (dashed) and measured (solid) inductor Q of planar spiral inductors in the MIT-LL P-MCM process. L_1 is the standard inductor used in the channelizer manifold while L_{2x} are suspended inductors used in the resonator sections.

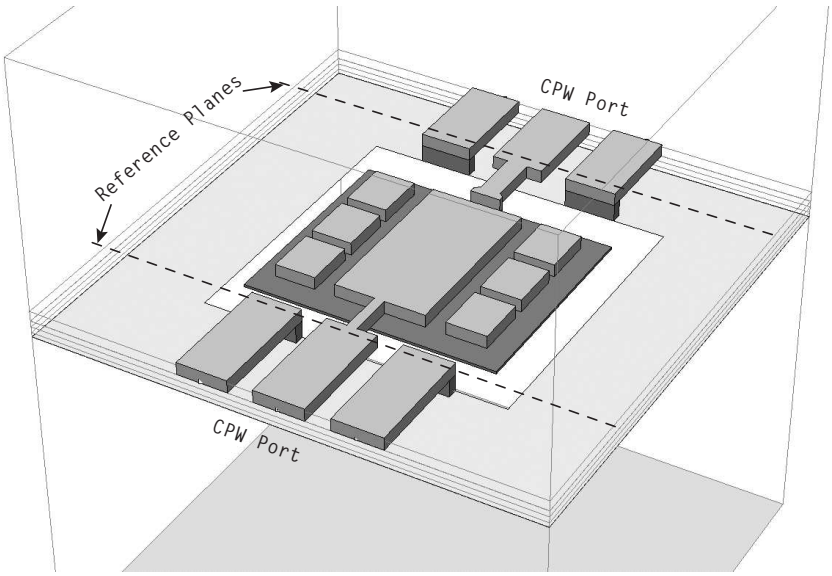

Figure 4.14: P-MCM trim-able resonator capacitor layout used in Sonnet full-wave simulation. Simulation data is de-embedded to the reference planes shown and compared to measured S-parameters.

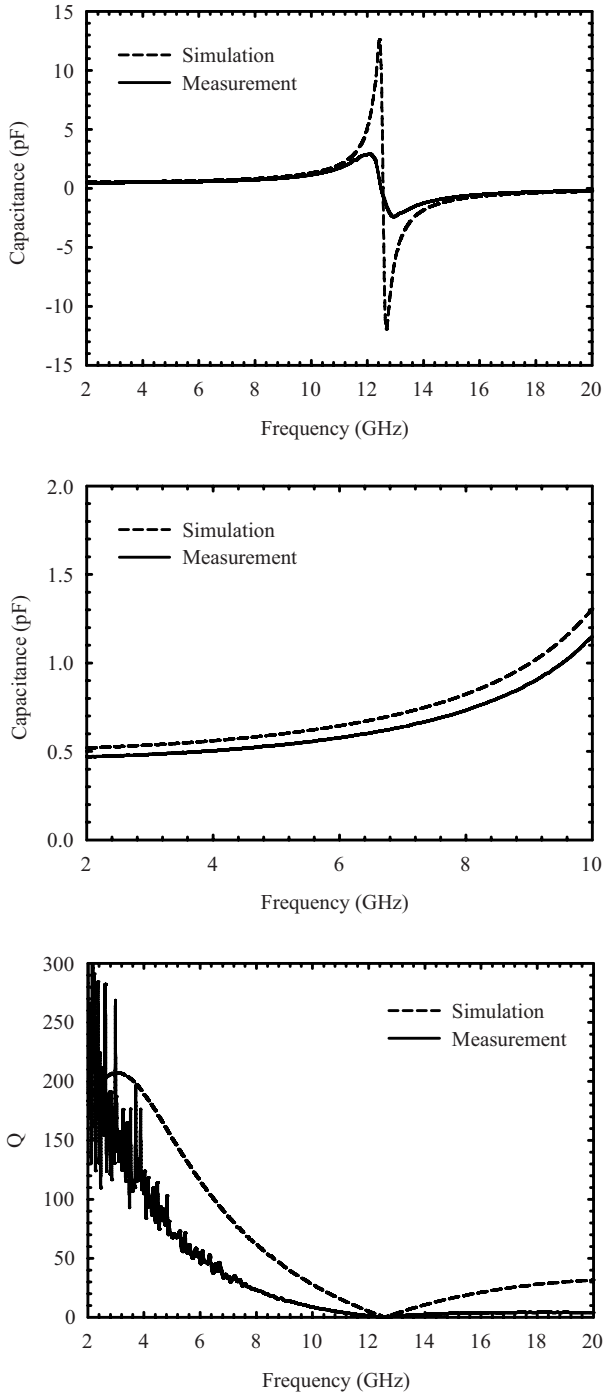

Figure 4.15: Simulated (dashed) and measured (solid) capacitance (wide-band, top and narrow-band, middle) and Q (bottom) of a resonator capacitor test structure (Fig. 4.14).

Chapter 5

Higher-Order Cochlear Channelizers

In this chapter, a design method is presented for contiguous-channel multiplexing filters with many channels covering a wide bandwidth. The circuit topology extends previous work on cochlea-like channelizers by introducing multiple resonator-channel filter sections. The new design provides increased stopband rejection, lower insertion loss, and improved passband shape compared with the earlier version while retaining a simple design method and a compact layout, and requires no post-fabrication tuning. Results of a 3-pole, 10-channel channelizer covering 182 MHz to 1.13 GHz with 17.5% bandwidth channels and 1.1 dB insertion loss are presented, and agree well with theory. A discussion of the power handling of planar channelizers is also presented.

5.1 Introduction

In single-order channelizers presented in Chapters 3 and 4, the channel filters used only series resonator sections (analogous to biological cochleas) and, as a consequence, lacked lower stopband rejection and had non-flat passband shapes. In this chapter, we present an improved cochlear channelizer that implements higher-order filters in each channel. This version retains the simple inductive manifold of the single-order cochlea channelizer but offers improved stopband rejection, passband shape, and reduced insertion loss. A design procedure is given for a 3rd-order cochlear channelizer that is well suited for microstrip implementation and a 10-channel design covering a 6:1

frequency range from 182 MHz to 1.13 GHz is presented. Such a channelizer finds use as a pre-selector filter in wideband receivers and instantaneous spectrum activity monitors as well as a multiplexer in wideband transmit applications.

5.2 Cochlear Channelizers Overview

5.2.1 Single-order channelizers

The first attempts to create cochlea-like RF channelizing filters were based on a circuit topology derived from an electrical-mechanical analogy of the basilar membrane. The result is a discretized, non-uniform transmission line arranged with the highest frequency (f_N) channel near the input and the lowest frequency (f_1) channel at the end of the channelizer manifold (Fig. 5.1a). The channels are coupled using

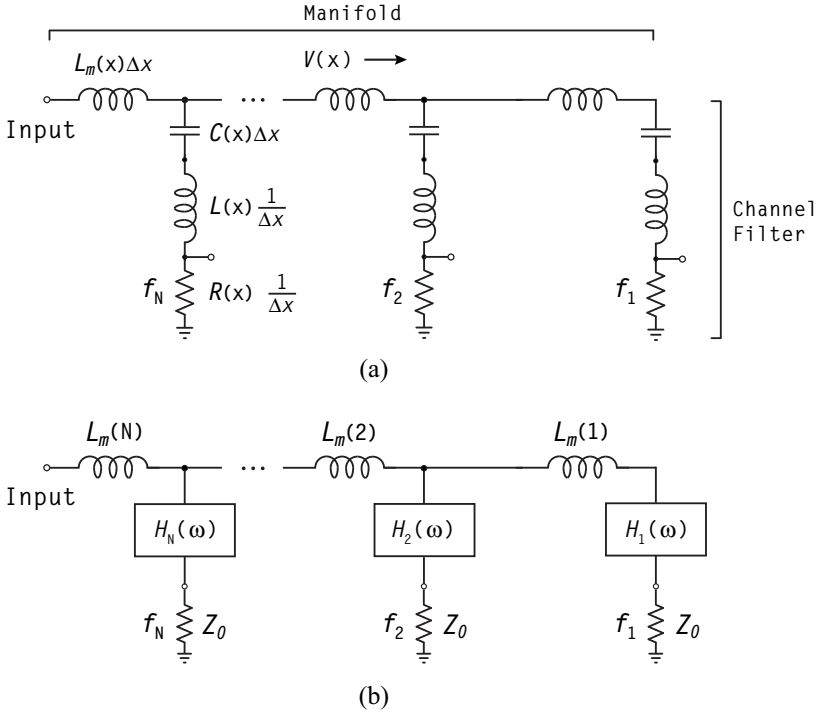

Figure 5.1: (a) Single-order cochlear channelizer discretized non-uniform transmission line model. (b) Higher-order channelizer circuit model.

a manifold composed of small-value inductors. The electrical component values for a single-order (single resonator) cochlear channelizer with constant fractional bandwidth channels are described by

$$L(x)C(x) = A_1 e^{\alpha x} \tag{5.1}$$

$$R(x)C(x) = A_2 e^{0.5\alpha x} \tag{5.2}$$

$$L_m(x)C(x) = A_3 e^{\alpha x} \tag{5.3}$$

where the four constants α, A_1, A_2, and A_3, are determined by the channelizer's minimum and maximum channel center frequencies, channel fractional bandwidth, and the phase at the center of each channel. Such a channelizer results in a compact and simple to design network with good upper stopband rejection for each channel. However, the single resonator channel filters have a lower stopband rejection of roughly 20 dB/decade and do not provide a tailored passband shape. The theory and design procedure for these filters is given in [62] and results of several versions are presented in [59] and [63].

5.2.2 Higher-Order Channelizers

Higher-order cochlear channelizers use multiple resonator filters for each channel filter while retaining the simple inductive manifold of the single-order model (Fig. 5.1b). The higher-order channel filters provide excellent upper and lower stopband rejection and a flat passband shape. Because of the increased selectivity, adjacent channel responses overlap much less, minimizing the power sharing between channels and thus decreasing the insertion loss of each channel as compared with single-order versions. For comparison, example channel responses for 3rd-order and single-order channelizers are shown in (Fig. 5.2).

The main problem in moving from single-order to higher-order cochlear channel-

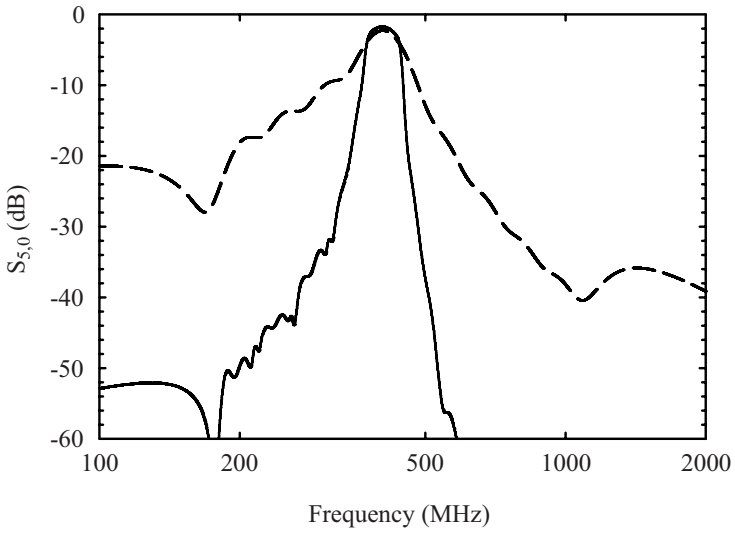

Figure 5.2: Single channel responses of two channelizers, 3rd-order (solid line) and single-order (dashed line), covering the same bandwidth (200–1000 MHz) with 10, 18% channels.

izers lies in producing a channel filter whose input impedance behaves as a series resonator (Z_{ch} in Fig. 5.3). At the connection node to the inductive manifold, each channel filter should appear capacitive at frequencies below its passband and inductive above its passband (Fig. 5.3). In this way, the circuit from the input port to any

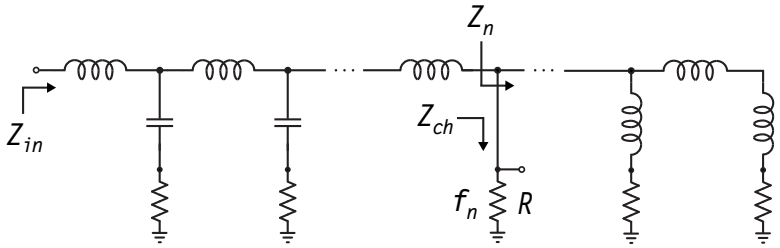

Figure 5.3: Simplified cochlear channelizer schematic at the resonant frequency of channel n.

particular channel node acts as a low-pass step-up matching network which transforms the driving point impedance at the resonating channel filter node (Z_n) to the channelizer input impedance (Z_{in} typically 50 Ω). The required channel filter input impedance (Z_{ch}) properties are discussed in the following section.

5.3 Circuit Design

The channelizer design procedure includes determining the number and bandwidth of each channel, synthesis of each channel filter, and designing the manifold.

5.3.1 Design Parameters

The design process starts with choosing the desired frequency range, channel fractional bandwidth, and crossover point for adjacent channels. The crossover point is chosen as 2 to 3 dB below each channel's maximum response. This creates the required amount of inter-channel coupling for the cochlea-like response and achieves a wideband input match by absorbing nearly all of the power in the total channelizer bandwidth. The number of channels N needed to cover the required bandwidth is given by

$$N \simeq 1 + \frac{\ln\left(\frac{f_N}{f_1}\right)}{\ln\left(\frac{1+\Delta/2}{1-\Delta/2}\right)} \tag{5.4}$$

where f_1 and f_N are the minimum and maximum channel center frequencies, respectively, and Δ is the fractional bandwidth of each channel defined from the crossover points of adjacent channels. The channel center frequencies are then chosen to cover the desired frequency range, starting with the lowest channel center frequency f_1 and continuing to the highest channel center frequency f_N, as

$$f_{n+1} = f_n \left(\frac{1+\Delta/2}{1-\Delta/2}\right), \qquad 1 \leq n \leq N-1. \tag{5.5}$$

5.3.2 Channel Filter Synthesis

The most important feature of each channel filter is its input impedance behavior over the *entire* channelizer bandwidth. In particular, each filter must present a near-

open circuit at its input port (Z_{ch}) for frequencies far above and below its center frequency (Fig. 5.4), appearing capacitive below its passband ($Z_{in} \rightarrow -j\infty\ \Omega$) and inductive above its passband ($Z_{in} \rightarrow +j\infty\ \Omega$).

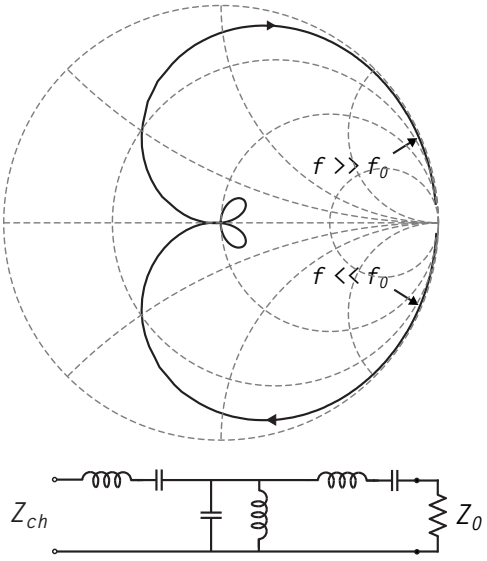

Figure 5.4: Required channel filter input impedance characteristic (Smith Chart) and the corresponding bandpass filter prototype for a cochlear channelizer (response for 3rd-order shown).

To understand why, consider the single-order circuit (Fig. 5.1a) as a low-pass transmission line with shunt-connected series resonant circuits. An input signal with frequency f_2 enters the input and first encounters resonators tuned to higher frequencies. These branches appear capacitive and, with the inductive manifold, produce a low-pass ladder network of shunt capacitors and series inductors. The signal propagates on this lumped LC transmission line until it reaches a series resonator with resonant frequency f_2. At this frequency, the resonator appears as a pure resistance R and absorbs the f_2 signal power.

If the series resonators are replaced with parallel types, the signal f_2 first encounters a near-short circuit (small inductive reactance) and is mostly reflected toward the input (Fig. 5.5a). Also, nearly as destructive to the channelizer operation are

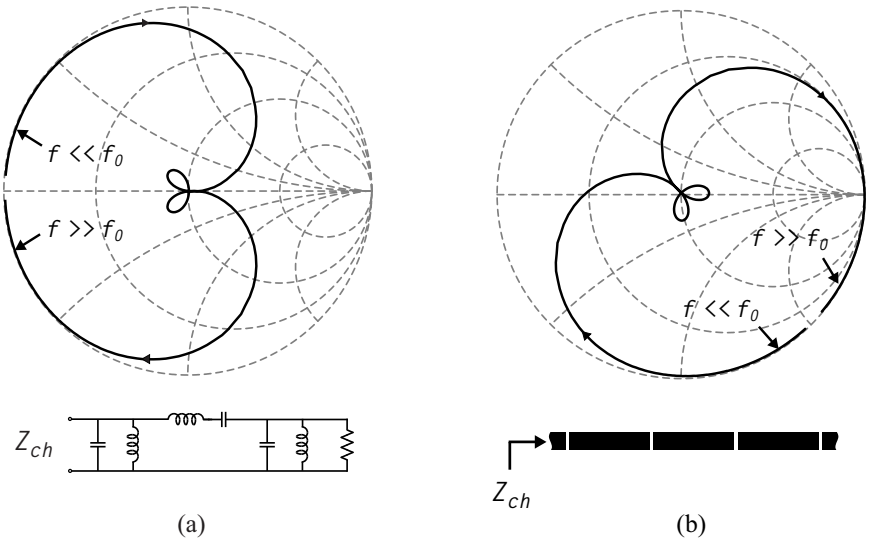

Figure 5.5: Examples of channel filter input impedance characteristics (Smith Charts) and their corresponding bandpass filter prototype (a) and distributed filter topology (b) which are unsatisfactory for a cochlear channelizer (see text).

filters which appear capacitive above their passband (Fig. 5.5b). In this case, the filter input impedance resonates with the inductive reactance looking into the manifold and produces a transmission zero within the channelizer bandwidth.

Unfortunately there are not many realizable RF and microwave filters that behave as near-ideal series resonant circuits at their input ports, over a wide bandwidth. One exception is the tubular topology shown in Fig. 5.6. When designed properly, an

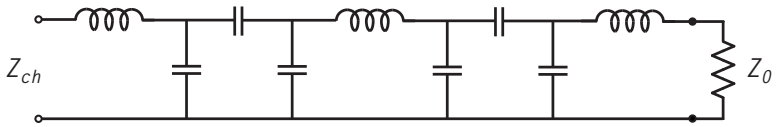

Figure 5.6: Tubular filter topology (3rd-order filter) with lumped-elements.

inductor is used at its input and this produces a series resonator-like response over a wide frequency range. Moreover, such a topology is well-suited for planar circuits using lumped elements [64]. In this case, series inductor parasitics to ground are

conveniently absorbed into the ends of the coupling capacitor pi-networks (Fig. 5.6).

To synthesize each channel filter one starts with the prototype bandpass filter (Fig. 5.7a), whose circuit elements are given by

$$L_k = \begin{cases} \dfrac{g_k R_1}{\Delta\,\omega_0} & k \text{ odd} \\ \dfrac{\Delta\, R_1}{g_k \omega_0} & k \text{ even} \end{cases} \tag{5.6}$$

and,

$$C_k = \begin{cases} \dfrac{\Delta}{g_k \omega_0 R_1} & k \text{ odd} \\ \dfrac{g_k}{\Delta\,\omega_0 R_1} & k \text{ even} \end{cases} \tag{5.7}$$

where Δ is the filter's fractional bandwidth,

$$\Delta = \frac{\omega_2 - \omega_1}{\omega_0},$$

and ω_0 is the filter passband center frequency, $\omega_0 = \sqrt{\omega_1 \omega_2}$, where ω_1 and ω_2 define the filter's passband limits [17]. For a channelizer input impedance (Z_{in}) of 50 Ω, channel filters with input impedance ($Z_{ch} = R_1$) from 5 to 20 Ω (all filters use the same R_1) result in reasonable component values and good input return loss over the channelizer bandwidth. To simplify the design process and accommodate an off-the-shelf inductor value L, one can use (5.6) with $L_1 = L$ to set the channel filter's input resistance (R_1) within a desired range (Fig. 5.7a). One can also slightly vary the lumped-element prototype parameters (g_k) (and thus the filter shape) to obtain a suitable inductance L for a needed channel filter R_1.

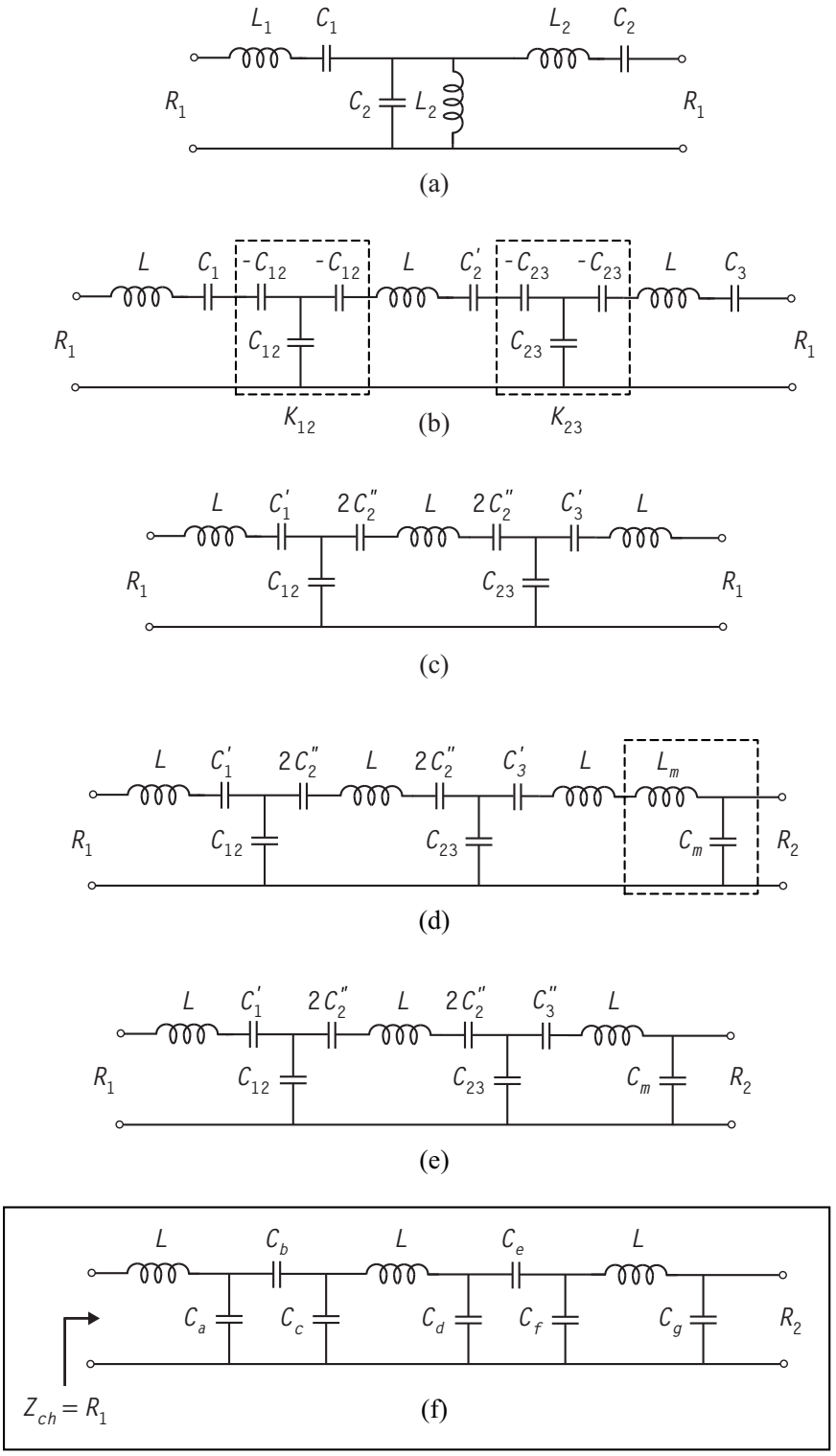

Figure 5.7: Channel filter schematics showing network transformations used to arrive at a channel filter with the desired input impedance characteristics.

For the odd-order filter with symmetric lumped-element prototype values,

$$K_{12} = K_{23} = \sqrt{\frac{L}{C_2}} \tag{5.8}$$

and the inverter capacitors are given by,

$$C_{12} = C_{23} = \frac{1}{\omega_0 K_{12}}. \tag{5.9}$$

The second resonator capacitor is chosen to provide the correct resonator impedance level while maintaining identical inductor values (Fig. 5.7b),

$$C_2' = \frac{L_2}{K_{12}^2}. \tag{5.10}$$

Next, the inverter capacitors are absorbed into the network (Fig. 5.7c),

$$C_1' = \left(\frac{1}{C_1} - \frac{1}{C_{12}}\right)^{-1} \tag{5.11}$$

$$C_3' = \left(\frac{1}{C_3} - \frac{1}{C_{23}}\right)^{-1} \tag{5.12}$$

$$C_2'' = \left(\frac{1}{C_2'} - \frac{1}{C_{12}} - \frac{1}{C_{23}}\right)^{-1}. \tag{5.13}$$

A matching section is then added to the output (Fig. 5.7d) to transform the output impedance to the desired channel output impedance R_2 (typically 50 Ω), using

$$C_m = \frac{\sqrt{R_2/R_1 - 1}}{\omega_0 R_2} \tag{5.14}$$

$$L_m = \frac{R_2^2 C_m}{1 + (\omega_0 R_2 C_m)^2} \tag{5.15}$$

and the third resonator capacitor is modified to maintain identical inductors in each resonator (Fig. 5.7e),

$$C_3'' = \frac{L}{L - L_m} C_3'. \tag{5.16}$$

A Tee (star) to Pi (delta) transformation is then performed on the sections coupling the second and third resonators, producing the desired tubular filter network, where (Fig. 5.7f)

$$C_a = \frac{C_1' C_{12}}{C_1' + 2C_2'' + C_{12}} \tag{5.17}$$

$$C_b = \frac{C_1' 2C_2''}{C_1' + 2C_2'' + C_{12}} \tag{5.18}$$

$$C_c = \frac{2C_2'' C_{12}}{C_1' + 2C_2'' + C_{12}} \tag{5.19}$$

$$C_d = \frac{2C_2'' C_{23}}{2C_2'' + C_3'' + C_{23}} \tag{5.20}$$

$$C_e = \frac{2C_2'' C_3''}{2C_2'' + C_3'' + C_{23}} \tag{5.21}$$

$$C_f = \frac{C_3'' C_{23}}{2C_2'' + C_3'' + C_{23}} \tag{5.22}$$

and finally (Fig. 5.7f),

$$C_g \equiv C_m \text{ (for nomenclature).} \tag{5.23}$$

Note that this synthesis relies on ideal inverter sections between the second and third resonators, and an ideal impedance matching section at the output port and is therefore approximate. For a channel filter fractional bandwidth above 10%, some adjustment is required to maintain the desired passband ripple and 3-dB points. In practice, one can use these synthesized circuit element values as a starting point in an implementation with real microstrip and lumped components, and tune the circuit using simulation tools to achieve the desired passband response. Synthesis of channel filters other than 3rd-order follows the same basic procedure.

5.3.3 Manifold Design

Higher-order channelizers use the same inductive manifold employed in single-order versions (Fig. 5.1a). In the higher-order case, the channel filters are designed for a termination on the manifold port with $R_1 = R$ (see Fig. 5.3) and $R_2 = 50\ \Omega$. For constant fractional bandwidth channels, the manifold inductors are exponentially scaled with distance (and thus frequency) along the channelizer, and using (5.2)–(5.3), are given by

$$L_m(x) = R\frac{A_3}{A_2}e^{\frac{1}{2}\alpha x} = L_0 e^{ax} \tag{5.24}$$

where $L_0 = R\frac{A_3}{A_2}$ and $a = \alpha/2$. In terms of (integer) channel number n, the coupling inductances are

$$L_m(n) = L_0 e^{a(1-n/N)}, \qquad 1 \le n \le N. \tag{5.25}$$

To design the manifold, one uses the same procedure described in [62] for a single-order channelizer using series resonators with input impedance R. The higher-order channel filter sections (with $R_1 = R$) are then coupled with the same manifold inductances. Alternatively, one can use a circuit simulator to find the coupling inductors, eliminating the need to program and iterate the numerical procedure in [62]. Once the channel filters are designed and connected by series inductances $L_m(n)$, one varies L_0 and a in simulation to achieve the best input return loss. As a starting point, $L_m(n)$ should be chosen to give a reactance ($X = 2\pi f L_m$) of 3–8 Ω at the lowest channel center frequency (f_1) and 10–20 Ω at the highest channel center frequency (f_N) with an exponential scale factor a of 0.3 to 1.0. These values are based on single-order designs and result in channelizers with Z_{in} centered near 50 Ω [62].

5.4 Experimental Results

5.4.1 Design, Layout, and Simulation

A 10-channel channelizer ($N = 10$) is designed to cover 200 MHz to 1 GHz (Fig. 5.8). A desired channel 3-dB fractional bandwidth of 18% in (5.4) indicates

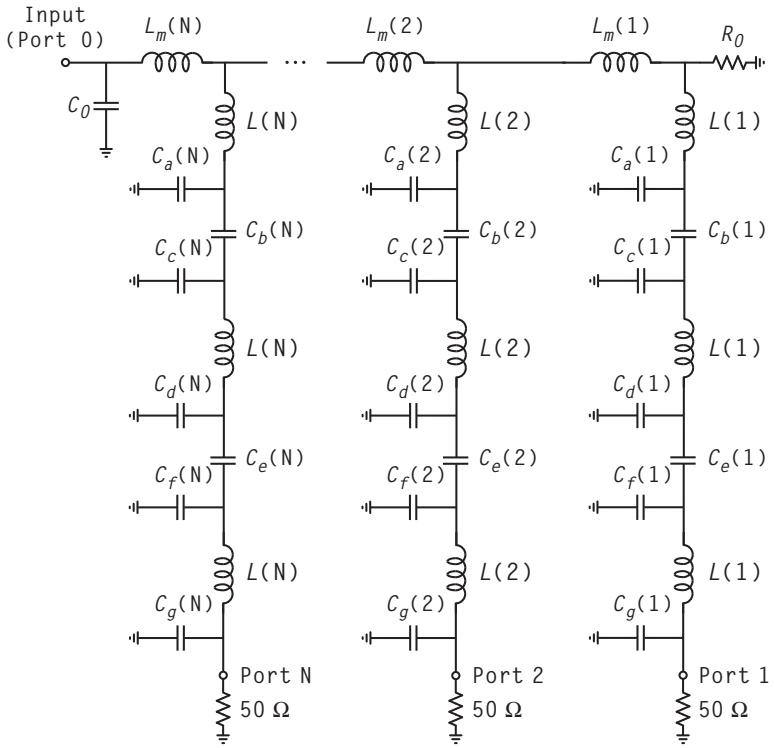

Figure 5.8: Circuit schematic diagram of a 3rd-order cochlear channelizer.

that 10 channels are required, and the channel filter center frequencies are calculated using (5.5). The inductors are chosen using (5.6) with the prototype (g_k) values for a 0.1-dB ripple Chebyshev passband for the channel filters (note that the $\Delta = 0.12$ specifies the ripple bandwidth). Commercially available inductor values ranging from 120 nH to 22 nH for 200–1000 MHz result in a filter (Z_{ch}) input resistance R_1 of $\simeq 17\ \Omega$. Each channel filter (Fig. 5.7f) is then synthesized using (5.6)–(5.23) with $R_1 = 17\ \Omega$ and $R_2 = 50\ \Omega$. With an $L_m(10) = 2.4$ nH (for channel 10) chosen to

give an $X \simeq 15\ \Omega$ at 1.02 GHz, a is varied in simulation, and $a = 0.8$ is found to give the best input return loss over the entire channelizer bandwidth. In this case, the resulting manifold inductors vary slowly from 2.4 nH ($L_m(10)$) to 4.9 nH ($L_m(1)$). To further improve the input match, a 2.75 pF capacitor is placed at the channelizer input (shunt to ground) to match the slightly inductive input impedance (Fig. 5.9). Also, a 1 kΩ resistor R_0 to ground is placed at the end of the manifold (Fig. B.3) to dampen any manifold resonances within the channelizer bandwidth. This value is chosen as a compromise between increased insertion loss ($R_0 < 500\ \Omega$) and very low damping ($R_0 > 2$ kΩ).

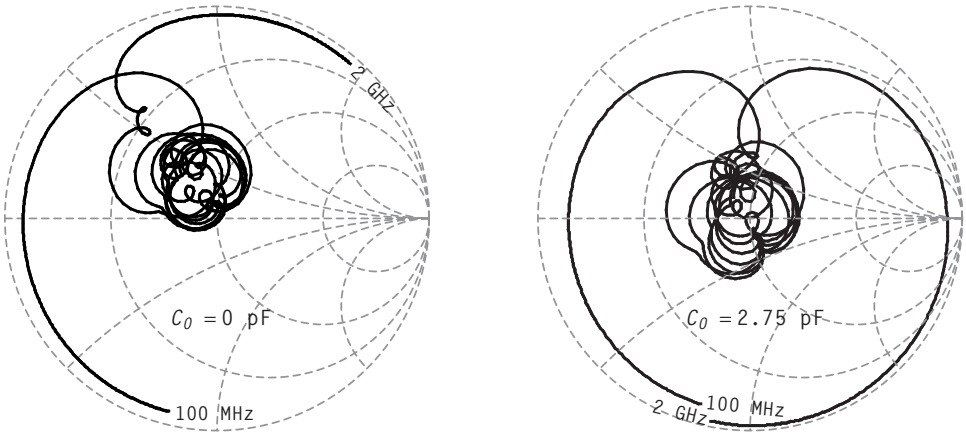

Figure 5.9: Simulated input impedance of the 10-channel 3rd-order channelizer without (a) and with (b) the input matching capacitor C_0, used to match the slightly inductive input impedance.

The circuit is implemented in a microstrip layout using 0.787 mm height PTFE/woven fiberglass ($\epsilon_r = 2.20$) laminate with two 53.3 μm thick copper layers and 0.51 mm diameter plated-through-hole vias. High-impedance (100 Ω) 0.635 mm width microstrip line lengths (ranging from 7.62 mm to 11.9 mm long) are used in lieu of lumped inductors (L_m) to create the manifold. The channel filters use surface mount

technology (SMT) devices, including Coilcraft Midi Spring[1] air coil inductors (L) and Dielectric Laboratories C06[2] multilayer capacitors (C_b, C_e, C_g), all with 2% or better tolerance. The remaining shunt capacitors (including C_0) are composed of the microstrip metal layer (top plates) and ground plane (bottom plates). The output of each channel filter (after C_g in Fig. 5.7f) is routed to an edge-launch SMA connector using 2.54 mm width 50 Ω microstrip lines with simulated losses of 0.56 dB/m at 1 GHz and 0.22 dB/m at 200 MHz. A close-up view of a single channel's layout

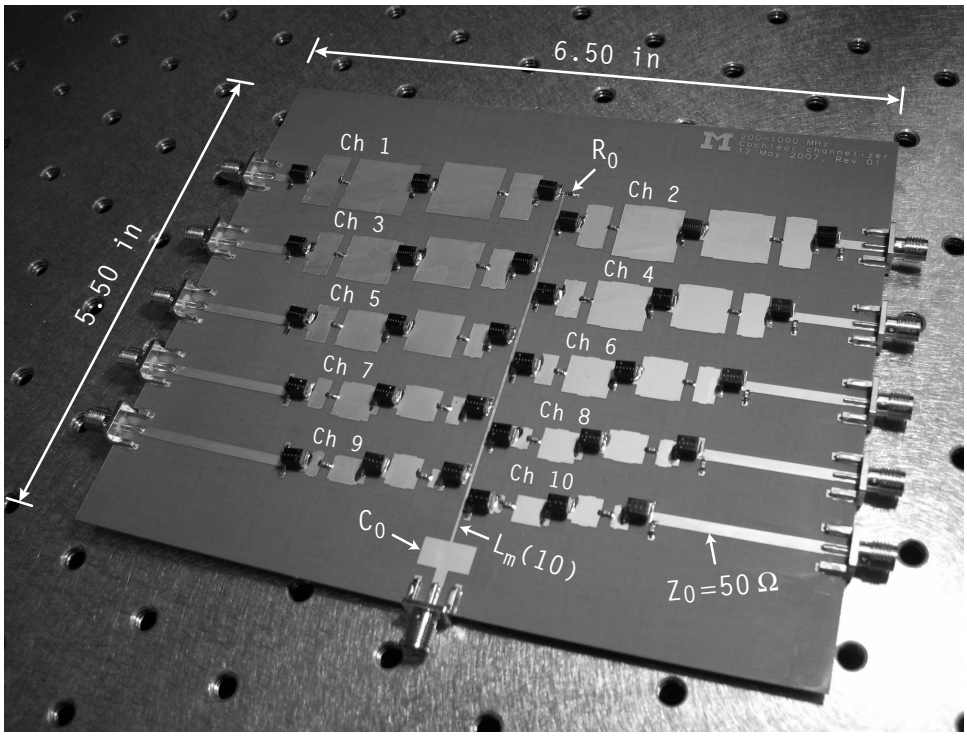

Figure 5.10: Photograph of a 10-channel 3rd-order cochlear channelizer with center frequencies ranging from 200 MHz to 1022 MHz. The channel filters are staggered on the sides of the inductive manifold. The input port is in the center of the lower substrate edge while the two sets of five output ports occupy the left and right board edges fed by microstrip lines from channel outputs.

(channel 5) is shown in Fig. 5.11. The channelizer manifold and filter lumped element

[1]Coilcraft Inc., Cary, IL USA
[2]Dielectric Laboratories, Inc., Cazenovia, NY USA

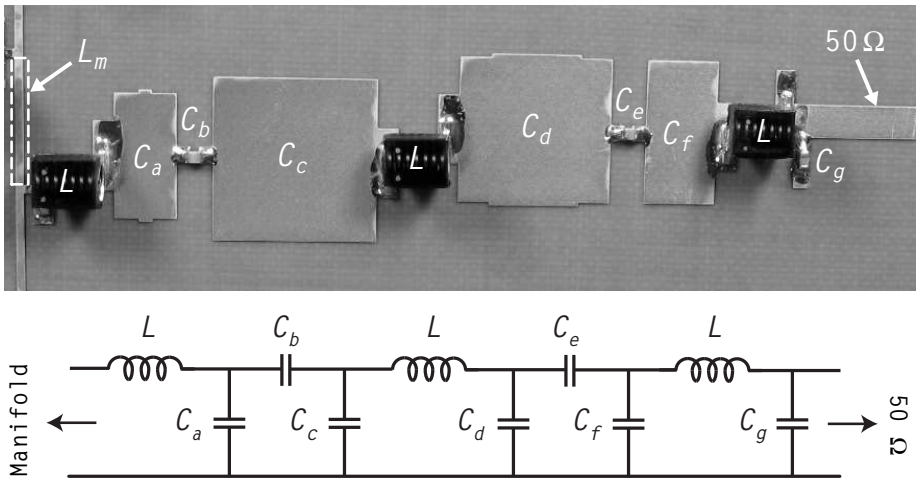

Figure 5.11: Close-up photograph (top) of single channel layout identifying a manifold inductor L_m (Fig. 5.8) and channel filter circuit components (bottom) for channel 5. C_a, C_c, C_d, and C_f are parallel plate capacitors patterned on the top metal layer, while C_b and C_e are multilayer SMT capacitors. The three resonator inductors L are air-wound coils while the manifold inductance L_m is a 0.635 mm width (100 Ω) microstrip line. A 2.54 mm wide 50 Ω microstrip line connects the filter output to an edge-launch SMA connector (not shown).

values are shown in Fig. 5.12, and these are used in circuit simulation to tune the microstrip layout.

First pass success in attaining good agreement between measurement and theory is attributed to a simulation method using very accurate models. Once the ideal filter elements are found (Figs. 5.8 and 5.12) each series inductor and capacitor is replaced with its SMT model from the Modelithics CLR Library [65] and simulated in ADS [57]. The SMT inductor models include the component pad and body parasitic capacitance to ground. These form a significant portion of the shunt capacitors C_a, C_c, C_d, and C_f and must be modeled to within ±1% to produce the expected filter responses. The parallel-plate shunt capacitors and transmission lines are simulated using Agilent ADS microstrip models and the capacitors are then fine-tuned using the Sonnet full-wave simulator software [58]. To minimize design time, each channel layout including component pads, shunt capacitors, and SMT ports, is simulated in Sonnet, and the

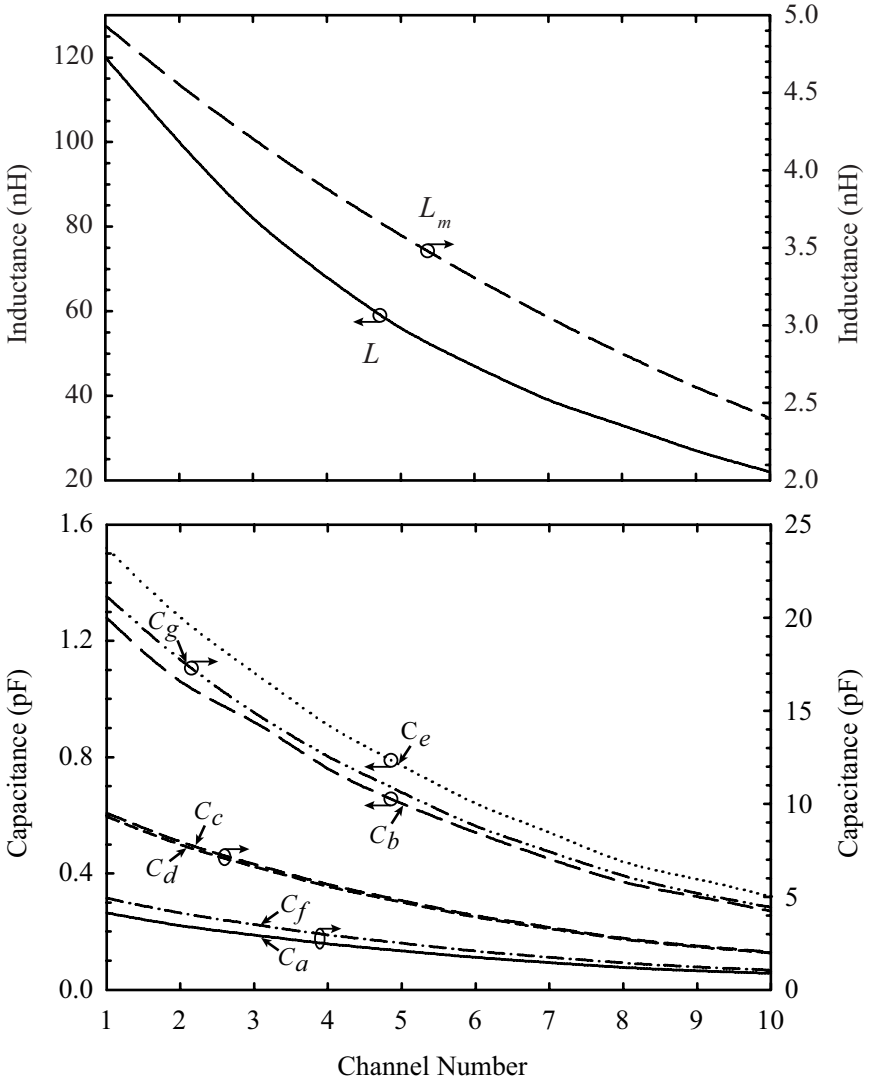

Figure 5.12: Lumped element component values for the 10-channel 200–1000 MHz 3rd-order cochlear channelizer (not shown, $C_0 = 2.75$ pF).

resulting S-parameters are exported to Agilent ADS and simulated together with the Modelithics component models. If necessary, lumped shunt capacitance is added or subtracted until agreement is obtained between the modeled and ideal filter responses. Then, the Sonnet model is modified to provide for the changed capacitance(s) and the simulation is redone. Using the combination of the Modelithics component library, ADS microstrip models, and Sonnet full-wave simulations, each channel took 2–4 iterations to match the expected filter response and the final component values and layout dimensions are found.

5.4.2 Measurements

The channelizer's S-parameters are measured using an Agilent E5071B vector network analyzer (VNA). A 2-port short-open-load-thru (SOLT) coaxial line calibration sets the reference planes at the coaxial connectors. Each channel's transmission response with respect to the channelizer input port ($S_{n,0}$, $1 \leq n \leq 10$) is measured by connecting VNA port 1 to the channelizer input (port 0) and VNA port 2 to the nth channel output (port n) while all other channel outputs are terminated in a 50 Ω load. The channelizer's input return loss ($S_{0,0}$) measurement is obtained in the same way (each channel output terminated in 50 Ω).

The measured and simulated S-parameters of the 10-channel channelizer are shown in Fig. 5.13 and Fig. 5.14 and a summary of channel characteristics appears in Table 5.1. The channels have an average fractional bandwidth of 17.5% and an aver-

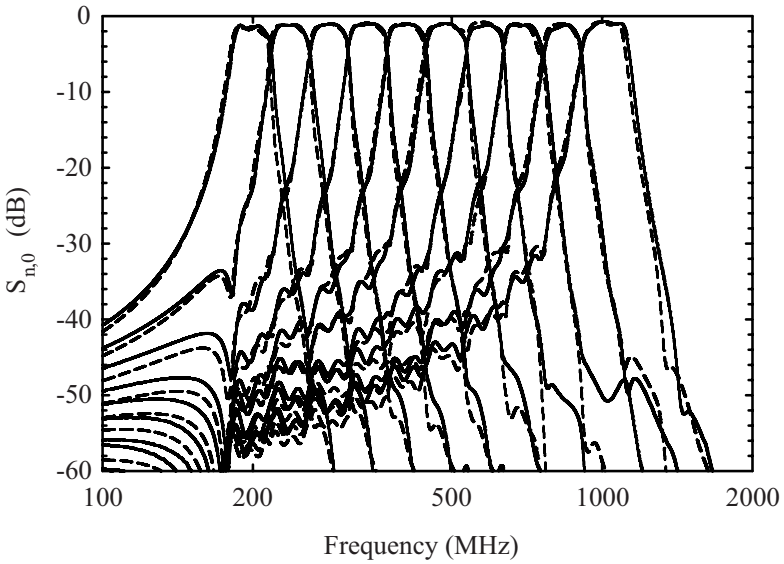

Figure 5.13: Measured (solid) and simulated (dashed) transmission response ($S_{n,0}$) of each channel of the 3rd-order cochlear channelizer.

age insertion loss of 1.12 dB at each channel's center frequency. The measurements agree very well with the simulations without any post-fabrication tuning.

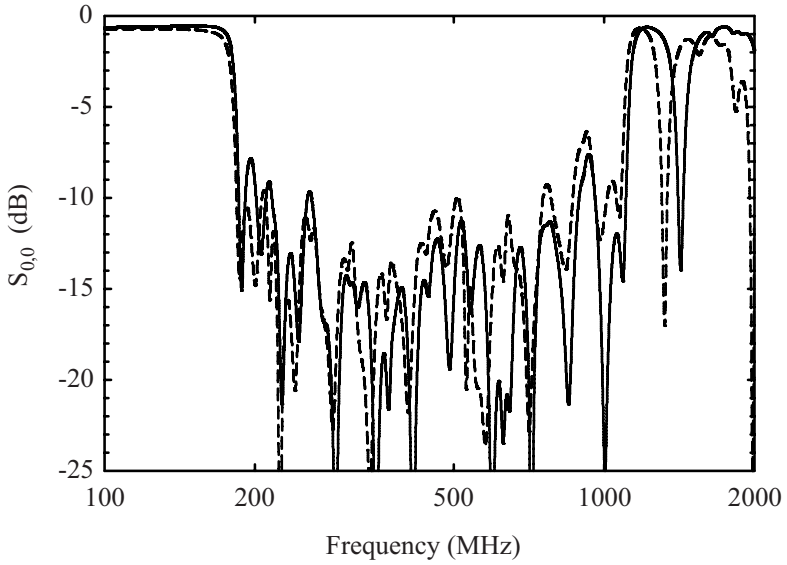

Figure 5.14: Measured (solid) and simulated (dashed) return loss ($S_{0,0}$) of the 3rd-order cochlear channelizer.

A single channel's (channel 5) narrow-band transmission response ($S_{5,0}$) and group delay are shown in Fig. 5.15 along with the simulated response for a stand-alone 3-pole filter with the topology shown in Fig. 5.7f. Compared with the stand-alone filter, the channelizer response has slightly higher rejection and an altered phase response. This results in an additional 2 ns of group delay at the center of channel 5.

Measurements of $S_{n,m}$ for $n \neq m$ are also performed to characterize the channelizer's channel-to-channel isolation. Isolation between channel 1 and channels 2–10 is given by $S_{1,2...10}$ (Fig. 5.16) while isolation between channel 10 and channels 1–9 is given by $S_{10,1...9}$ (Fig. 5.17). A particular channel's isolation to other channels closely follows its stopband response for channels located on the opposite side of the manifold; in this case, the coupling between different channels is through the inductive manifold only. However, a small amount of electromagnetic coupling occurs for channels on the same side of the manifold. This is seen as a rise in $S_{n,m}$ in the upper stopband of channel 1 (Fig. 5.16) and in the lower stopband of channel 10 (Fig. 5.17).

Table 5.1: Measured Channel Characteristics

Ch	f_n	$\Delta^\dagger$	I.L.‡
1	200 MHz	0.176	1.62 dB
2	239 MHz	0.169	1.20 dB
3	286 MHz	0.169	1.02 dB
4	341 MHz	0.175	1.01 dB
5	408 MHz	0.176	1.06 dB
6	490 MHz	0.179	0.93 dB
7	585 MHz	0.166	1.19 dB
8	696 MHz	0.173	1.22 dB
9	838 MHz	0.163	1.18 dB
10	1022 MHz	0.206	0.74 dB

†3-dB fractional bandwidth
‡Insertion loss at passband center (f_0)

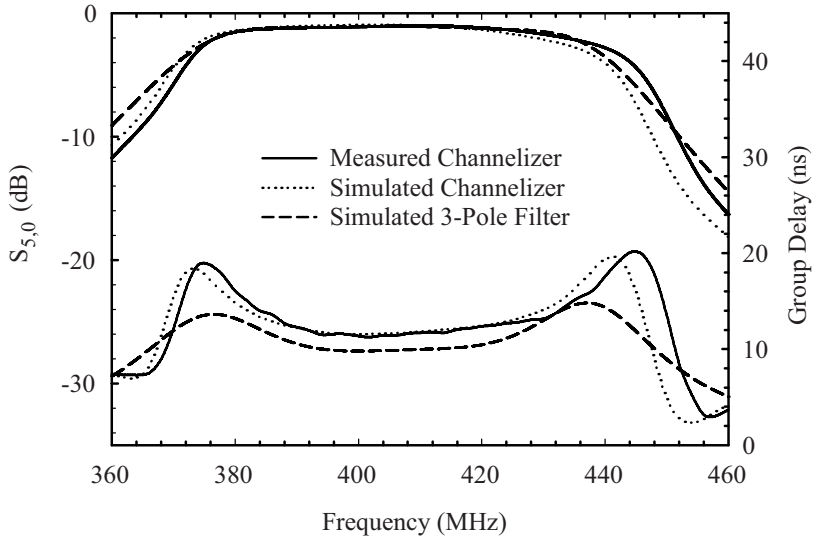

Figure 5.15: Transmission response (top) and group delay (bottom) of channel 5 of the 10-channel channelizer (simulated and measured) and the corresponding stand-alone 3-pole filter (simulated).

Physically adjacent channels (i.e. $1, 3, 5, \ldots$ and $2, 4, 6, \ldots$) couple by a maximum of about -60 dB, decreasing by 5 to 15 dB for each next-adjacent channel. The main

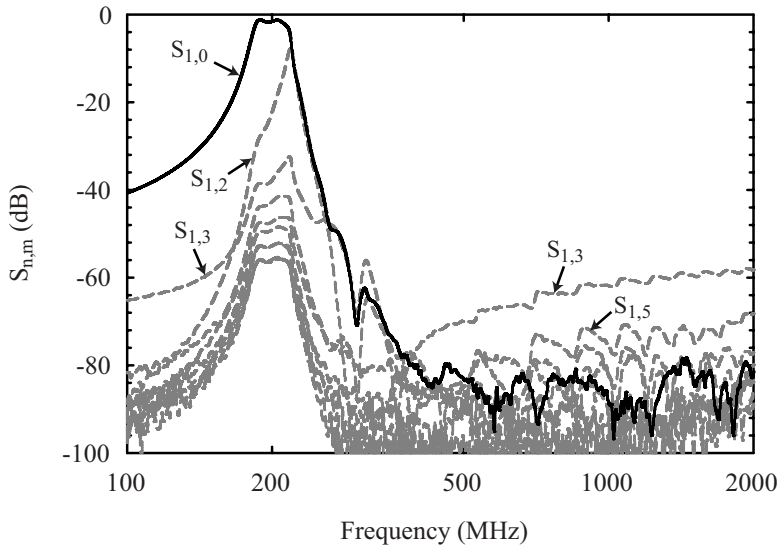

Figure 5.16: Measured $S_{1,0}$ (solid line) along with $S_{1,2\ldots10}$ (dashed lines) which gives channel 1's ($n = 1$) isolation to other channels ($m = 2 \ldots 10$). Isolation follows the upper stopband skirt of channel 1 with reduced isolation to channels located on the same side of the manifold ($n = 3, 5, 7, 9$) (Fig. B.3).

coupling mechanism between adjacent channels is electromagnetic coupling between the microstrip shunt capacitors. The largest shunt capacitors for each channel have lengths ranging from 6.6 mm (1 GHz) to 17.8 mm (200 MHz) or about 0.02–0.03 λ_g (guided wavelength) and are separated by a minimum of 7.6 mm (10× the substrate height) at the lowest frequency channels.

Since each filter has higher rejection in its upper stopband, lower frequency channels feature higher rejection of higher frequency channels. This is illustrated for three channel center frequencies (of channels 1, 5, and 10) in Fig. 5.18 which shows the power level of a particular frequency appearing at each channel port (the power is normalized so that a particular channel has 0 dB of rejection at its own center frequency).

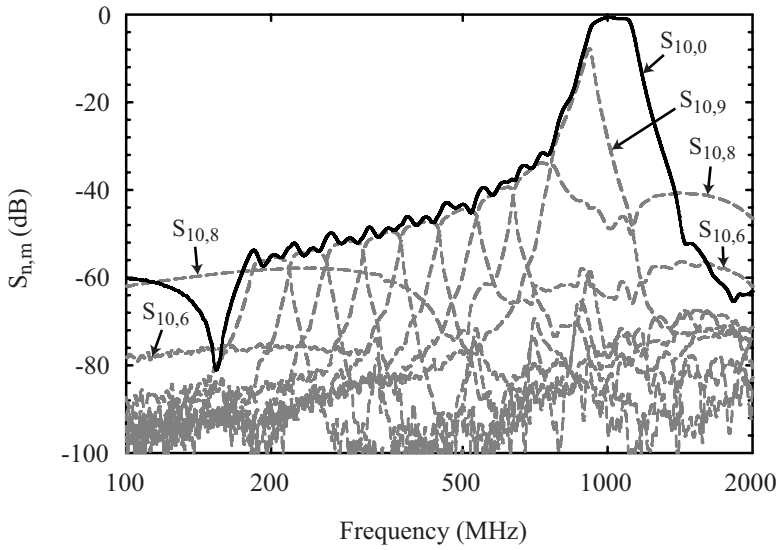

Figure 5.17: Measured $S_{10,0}$ (solid line) along with $S_{10,1\ldots9}$ (dashed lines) which gives channel 10's ($n = 10$) isolation to other channels ($m = 1 \ldots 9$). Isolation follows the lower stopband skirt of channel 10 with reduced isolation to channels located on the same side of the manifold ($n = 2, 4, 6, 8$) (Fig. B.3).

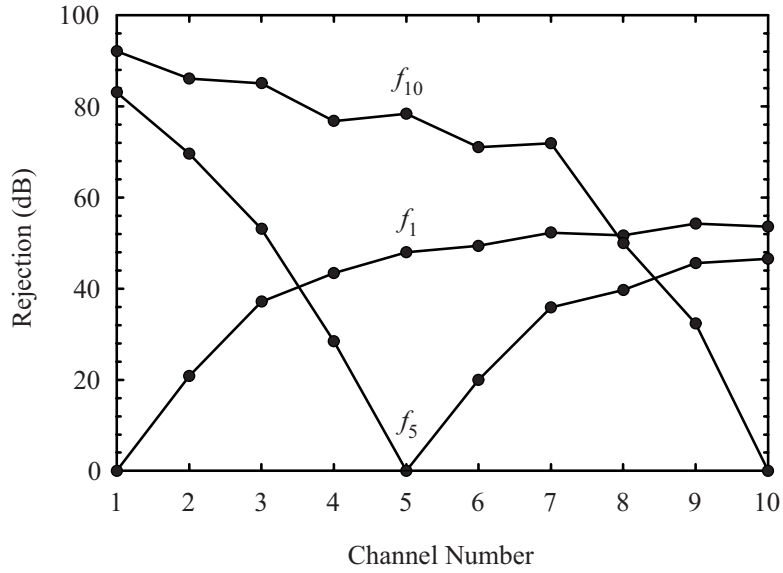

Figure 5.18: Measured rejection of channel 1, 5, and 10 center frequencies at all channel output ports.

5.4.3 Loss Analysis

To understand the loss mechanisms, we consider how power at a single frequency is distributed throughout the channelizer. At the center frequency of channel 5 (408 MHz), the percentage of the input power appearing at each output port is calculated from each channel's measured $|S_{n,0}|^2$. Likewise, the reflected power at the channelizer input is given by $|S_{0,0}|^2$. At 408 MHz, 78.3% of the power arrives at the channel 5 output (1.06 dB insertion loss), 0.937% appears at all other channel outputs, and 0.987% is reflected at the channelizer input (20.1 dB input return loss). Summing these powers results in 80.2% of the input power. Thus, the filter dissipates 19.8% of the input power corresponding to an effective loss of 0.96 dB. The dissipation is

Table 5.2: Sample Channel Power Distribution for Channel 5

	Power (%)
Channel 5 Output	78.3 (−1.06 dB)
Sum of Channel 1–4, 6–10 Outputs	0.937
Reflected at Input	0.987
Sum of all Power Contributions	80.2
Power Dissipated	19.8

primarily due to the channel filter inductor losses. Channel filter inductor (L) unloaded Q ranges from 130–150 at the channel center frequencies, while capacitor and manifold inductor (L_m) unloaded Qs range from 600–1200 and 200–350, respectively.

5.4.4 Power Handling for Transmit Applications

All channelizer components are passive and isotropic, and therefore the circuit's S-parameters are reciprocal. Thus, the channelizer can also be used as a transmit multiplexer where the individual channel ports are connected to transmitter outputs and the common manifold port serves as the multiplexer output.

The SMT components used in each channel filter limit the channelizer's single-tone average and peak power handling capability. The largest value inductor ($L(1)$=120 nH) used has the lowest maximum r.m.s. current rating of 1.5 A (it has the largest number of turns, thus the most resistance and loss). From simulation, this current corresponds to a maximum channelizer single-tone average input power of 27 W. The channelizer's capacitors must also be operated below their dielectric breakdown voltage. Of all the capacitors used, the SMT units have the lowest maximum voltage rating of 625 V corresponding to a channelizer peak input power of 60 W.

The inductive manifold composed of thin microstrip lines imposes an upper limit on the channelizer's multi-tone power handling capability. The maximum temperature rise ΔT of a microstrip line conductor is given by [66]

$$\Delta T = \frac{P_i h \left(1 - 10^{-\frac{Al}{10}}\right)}{lwk} \tag{5.26}$$

where l and w are the line length and width, h is the substrate height (all in [m]), P_i is the incident power (in [W]), k is the substrate thermal conductivity (in [$\mathrm{Wm^{-1}K^{-1}}$]), and A is the transmission line loss (in [dB/m]). The copper-clad PTFE/woven fiberglass substrate used in this design is rated for operation at a maximum of 125°C. This limit is first reached for the 0.635 mm wide manifold section nearest to the common port since this section carries the power of all 10 channels. For this channelizer, the maximum allowable average power is 14 W per channel (140 W total) at 25°C ambient (100°C temperature rise) and 5.6 W per channel (56 W total) at 85°C ambient (40°C temperature rise). The channelizer can be built on AlN or other substrates with higher thermal conductivity to increase its average power handling capability.

We have improved cochlea-like channelizers by using 3rd-order channel filters with the appropriate input impedance characteristic. The new channelizers feature channels with improved rejection, flat passband shape, and reduced insertion loss, and

retain the simple inductive manifold of earlier cochlear channelizers. The design procedure is easily extended to include 4th and higher-order channel filters.

5.5 Distributed 2nd-order Channelizer Simulations

A distributed-element cochlear channelizer is attractive for higher microwave frequencies. Above about 2 GHz, transmission line resonators become reasonably small allowing the realization of compact wideband channelizers. In addition, simulation is more straightforward and fabrication of multiple samples is possible in a monolithic process. To that end, design of a second-order planar channelizer covering 2 to 6 GHz was undertaken. Simulations were done of using end-coupled microstrip resonator filters. In the course of moving the design from ideal elements to a physical layout, a problems was encountered that shed light on the channel filter properties required for the cochlear channelizer topology. While this experiment did not result in a successful design, it demonstrates the importance of the maintaining the channel filter's series resonator-like wideband input impedance characteristics within a cochlear channelizer, and is included here to offer insight for further work.

5.5.1 Design Equations

At first glance, end-coupled $\lambda/2$ resonator filters appear to be a good candidate for use in a cochlear channelizer. The open-ended resonators, which behave like parallel resonant circuits, are coupled together through admittance inverters which transform their properties to series resonator-like response (i.e. they appear as open circuits in the filter stop-bands).

A distributed-element channelizer design follows the same procedure as the lumped-element one described earlier. One designs the individual filter sections with an input (manifold side) impedance less than 50 Ω, then designs a manifold of inductors (or

high impedance transmission line segments) using the single-order channelizer theory.

One additional problem comes with distributed filter implementations. If the channelizer covers more than about one octave, one must eliminate re-entrant filter responses that interfere with other channel filters. These spurious passbands are due to higher-order resonator responses and generally appear at $2mf_0$ for $\lambda/2$ types and at $3mf_0$ for $\lambda/4$ resonators ($m = 1, 2, 3 \ldots$), where f_0 is the passband center frequency. In parallel-coupled filters using $\lambda/4$ resonators, the first spurious passband appears closer to $2f_0$ due to a difference in even and odd mode phase velocities in the coupled sections [67]. In all of these distributed filters, this periodic behavior also decreases filter upper stop-band rejection since the transmission response begins to rise after the first pass-band instead of maintaining a monotonically decreasing skirt (as in lumped-element filters).

For end-coupled $\lambda/2$ filters, the spurious resonance problem is easily solved by used stepped impedance resonators (SIR). These resonators use alternating sections of low impedance (Z_1) and high impedance (Z_2) transmission lines. Analysis of the resonance condition of such a resonator shows that its spurious-free bandwidth increases with the ratio of the two impedances (Z_2/Z_1). Filters using these resonators are designed using the standard procedure for direct-coupled resonator filters given in [17] and [68] with modified expressions for the resonator susceptance slope parameters given in [69] and [70]. Other suggested techniques for spurious passband suppression that look promising for planar designs are given in [71] and [72].

The general model for a second-order ($N = 2$) filter is shown in Fig. 5.19a and the transmission line implementation of the model elements is shown in Fig. 5.19b,c. The lumped capacitors ($C_{n,n+1}$) are realized with either narrow microstrip gaps, interdigital capacitors, metal-insulator-metal (MIM) capacitors in a multi-layer planar process, or SMT devices. An example layout is shown in Fig. 5.23b along with a uniform impedance version for comparison (Fig. 5.23a).

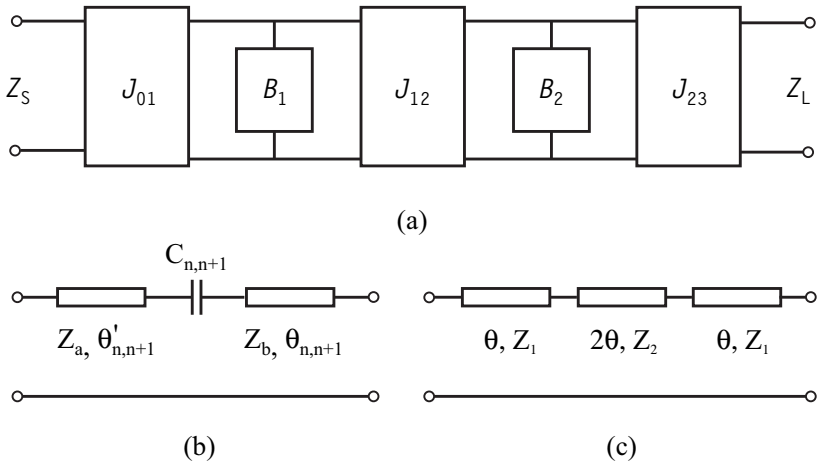

Figure 5.19: (a) Direct-coupled resonator filter model ($N = 2$) with ideal inverters ($J_{n,n+1}$) and parallel resonators (B_k), (b) inverter implementations with transmission lines and a series capacitor, and (c) stepped impedance resonator (SIR) with equal line lengths.

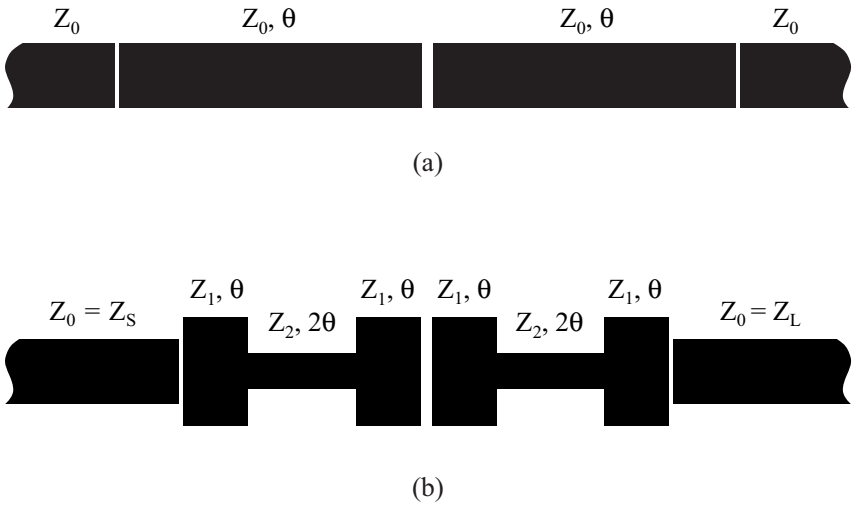

Figure 5.20: Second-order end-coupled $\lambda/2$ resonator filters using microstrip (a) uniform impedance and (b) stepped impedance resonators (SIR).

The design equations for the 2nd-order $\lambda/2$ SIR filter are summarized below, using the definitions in Table 5.3. For an SIR composed of two low impedance (Z_1) segments of length θ on each end and one middle, high impedance segment (Z_2) of length 2θ,

Table 5.3: SIR Filter Impedance Definitions

Z_S	$\equiv$	Filter input impedance [Ω]
Z_L	$\equiv$	Filter output impedance [Ω]
Z_1	$\equiv$	Resonator impedance (low) [Ω]
Z_2	$\equiv$	Resonator impedance (high) [Ω]

the expression for the length is given by

$$\theta = \tan^{-1}\sqrt{k} \tag{5.27}$$

where k is the ratio of the impedances,

$$k = \frac{Z_1}{Z_2} \tag{5.28}$$

and the frequency of the first spurious response f_{s1} increases with greater ratios of Z_2 to Z_2 (i.e. smaller k) [69],

$$\frac{f_{s1}}{f_0} = \frac{\pi}{2\tan^{-1}\sqrt{k}}. \tag{5.29}$$

The susceptance slope parameter of this SIR is

$$b = 2\theta Y_{res} = \frac{2\theta}{Z_1} \tag{5.30}$$

where Y_{res} is the admittance of the coupled resonator (the low impedance section in this case since it appears at the ends of each resonator). Using (5.30) in the standard form of direct-coupled resonator filters with J-inverter-coupled parallel resonators

[17, 40] gives the inverter values

$$J_{n,n+1} = \begin{cases} \sqrt{\dfrac{\Delta\, b}{Z_S g_0 g_1}} & n = 0 \\ \dfrac{\Delta\, b}{\sqrt{g_1 g_2}} & n = 1 \\ \sqrt{\dfrac{\Delta\, b}{Z_L g_0 g_1}} & n = 2 \end{cases} \tag{5.31}$$

The inverters can be realized by a Pi-network of capacitors or with the transmission line and capacitor network shown in Fig. 5.19b. The latter network's transmission line lengths are negative for positive capacitance values. This circuit is attractive since the negative transmission line lengths are absorbed in adjacent lines of the same characteristic impedance. In addition, this inverter can be designed with arbitrary impedances for each transmission line. For example, the input inverter J_{01} is designed with a $Z_a = 50\ \Omega$ (the filter input impedance) and $Z_b = Z_1$ (the low impedance resonator section). The transmission line lengths are given by [73],

$$\theta'_{n,n+1} = \frac{1}{2}\left(p_{n,n+1} + q_{n,n+1}\right), \qquad n = 0, 1, 2 \tag{5.32}$$

$$\theta_{n,n+1} = \frac{1}{2}\left(p_{n,n+1} - q_{n,n+1}\right), \qquad n = 0, 1, 2 \tag{5.33}$$

where p, q, and $\overline{B}$ are

$$p_{n,n+1} = \begin{cases} -\tan^{-1}\left[\left(Z_S/Z_1 + 1\right)\overline{B}_{01}\right] & n = 0 \\ -\tan^{-1}\left(2\overline{B}_{12}\right) & n = 1 \\ -\tan^{-1}\left[\left(Z_L/Z_1 + 1\right)\overline{B}_{23}\right] & n = 2 \end{cases} \tag{5.34}$$

$$q_{n,n+1} = \begin{cases} -\tan^{-1}\left[\left(Z_S/Z_1 - 1\right)\overline{B}_{01}\right] & n = 0 \\ 0 & n = 1 \\ -\tan^{-1}\left[\left(Z_L/Z_1 - 1\right)\overline{B}_{23}\right] & n = 2 \end{cases} \tag{5.35}$$

$$\overline{B}_{n,n+1} = \begin{cases} \left\{\left[\left(J_{01}Z_1\right)^2 - 1\right]\left(Z_S/Z_1\right)^2 + \left(J_{01}Z_1\right)^{-2} - 1\right\}^{-1/2} & n = 0 \\ \left\{\left[\left(J_{12}Z_1\right)^2 - 1\right] + \left(J_{12}Z_1\right)^{-2} - 1\right\}^{-1/2} & n = 1 \\ \left\{\left[\left(J_{23}Z_1\right)^2 - 1\right]\left(Z_L/Z_1\right)^2 + \left(J_{23}Z_1\right)^{-2} - 1\right\}^{-1/2} & n = 2 \end{cases} \tag{5.36}$$

and the inverter capacitor values are given by

$$C_{n,n+1} = \frac{\overline{B}_{n,n+1}}{\omega_0 Z_1}, \qquad n = 0, 1, 2. \tag{5.37}$$

5.5.2 Simulation Results

A 10-channel, 2 to 6 GHz channelizer was designed using SIR channel filters. The filter $\lambda/2$ resonators used alternating sections of $Z_1 = 20\ \Omega$ and $Z_2 = 90\ \Omega$ placing the first spurious filter passband at approximately $3.6f_0$. For the lowest frequency channel centered at 2 GHz, the first re-entrant response occurs above 7 GHz (Fig. 5.21) without significantly affecting the desired passband shape (Fig. 5.22). Each channel was designed with $\Delta = 12.2\%$ and an input impedance of 20 Ω. The manifold used an L_0 of 0.400 nH and exponential taper of a $= 0.5$. A proposed layout for this channelizer is shown in Fig. 5.23. The manifold inductors are implemented with high impedance microstrip segments and series capacitances are done with MIM capacitors. A full-wave simulation was done of each resonator section using Sonnet and the results imported into ADS for a linear circuit simulation with ideal manifold and coupling elements used to tune parasitic effects. Once the channel filters and

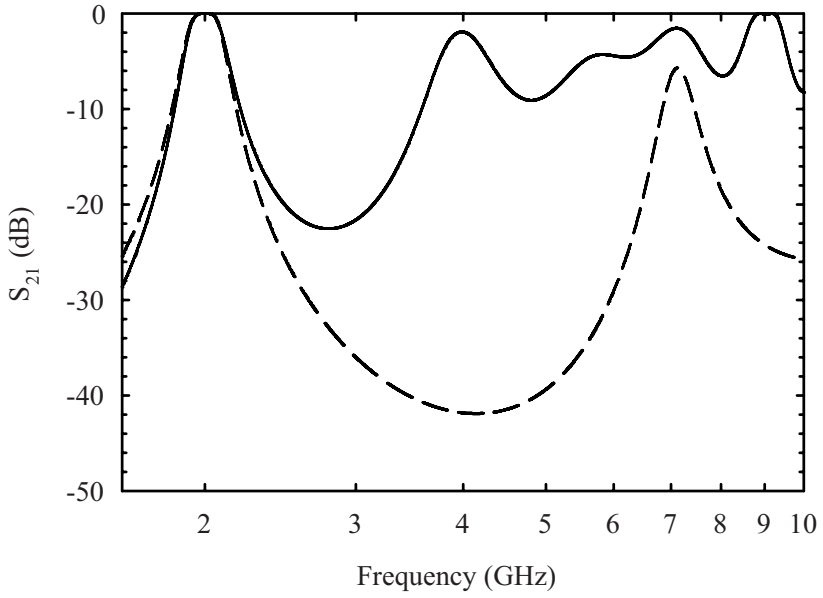

Figure 5.21: Wideband simulated transmission (S_{21}) of 2 GHz filters using constant-impedance (solid line) and stepped impedance (dashed line) resonators.

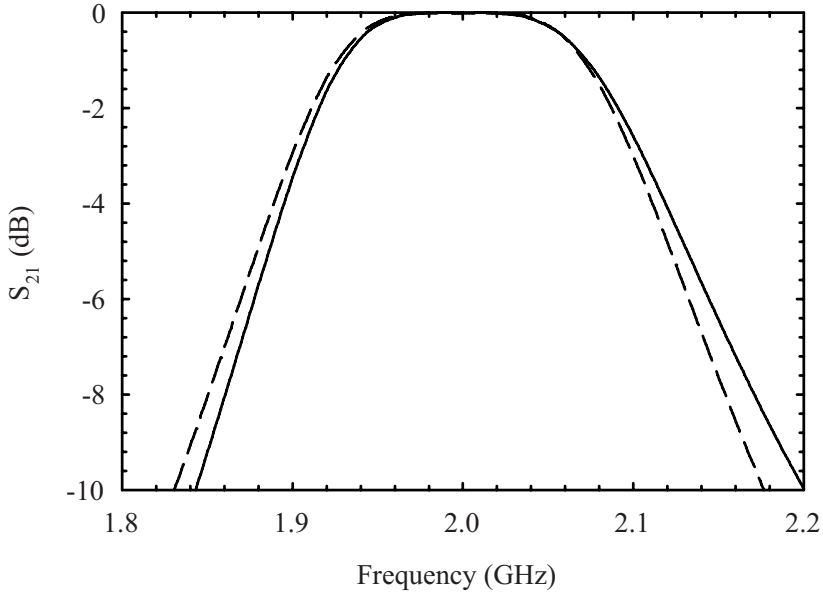

Figure 5.22: Simulated transmission (S_{21}) of 2 GHz filters using constant-impedance (solid line) and stepped impedance (dashed line) resonators.

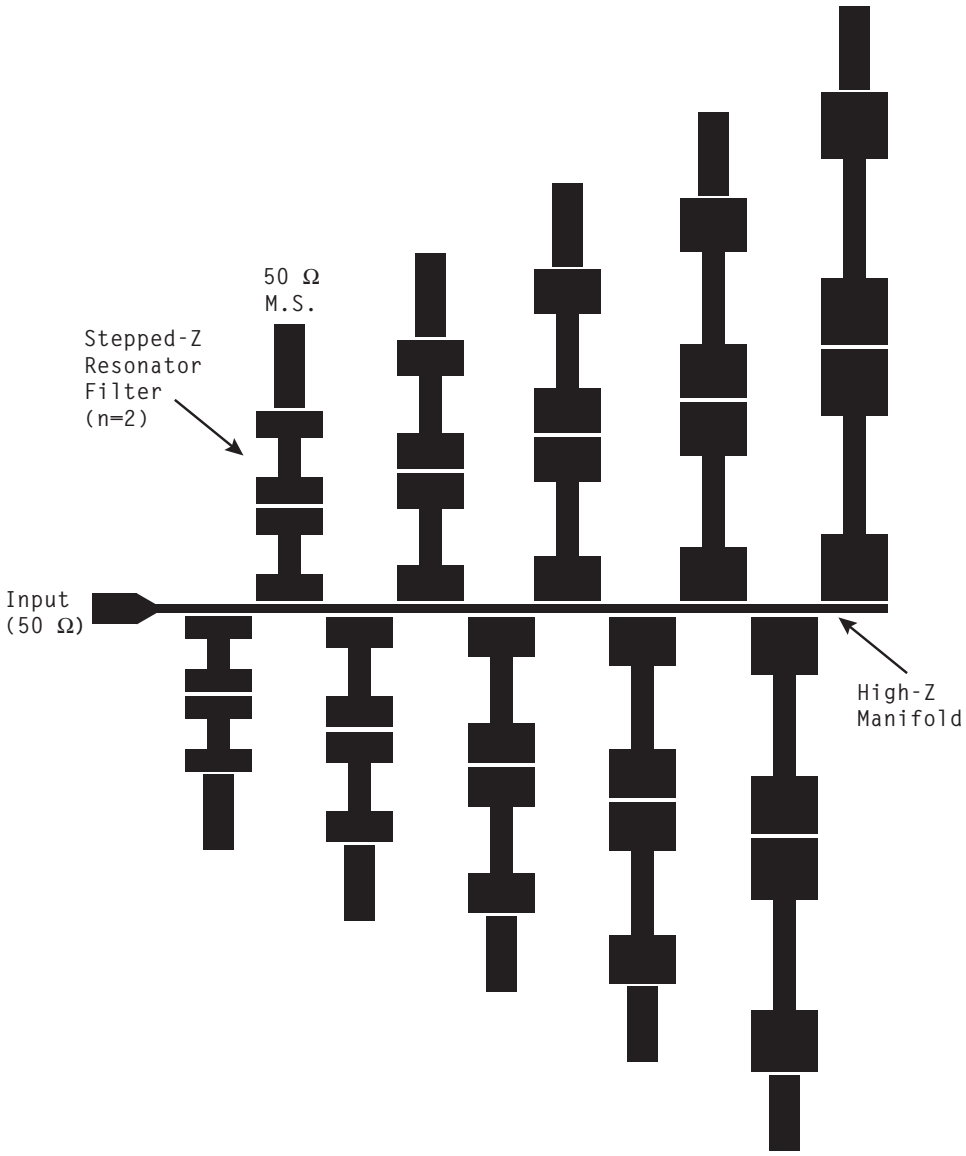

Figure 5.23: Proposed layout for second-order cochlear channelizer using end-coupled stepped-impedance resonator filters.

manifold were connected in simulation a critical problem with the channel filter's response was identified.

The end-coupled $\lambda/2$ filters require negative-value transmission lines for the inverter sections (Fig. 5.19b) located in between each resonator as well as at the input and output ports. For inter-resonator coupling, the negative transmission lines are physically absorbed into the circuit by reducing the resonator lengths. At the in-

put and output, however, no physical transmission line exists. This is dealt with by setting the inverter transmission line impedance equal to the port impedance. Thus, any length of matched transmission does not alter the magnitude of the filter's transmission response, and the length can be conveniently set to zero (or some other convenient length). However, this does alter the filter's phase response by a negative amount equal to the inverter line section (plus any additional physical line length used). This is seen on a Smith chart as rotating S_{11} negative θ'_{01} degrees (clockwise), moving the high frequency response from a near-open circuit into the capacitive region (Fig. 5.5b). The effect of this impedance transformation on the channelizer circuit is an in-band resonance with the inductive impedance seen at the manifold, producing a transmission zero at in the channelizer bandwidth. This is clearly seen in the simulated transmission plots in Fig. 5.24. By placing ideal negative transmis-

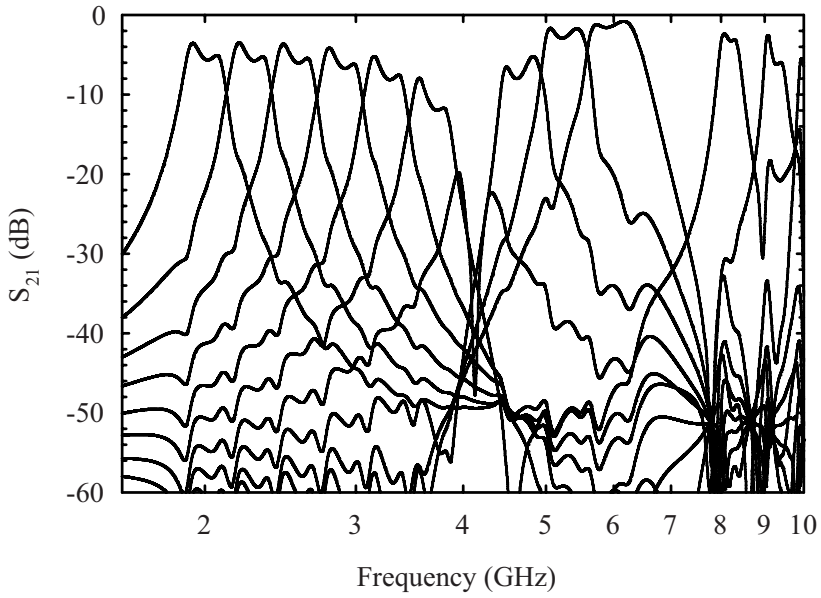

Figure 5.24: Simulated transmission (S_{21}) of each channel of a 2nd-order channelizer using end-coupled resonator filters ($\theta_{01} = 0°$) at filter input).

sion line lengths at the filter inputs (the manifold-filter interfaces), as in the ideal circuit model, the desired channelizer response is obtained as shown in Fig. 5.25.

Unfortunately, a solution to this problem has not yet been found. An obvious first

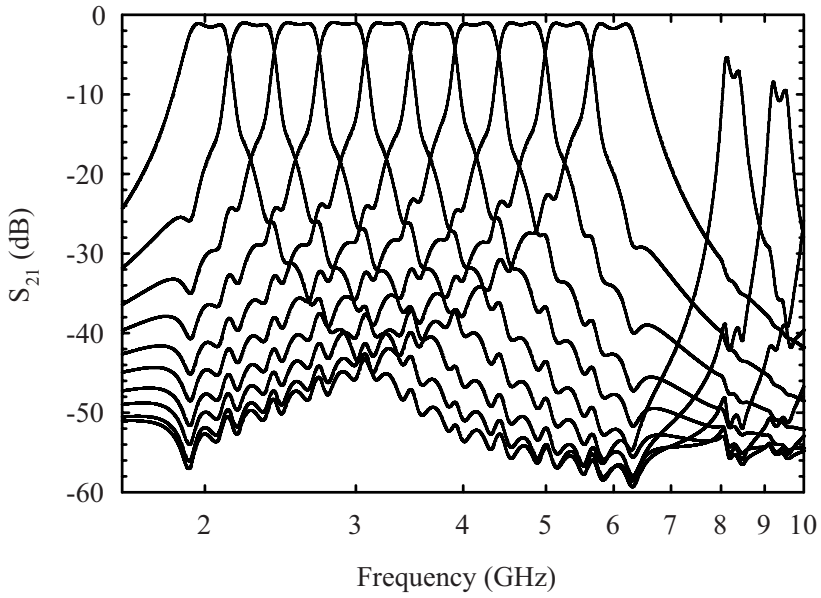

Figure 5.25: Simulated transmission (S_{21}) of each channel of a 2nd-order channelizer with negative transmission line segment at the filter input ($\theta_{01} = -22.5°$).

attempt adds an additional $\phi = 180°$ of line at the filter input which, combined with the negative inverter length, is slightly less than $\lambda/2$ and is realizable. Within the passband, this causes no change in the filter amplitude and phase response (except for an additional 180° of transmission phase). However, at frequencies in the stop-bands, this line section introduces $2\phi f/f_0$ degrees of input impedance phase shift (the factor of 2 is due to the reflection coefficient accruing twice the phase shift as it traverses the line in the forward and reverse direction). Thus, at $f_0/2$ and $3/2f_0$ this causes the input impedance to appear as a short circuit (and all other predominantly reactive impedances as Γ makes a complete rotation around the Smith chart). In a cochlear channelizer which requires filters to appear as near-open circuits in their stop-bands, this input impedance behavior destroys the wideband response by either reflecting signals back to the input before they reach the resonant channel or by producing

in-band transmission zeros through a filter-manifold resonance. Other attempts at a solution have tried high-pass networks to provide a negative phase, but have not proven worthwhile.

Chapter 6

Conclusion

6.1 Summary of Work

The work presented in this thesis introduces an RF and microwave multiplexer topology well-suited for applications requiring multi-octave coverage with greater than ten channels. Single-order cochlea-like channelizers offer a pre-selection scheme for wideband receiver front ends in a compact circuit with a simple design procedure. The basic circuit model is found through an electrical-mechanical analogy of a one-dimensional mammalian cochlea model. Versions with 20 channels covering 20 to 90 MHz in constant fractional bandwidth as well as constant absolute bandwidth channels are demonstrate the theory and design procedure. A planar version covering 2 to 7 GHz in 15 channels is also presented. The cochlea-like circuit is extended to include conventional (all-pole ladder type) higher-order filter sections with specific input impedance behavior. Higher-order channelizers using conventional RF and microwave filters can be used in both input (receiver) and output (transmit) multiplexers, with performance on par with other modern multiplexer types. The cochlear types, however, require little or no optimization to design units with many channels channels, and can be realized without the need for post-fabrication tuning. A version covering 200 MHz to 1 GHz in 10 channels demonstrates this idea.

6.2 Future Work

The cochlea-like channelizer topology, in both single-order and higher-order forms, is readily extended to other frequency ranges and bandwidths using different filter topologies and available technologies. Surface mount technology can be used up to about 2 GHz, while lumped-element planar monolithic or hybrid circuits can be used from 2 to 6 GHz. The main limitation to implementation is the chosen channel filter's wideband input impedance characteristics, while channelizer bandwidth and filter center frequencies are limited by the parasitics in the technology used. So far, any channel filter that behaves as a series resonator over the channelizer bandwidth has worked well in this multiplexer topology. Lumped-element filters in this category include those incorporating a series resonator, or its equivalent, at the filter input. In addition to the tubular topology presented in Chapter 5, filters using parallel resonators and input admittance inverters can be designed to work well. One example is the series capacitor-coupled parallel resonator type, which has proved successful in circuit simulation. Similar filter topologies using higher Q resonators, such as helical types, likewise can work well in cochlear channelizers. All of the mentioned filter types are particularly attractive since their lumped element parasitic capacitances to ground are easily absorbed in the filter network components. As with any type passive filter, a given technology's resonator Q also determines the useful fractional bandwidth of each channel filter for a given filter order (or amount of stop-band rejection) where Qs above about 200 are needed for 3rd-order and higher filters with fractional bandwidths less than about 10%. Due to their extremely high unloaded Q lumped-element components, superconducting technologies offer one obvious way to take advantage of the compact cochlear channelizer topology. Finally, the development of distributed channel filters suitable for cochlear multiplexers is important for creating wideband, channelizers especially above 6 GHz in monolithic processes. This is particularly challenging, as most distributed microwave filters generate a stop-

band input impedance that interferes with a wideband cochlea-like response, at least without significant immittance compensation and computer optimization.

Appendices

Appendix A

Channelizer Design Code

This appendix includes functions written for MATLAB version 7.1 [74] which calculate the coefficients and component values for single-order channelizers in [62] and the manifold inductors for higher-order channelizers as in [75]. Both functions use a numerical integration procedure written by Rob White.

MATLAB function `coefcfb.m` for generating constant fractional bandwidth (CFB) single-order channelizer coefficients:

```
function[A1,A2,A3,alpha,alpha2,Q] = coefcfb(lag,N,NN,fmin,fmax,R)
% COEFCFB calculates the coefficients for the single-order
% cochlear channelizer described in "Cochlea-based RF channelizing
% filters", IEEE Transactions on Circuits and Systems I, by Galbraith,
% White, Lei, Grosh, and Rebeiz.
%
% Inputs: phase lag (radians), N (number of channels), channel crossover
% factor NN (no units), minimum and maximum frequency (MHz),
% and resonator resistor R
%
% Outputs: coefficients A1, A2, A3, alpha, alpha2 (exponential fit),
% and required resonator unloaded Q (all optional)
%
% Syntax: [A1,A2,A3,alpha,alpha2,Q] = coefcfb(lag,N,NN,fmin,fmax,R)
alpha_0 = log(fmax/fmin);
Q = 1/NN*(exp(1/(N-1)*alpha_0)+1)/(exp(1/(N-1)*alpha_0)-1);
A1 = (1/(fmax*2*pi)^2); % To get fmax resonance at x = 0
alpha = log((fmax/fmin)^2); % To get fmin resonance at x = 1
A2 = sqrt(A1)/Q; % To get the desired Q for each resonator

% Use WKB integral to approximate phase lag and step down the
% transmission line, setting L1*C at incremented steps to get
% the desired phase lag at the center frequency for each location.
```

```
% Make frequency span from fmin to fmax (log spacing))
w = logspace(log10(fmax*2*pi*0.9),log10(fmin*2*pi*1.1),100);
% Make index i_f for frequency points
for i_f = 1:length(w),
    % Set current frequency for index i_f
    omega = w(i_f);
    % Set x-coordinate for current frequency
    xbp(i_f) = log(1./(A1*(omega.^2)))./alpha;
    % Calculate P (=L1*C) for the first x partition
    if i_f == 1
        x = linspace(0,xbp(i_f),100);
        h = -omega^2./(A1*exp(alpha*x).*omega.^2-1-A2... % minus A2!
        *exp(0.5*alpha*x)*sqrt(-1).*omega);
        integral=trapz(x,sqrt(h));
        % P(n) is a discrete function for L1*C
        P(i_f) = (lag/real(integral))^2;
    % Calculate L1*C for later xbp
    else
        lag_so_far = 0;
        % Make index for previous partitions
        for i_x = 1:i_f-1,
            % Set integration interval for only the first partition
            if i_x == 1,
                x = linspace(0,xbp(1),100);
            % Set integration interval for later partition
            else
                x = linspace(xbp(i_x-1),xbp(i_x),100);
            end
            % Make a running sum of integrals for previous segments
            lag_so_far = lag_so_far+...
            trapz(x,sqrt(-P(i_x)*omega^2./(A1*exp(alpha*x)...
            .*omega.^2-1-A2*exp(0.5*alpha*x)*sqrt(-1).*omega)));
        end
        % Calculate current P for
        x = linspace(xbp(i_f-1),xbp(i_f),100);
        h = -omega^2./(A1*exp(alpha*x).*omega.^2-1-A2...
        *exp(0.5*alpha*x)*sqrt(-1).*omega);
        integral=trapz(x,sqrt(h));
        P(i_f) = (real((lag-lag_so_far))/real(integral))^2;
    end
end

% Fit P function to an exponential
x = linspace(0,1,length(P)); [fit,tempFunction]...
        = polyfit(xbp,real(log(P)),1);
A3 = exp(fit(2));
% alpha2 will give a more accurate phase than alpha
```

```
alpha2 = fit(1);

% Now re-define P as this fit:
P = A3*exp(alpha2*xbp);
for i_f = 2:length(w),
    omega = w(i_f);
    xbp(i_f) = log(1./(A1*omega.^2))./alpha;
    x = linspace(0,xbp(i_f),i_f);
    g2 = -P(1:i_f).*omega^2./(A1*exp(alpha*x).*omega.^2-1-A2...
    *exp(0.5*alpha*x)*sqrt(-1).*omega);
    phase(i_f) = trapz(x,sqrt(g2));
end

% plot phase versus frequency to check approximation
semilogx(w/(2*pi),phase,'x');
% Print out results
disp(' ');
disp(' ');
disp('--------------------------');
disp(' Filter characteristics:');
disp([' fmax = ',num2str(fmin/1e6),' MHz']);
disp([' fmax = ',num2str(fmax/1e6),' MHz']);
disp([' N = ',num2str(N)]);
disp([' NN (crossover factor) = ',num2str(NN)]);
disp([' Q = ',num2str(Q)]);
disp('--------------------------');
disp(' CFB Model Constants:');
disp([' A1 =',num2str(A1)]);
disp([' A2 = ',num2str(A2)]);
disp([' A3 = ',num2str(A3)]);
disp([' alpha = ',num2str(alpha)]);
disp([' alpha2 = ',num2str(alpha2)]);
disp('--------------------------');
% Calculate component values from constants
% Make x-vector
x = linspace(0,1,N)';
% Compute dx based on N and a device length of 1:
dx = 1/N;
Rfinal = ones(N,1)*R; %Ohms
% 1/(G*dx) = R so:
G = 1./(Rfinal*dx);
% Calculate C per unit length
C = G.*A2.*exp(0.5*alpha*x);
% Multiply by dx to get C
Cfinal = C*dx;
% Calculate L1, L2
L1 = A3*exp(alpha2*x)./C;
```

```
L2 = A1*exp(alpha*x)./C;
L1final = L1*dx;
L2final = L2/dx;
% Flip order, so channel 1 is at fmin
L1VAL = flipud(L1final);
L2VAL = flipud(L2final);
CVAL = flipud(Cfinal);
f0final = (1./(2*pi*sqrt(L2VAL.*CVAL)))./1e6;
% Display component values
disp(' Component Values:');
for ii=1:N
    disp([' L1_',num2str(ii),' = ',num2str(L1VAL(ii)*1e9),' nH']);
end
disp('--------------------------');
for ii=1:N
    disp([' L2_',num2str(ii),' = ',num2str(L2VAL(ii)*1e9),' nH']);
end
disp('--------------------------');
for ii=1:N
    disp([' C_',num2str(ii),' = ',num2str(CVAL(ii)*1e12),' pF']);
end
disp('--------------------------');
disp([' R = ',num2str(Rfinal(1)),' Ohms']);
disp('--------------------------');
disp(' ');
```

MATLAB function `coefcab.m` for generating constant absolute bandwidth (CAB) single-order channelizer coefficients:

```
function[B1,B2,B3,B4,delta_f] = coefcab(lag,N,fmin,fmax,R)
% COEFCAB calculates the coefficients for the single-order constant
% absolute bandwidth (CAB) cochlear channelizer described in
% "Cochlea-based RF channelizing filters", IEEE Transactions on
% Circuits and Systems I, by Galbraith, White, Lei, Grosh, and Rebeiz.
%
% Inputs: phase lag (radians), N (number of channels), minimum and
% and maximum frequency (MHz), resonator R
%
% Outputs: coefficients B1, B2, B3, and B4
% and required absolute bandwidth (all optional)
%
% Syntax: [B1,B2,B3,B4,delta_f] = coefcab(lag,N,fmin,fmax,R)
B1 = fmax*2*pi; % To get fmax resonance at x = 0
B2 = fmin*2*pi-B1; % To get fmin freq resonance at x = 1
delta_f = (fmax-fmin)/(N-1);
delta_w = delta_f*2*pi;
```

```
% Use WKB integral to approximate phase lag and step down the
% transmission line, setting L1*C at incremented steps to get
% the desired phase lag at the center frequency for each location.

% Make frequency span from fmin to fmax (lin spacing))
w = linspace(fmax*2*pi*0.9,fmin*2*pi*1.1,100);

% Make index i_f for frequency points
for i_f = 1:length(w),
    % Set current frequency for index i_f
    omega = w(i_f);
    % Set x-coordinate for current frequency
    xbp(i_f) = (omega-B1)/B2;
    % Calculate P (=L1*C) for the first x partition
    if i_f == 1
        x = linspace(0,xbp(i_f),100);
        h = -omega^2./(1./(B1+B2*x).^2.*omega.^2-1+...
            delta_w./(B1+B2*x).^2*sqrt(-1).*omega);
        integral = trapz(x,sqrt(h));
        P(i_f) = (lag/real(integral))^2;
    % Calculate L1*C for later xbp
    else
        lag_so_far = 0;
        % Make index for previous partitions
        for i_x = 1:i_f-1,
            % Set integration interval for only the first partition
            if i_x == 1,
                x = linspace(0,xbp(1),100);
            % Set integration interval for later partition
            else
                x = linspace(xbp(i_x-1),xbp(i_x),100);
            end
            % Make a running sum of integrals for previous segments
            lag_so_far = lag_so_far+...
                trapz(x,sqrt(-P(i_x)*omega^2./...
                (1./(B1+B2*x).^2.*omega.^2-1+...
                delta_w./(B1+B2*x).^2*sqrt(-1).*omega)));
        end
        % Calculate current P for
        x = linspace(xbp(i_f-1),xbp(i_f),100);
        h = -omega^2./(1./(B1+B2*x).^2.*omega.^2-1+...
            delta_w./(B1+B2*x).^2*sqrt(-1).*omega);
        integral = trapz(x,sqrt(h));
        P(i_f) = (real((lag-lag_so_far))/real(integral))^2;
    end
end
```

```
% Fit P function to the polynomial function
x = linspace(0,1,length(P));
[fit,tempFunct] = polyfit(xbp,real(sqrt(1./P)),1);
B4 = fit(1);
B3 = fit(2);

% Now re-define P as this fit:
P= 1./(B4*xbp+B3).^2;
for i_f = 2:length(w),
    omega = w(i_f);
    xbp(i_f) = (omega-B1)/B2;
    x = linspace(0,xbp(i_f),i_f);
    g2 = -P(1:i_f).*omega^2./(1./(B1+B2*x).^2.*omega.^2-1+...
        delta_w./(B1+B2*x).^2*sqrt(-1).*omega);
    phase(i_f) = trapz(x,sqrt(g2));
end

% plot phase versus frequency to check approximation
plot(w/(2*pi),real(phase),'x');

% Print out results
disp(' ');
disp(' ');
disp('--------------------------');
disp(' Filter characteristics:');
disp([' fmax = ',num2str(fmin/1e6),' MHz']);
disp([' fmax = ',num2str(fmax/1e6),' MHz']);
disp([' N = ',num2str(N)]);
disp([' delta_f = ',num2str(delta_f/1e6),' MHz']);
disp('--------------------------');
disp(' CAB Model Constants:');
disp([' B1 =',num2str(B1)]);
disp([' B2 = ',num2str(B2)]);
disp([' B3 = ',num2str(B3)]);
disp([' B4 = ',num2str(B4)]);
disp('--------------------------');
% Calculate component values from constants
% Make x-vector
x = linspace(0,1,N)';
% Compute dx based on N and a device length of 1:
dx = 1/N;
Rfinal = ones(N,1)*R; %Ohms
% 1/(G*dx) = R so:
G = 1./(Rfinal*dx);
% Calculate C per unit length
C = G.*delta_w./(B1+B2*x).^2;
```

```
% Multiply by dx to get C
Cfinal = C*dx;
% Calculate L1, L2
L1=1./(B3+B4*x).^2./C;
L2=1./(B1+B2*x).^2./C;
L1final=L1*dx;
L2final=L2/dx;
% Flip order, so channel 1 is at fmin
L1VAL = flipud(L1final);
L2VAL = flipud(L2final);
CVAL = flipud(Cfinal);
f0final = (1./(2*pi*sqrt(L2VAL.*CVAL)))./1e6;
% Display component values
disp(' Component Values:');
for ii=1:N
    disp([' L1_',num2str(ii),' = ',num2str(L1VAL(ii)*1e9),' nH']);
end
disp('--------------------------');
for ii=1:N
    disp([' L2_',num2str(ii),' = ',num2str(L2VAL(ii)*1e9),' nH']);
end
disp('--------------------------');
for ii=1:N
    disp([' C_',num2str(ii),' = ',num2str(CVAL(ii)*1e12),' pF']);
end
disp('--------------------------');
disp([' R = ',num2str(Rfinal(1)),' Ohms']);
disp('--------------------------');
disp(' ');
```

Appendix B

Planar Low-Loss Double-Tuned Transformers

The work in this appendix was pursued along with the planar microwave channelizer described in Chapter 4. Initially, as in the lower frequency versions, a transformer was going to be used for output impedance matching of each channel's resonator, motivating the development of suitably broadband transformers. While the channelizer design ultimately used a simpler LC network to accomplish this, transformers were included in the fabrication run resulting in a good test of their theory and a demonstration of their performance.

Here, a state-of-the-art, planar double-tuned transformer using high-Q, micromachined spiral inductors and integrated capacitors is presented. This circuit provides a 4:1 impedance transformation over a 30% bandwidth centered at 4.06 GHz, with a minimum insertion loss of 1.50 dB. The fabricated circuit occupies a total area of 440 $\times$ 500 μm^2 and finds application in power amplifier and other matching applications. An accurate lumped-element circuit model and design trade-offs are also presented.

Conventional transformers based on two magnetically-coupled inductors are commonly used in communications systems from audio to microwave frequencies. In technologies where high-permeability core materials are available, usually at frequencies below 1 GHz in non-integrated electronics, transformers with a magnetic coupling factor (k) of nearly one are possible. Such near-ideal transformers offer very wide bandwidths, often in excess of three decades (limited only by inductor parasitic capacitance).

In integrated circuits, possible k values are usually limited to less than 0.8 causing conventional transformer bandwidth to rapidly decrease. To overcome this, a transformer can be made with tuned circuits using capacitors in shunt with the primary and secondary inductors. This type of circuit has been used in interstage coupling between active, low frequency, often narrow-band intermediate frequency (IF) stages, usually implemented as 3-D solenoidal inductors with variable coupling provided by a moveable magnetic core. By applying this circuit to modern integrated circuit technology at microwave frequencies, one is able to perform an impedance transformation over a wide bandwidth using easily-achieved k values while conveniently absorbing inductor parasitic shunt capacitances. Such an integrated double-tuned transformer provides low insertion loss when the lumped element unloaded Qs are above 20.

B.1 Modeling and Design Trade-Offs

The lumped-element circuit model for the double-tuned transformer is shown in Fig. B.1a. The primary and secondary windings are modeled by L_1 and L_2 with resonating capacitances C_1 and C_2. The model accounts for parasitics including the inductor and capacitor loss (i.e. resonator unloaded Q) modeled by R_1 and R_2 and the electric coupling between the transformer primary and secondary (C_{12}). The inductor parasitic capacitances are absorbed into C_1 and C_2. A magnetic coupling factor k between L_1 and L_2 is implied and defined as $k \equiv M/\sqrt{L_1 L_2}$, where M is the mutual inductance. Although the impedances connected to the two ports can be complex, they are assumed real in this application and are given by R_S and R_L loading the primary (source) and secondary (load), respectively.

A simple way to view the double-tuned circuit relies on an equivalent circuit model of the real ($k \neq 1$) transformer shown in Fig. B.1b [76]. In this model, the non-unity coupling between the primary and secondary windings results in an inductance

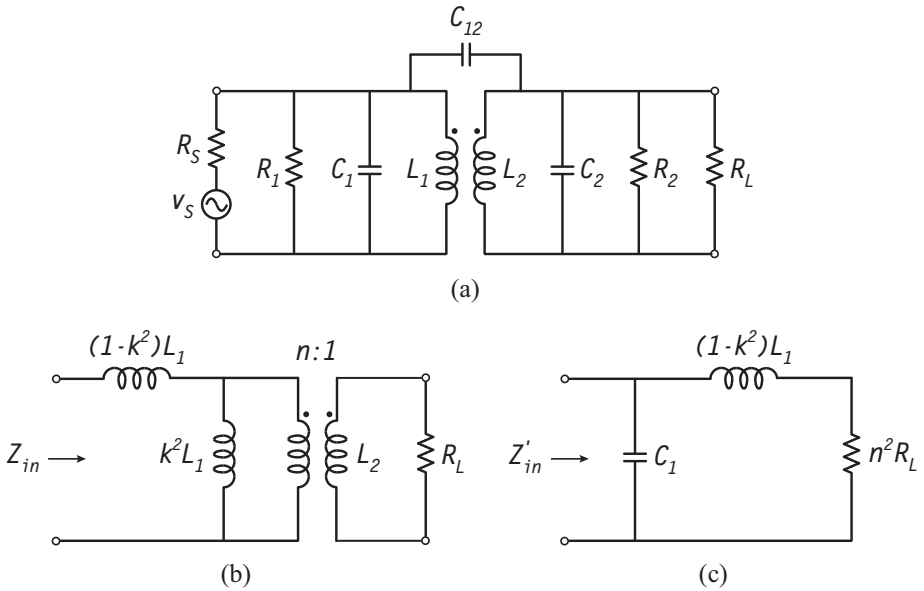

Figure B.1: (a) Lumped-element circuit model of the planar double-tuned transformer. (b) A real transformer ($0 \leq k \leq 1$) equivalent circuit; the transformer in this model is ideal ($k = 1$) with a turns ratio given by (B.1). (c) When the secondary of the double-tuned transformer (a) is resonant, the primary sees the transformed secondary resistance in series with an inductive reactance; this leakage inductance acts as part of an L-C step-up matching network along with C_1.

on each side of the transformer that is uncoupled to the other side. This leakage inductance provides no transformer action, but produces a reactance seen looking into the transformer windings. An analysis of the real transformer results in an expression for the effective transformer turns ratio (n) as a function of coupling factor and the primary and secondary inductances,

$$n = k\sqrt{\frac{L_1}{L_2}}. \tag{B.1}$$

When the secondary is terminated by a pure resistance, or equivalently, the parallel resonant secondary circuit of Fig. B.1a is at resonance, the impedance looking into the

primary sees the transformed secondary load in series with the leakage inductance,

$$Z_{in}(\omega)\Big|_{\omega_0} = j\omega_0(1-k^2)L_1 + n^2R_L \tag{B.2}$$

where $\omega_0 = 1/\sqrt{L_2C_2}$, the resonant frequency of the transformer secondary. (R_1 and R_2 are neglected as they are assumed to be much larger than R_S and R_L and do not affect the resonant frequencies of the primary and secondary circuits.) In terms of admittance,

$$\begin{aligned} Y_{in}(\omega)\Big|_{\omega_0} = &\frac{n^2R_L}{(n^2R_L)^2 + [\omega_0L_1(1-k^2)]^2} \\ &- j\frac{\omega_0L_1(1-k^2)}{(n^2R_L)^2 + [\omega_0L_1(1-k^2)]^2}. \end{aligned} \tag{B.3}$$

The inductive reactance in (B.2) can be canceled by a shunt capacitor across the transformer primary (Fig. B.1c). Equating the admittance of C_1 with the imaginary part of (B.3), the required primary capacitor is given by

$$C_1 = \frac{L_1(1-k^2)}{(n^2R_L)^2 + [\omega_0L_1(1-k^2)]^2}. \tag{B.4}$$

The resulting input impedance Z'_{in} is purely real

$$Z'_{in}(\omega)\Big|_{\omega_0} = n^2R_L + \frac{[\omega_0L_1(1-k^2)]^2}{n^2R_L}. \tag{B.5}$$

Using (B.5), and for $Z'_{in} = R_S$, the needed value of L_1 is given by

$$L_1 = \frac{n}{\omega_0(1-k^2)}\sqrt{R_LR_S - n^2R_L^2}. \tag{B.6}$$

The primary resonance occurs only at one frequency which is assumed to be nearly identical to the secondary resonant frequency. One can use this as a starting point and then tune the resonator center frequencies and loaded Qs to obtain a broader

response with some passband ripple.

In the special case where the resonators are tuned to the same frequency,

$$\omega_1 = 1/\sqrt{L_1 C_1} = \omega_2 = 1/\sqrt{L_2 C_2} = \omega_0$$

and have identical primary and secondary loaded Qs,

$$Q_1^l = \frac{R_S||R_1}{\omega_1 L_1} = Q_2^l = \frac{R_L||R_2}{\omega_2 L_2} = Q^l \tag{B.7}$$

the transformer tuned primary and secondary are critically coupled, giving a maximally-flat transmission response [77, 78]. In this case, the required value of k is given by

$$k = \frac{1}{Q^l} \tag{B.8}$$

and the resulting transformer 3-dB bandwidth is

$$\beta = \frac{\sqrt{2} f_0}{Q^l}. \tag{B.9}$$

Although (B.8) and (B.9) are formulated for the case of $Q^l > 20$, using a Q^l as low as 2.5 results in less than a 10% error in bandwidth and an upward shift in center frequency. Other responses, such as Chebyshev or Bessel transfer functions, are possible by varying k, Q_1^l, Q_2^l, ω_1, and ω_2 [77].

B.2 Design, Fabrication, and Results

A 4:1 transformer at 4 GHz, with load and source terminations of 12.5 Ω and 50 Ω was designed. Full-wave simulations were performed using Sonnet [58] to predict coupling values for stacked inductor geometries. To achieve the widest possible bandwidth with a maximum realizable k of 0.5, the secondary was designed with a Q_2^l

of 1.3. Using (B.7) the required value of L_2 was calculated as 0.40 nH. To resonate at 4 GHz, C_2 was chosen as 3.98 pF. Using (B.4) and (B.1), the needed C_1 was 2.38 pF. Finally, L_1 was calculated as 0.86 nH using (B.6). The circuit was then tuned in simulation for widest bandwidth, with L_1 and C_2 adjusted to 0.80 nH and 3.50 pF. The unloaded Qs of the inductors and capacitors were chosen to establish a total resonator unloaded Q of 15 (based on measured data of inductors and capacitors in the utilized process).

The circuit was fabricated in the M.I.T. Lincoln Laboratory Precision Multi-Chip Module (P-MCM) process. This technology offers three metal signal layers, a metal-insulator-metal (MIM) capacitor layer, a tantalum resistor layer, and tungsten vias (Fig. B.2) [60]. The process has been recently improved by including backside trench etching and a 20 μm thick gold top metal layer, making high-Q suspended inductors possible. Suspended inductors with unloaded Qs of $\sim$30 (at 4 GHz) result in transformers with relatively low insertion loss. The inductors use 20 μm wide lines and 20 μm spacing. Inductor L_1 utilizes the top metal and signal 1 layers and L_2 is made using the signal 2 layer, with the two spirals separated by 7.315 μm of SiO_2. The shunt capacitors use the power and ground plane metal layers separated by 150 nm of Al_2O_3 (see Fig. 4.3). The fabricated circuit is shown in Fig. B.3. The area containing the transformer is 440 μm by 500 μm (roughly $0.02\lambda \times 0.02\lambda$ in Si).

The transformer was measured using an on-wafer probing set-up using a vector network analyzer with 50 Ω ports. A 2-port short-open-load-thru (SOLT) calibration placed the measurement reference planes at the GSG probe tips. The effects of the probe pads were then removed by including -27 fF of capacitance in parallel with each port. Measured S-parameters were then simulated using a combination of 50 Ω and 12.5 Ω ports to examine the transformer's performance in an impedance matching application.

The measured and simulated S-parameters are shown in Fig. B.4. The 10-dB

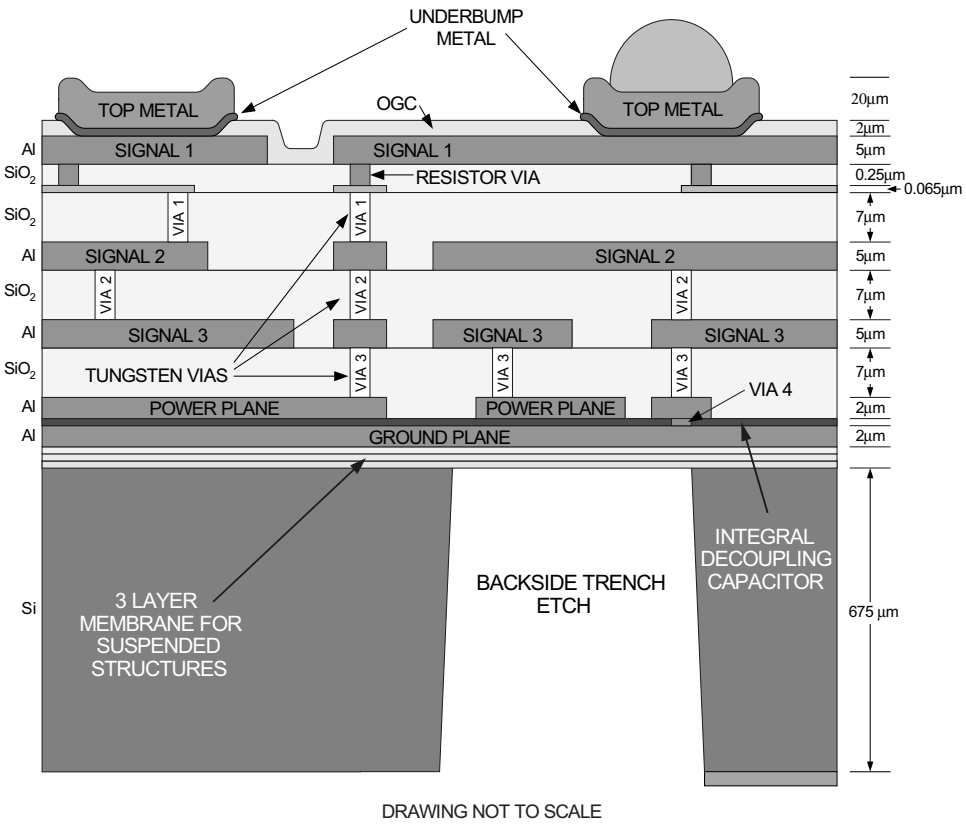

Figure B.2: The Precision Multi-Chip Module (P-MCM) process developed by M.I.T. Lincoln Laboratory.

return loss bandwidth is 30%, with an insertion loss of 1.50 dB at the center frequency of 4.06 GHz and 1.97 dB and 2.05 dB at the band edges of 3.52 GHz and 4.71 GHz respectively. The measured and simulated (model) responses match very well over 1–18 GHz (Fig. B.5).

The electric coupling (C_{12}) produces a transmission zero in the upper stop-band and can be increased with additional lumped capacitance to decrease the zero's frequency and increase the transmission skirt slope above the passband. In this transformer, the zero appears well above 18 GHz, so is not visible in Fig. B.5.

The measured S-parameters were fit to the planar transformer model (Fig. B.1a). The fit circuit element values vary slightly from the design values due to modeling uncertainty and process variation, but agree within 7%. The extracted values are

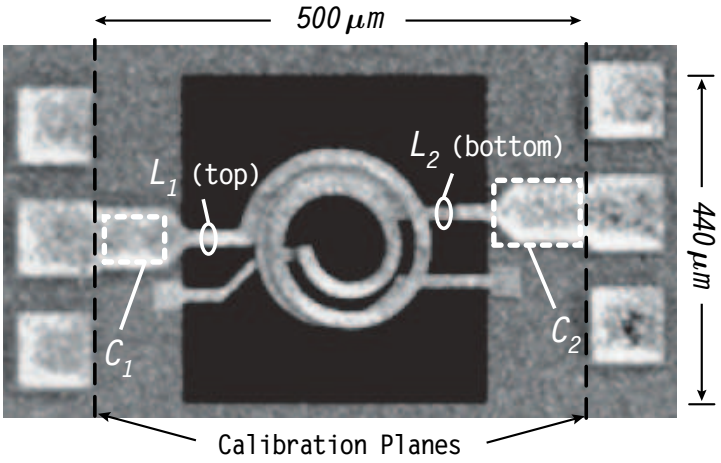

Figure B.3: Die photograph of the double-tuned transformer. Capacitors C_1 and C_2 are not visible below the top metal layer. The backside etching is also not visible as its outline is covered by the remaining ground plane (partial removal of the ground plane layer results in the black rectangle surrounding the transformer windings).

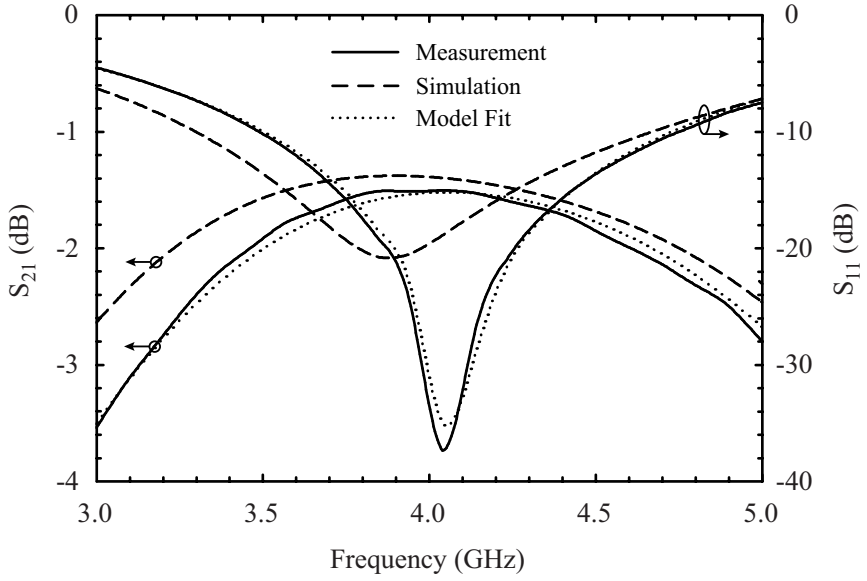

Figure B.4: Measured, simulated, and model fit response of the double-tuned transformer circuit. The primary (R_S) is terminated in 50 Ω while the secondary (R_L) is terminated in 12.5 Ω.

shown in Table B.1.

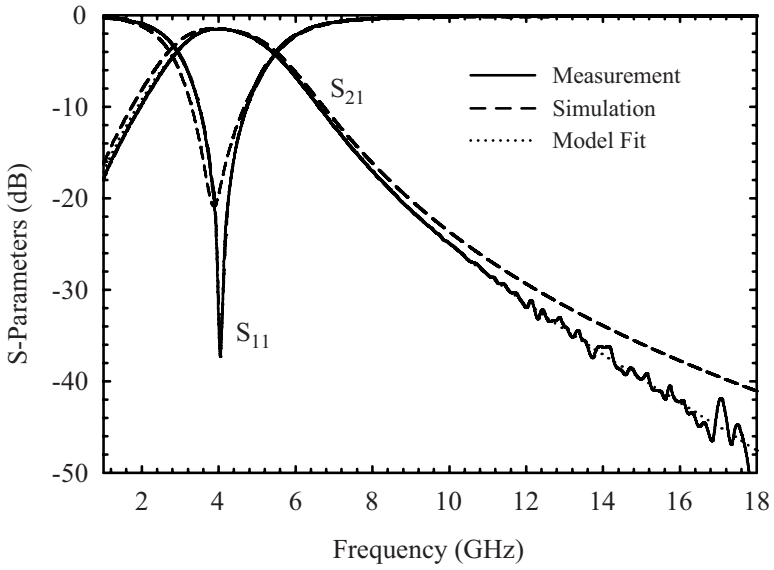

Figure B.5: Wideband response of the double-tuned transformer.

B.3 Conclusion

A state-of-the-art planar double-tuned transformer was presented with a 30% bandwidth centered at 4.06 GHz, with 1.50 dB minimum insertion loss, in a small area (0.22 mm^2). Also, an accurate model and design trade-offs are given which allow the implementation of similar transformers for a wide range of realizable k values (0.1–0.8) typical in RFIC geometries.

Table B.1: Transformer Circuit Model Fit Element Values

Element	Value	Element	Value
k	0.47	C_{12}	40.0 fF
L_1	0.75 nH	R_S	50 Ω
L_2	0.39 nH	R_L	12.5 Ω
R_1	230 Ω	f_1†	3.86 GHz
R_2	110 Ω	f_2†	4.48 GHz
C_1	2.27 pF	Q_1^l	2.3
C_2	3.24 pF	Q_2^l	1.0

†$f_n = \omega_n/2\pi$

Bibliography

[1] C. Kudsia, R. Cameron, and W.-C. Tang, "Innovations in microwave filters and multiplexing networks for communications satellite systems," *IEEE Trans. Microwave Theory Tech.*, vol. 40, no. 6, pp. 1133–1149, Jun. 1992.

[2] G. W. Anderson, D. C. Webb, A. E. Spezio, and J. N. Lee, "Advanced channelization technology for RF, microwave, and millimeterwave applications," in *Proc. IEEE*, vol. 79, no. 3, Mar. 1991, pp. 355–388.

[3] J. H. Collins and P. M. Grant, "A review of current and future components for electronic warfare receivers," *IEEE Trans. Microwave Theory Tech.*, vol. 29, no. 5, pp. 395–403, May 1981.

[4] I. Hunter, L. Billonet, B. Jarry, and P. Guillon, "Microwave filters—applications and technology," *IEEE Trans. Microwave Theory Tech.*, vol. 50, no. 3, pp. 794–805, Mar. 2002.

[5] R. F. Jeffries, R. B. Greed, D. C. Voyce, G. Nudd, R. G. Humphreys, and S. W. Goodyear, "Further development of a future ESM channeliser with high temperature superconducting filters," *IEEE Trans. Applied Superconductivity*, vol. 11, no. 1, pp. 410–413, Mar. 2001.

[6] J. E. Dean and J. D. Rhodes, "Design of MIC broadband contiguous multiplexers," in *IEEE MTT-S International Microwave Symposium Digest*, May 1980, pp. 147–149.

[7] S. G. Kaiser, "Digital receiver technology, architecture, and application," in *IEEE MTT-S International Microwave Symposium Digest*, Jun. 1996, pp. 1331–1334.

[8] H.-M. Seo, C.-G. Woo, and P. Choi, "Relationships between ADC performance and requirements of digital-IF receiver for WCDMA base-station," *IEEE Trans. Vehicular Tech.*, vol. 52, no. 75, pp. 1398–1408, Sep. 2003.

[9] C.-H. Tseng and S.-C. Chou, "Direct downconversion of multiband RF signals using bandpass sampling," *IEEE Trans. Wireless Comm.*, vol. 5, no. 1, pp. 72–76, Jan. 2006.

[10] R. Levy, R. V. Snyder, and G. Matthaei, "Design of microwave filters," *IEEE Trans. Microwave Theory Tech.*, vol. 50, no. 3, pp. 783–793, Mar. 2002.

[11] R. Levy and S. B. Cohn, "A history of microwave filter research, design, and development," *IEEE Trans. Microwave Theory Tech.*, vol. 32, no. 9, pp. 1055–1067, Sep. 1984.

[12] R. M. Fano and A. W. Lawson, *Microwave Transmission Circuits, MIT Radiation Laboratory Series.* New York, NY: McGraw-Hill, 1948, vol. 9, (See chs. 9 and 10).

[13] M. Makimoto and S. Yamashita, *Microwave Resonators and Filters for Wireless Communications*. New York, NY: Springer, 2001.

[14] J. D. Rhodes and R. Levy, "Design of general manifold multiplexers," *IEEE Trans. Microwave Theory Tech.*, vol. 27, no. 2, pp. 111–123, Feb. 1979.

[15] M. Guglielmi, "Simple CAD procedure for microwave filters and multiplexers," *IEEE Trans. Microwave Theory Tech.*, vol. 27, no. 2, pp. 111–123, Feb. 1979.

[16] J. D. Rhodes and R. Levy, "A generalized multiplexer theory," *IEEE Trans. Microwave Theory Tech.*, vol. 27, no. 2, pp. 99–111, Feb. 1979.

[17] G. L. Matthaei, L. Young, and E. Jones, *Microwave Filters Impedance-Matching Networks, and Coupling Structures*. Norwood, MA: Artech House, 1980.

[18] E. G. Cristal and G. L. Matthaei, "A technique for the design of multiplexers having contiguous channels," *IEEE Trans. Microwave Theory Tech.*, vol. 12, no. 1, pp. 88–93, Jan. 1964.

[19] J. D. Rhodes and S. A. Alseyab, "A design procedure for bandpass channel multiplexers connected at a common junction," *IEEE Trans. Microwave Theory Tech.*, vol. 28, no. 3, pp. 246–253, Mar. 1980.

[20] A. García-Lampérez, M. Salazar-Palma, and T. K. Sarkar, "Analytical synthesis of microwave multiport networks," in *IEEE MTT-S International Microwave Symposium Digest*, Jun. 2004, pp. 455–458.

[21] K. D. Breurer and N. Worontzoff, "A low cost multiplexer for channelized receiver front ends at millimeter waves," in *IEEE MTT-S International Microwave Symposium Digest*, May 1980, pp. 150–152.

[22] C. I. Mobbs, "The use of matched four-port filters to realize switched multiplexers having low amplitude and group delay ripple," *IEEE Trans. Microwave Theory Tech.*, vol. 35, no. 12, pp. 1183–1191, Dec. 1987.

[23] R. R. Mansour, "Design of superconductive multiplexers using single-mode and dual-mode filters," *IEEE Trans. Microwave Theory Tech.*, vol. 42, no. 7, pp. 1411–1418, Jul. 1994.

[24] F. S. Coale, "Applications of directional filters for multiplexing systems," *IEEE Trans. Microwave Theory Tech.*, vol. 6, no. 4, pp. 450–453, Mar. 1980.

[25] V. Neubauer, M. Mayer, and G. Magerl, "A novel low loss microwave multiplexer design based on directional filters," in *IEEE Radio and Wireless Conference*, Aug. 2002, pp. 257–260.

[26] W. A. Edson and J. Wakabayashi, "Input manifolds for microwave channelizing filters," *IEEE Trans. Microwave Theory Tech.*, vol. 18, no. 5, pp. 270–276, May 1970.

[27] R. J. Cameron, H. Gregg, C. J. Radcliffe, and J. D. Rhodes, "Extracted-pole filter manifold multiplexing," *IEEE Trans. Microwave Theory Tech.*, vol. 30, no. 7, pp. 1041–1050, Jul. 1982.

[28] R. G. Egri and A. E. Williams, "A contiguous-band multiplexer design," in *IEEE MTT-S International Microwave Symposium Digest*, May 1983, pp. 86–88.

[29] J. W. Bandler, S. Daijavad, and Q. Zhang, "Exact simulation and sensitivity analysis of multiplexing networks," *IEEE Trans. Microwave Theory Tech.*, vol. 34, no. 1, pp. 93–101, Jan. 1986.

[30] G. Tanne, S. Toutain, J. F. Favennec, P. Jarry, and C. Boschet, "Optimal design of contiguous-band output multiplexers (comux)," *Electronics Letters*, vol. 29, no. 19, pp. 1674–1675, Sep. 1993.

[31] M. K. Chahine and G. Carrer, "Optimal design of contiguous band multiplexers," *Electronics Letters*, vol. 30, no. 24, pp. 2050–2052, Nov. 1994.

[32] G. L. Matthaei and E. G. Cristal, "Multiplexer channel-separating units using interdigital and parallel-coupled filters," *IEEE Trans. Microwave Theory Tech.*, vol. 13, no. 3, pp. 328–334, May 1965.

[33] M. Zewani and I. C. Hunter, "Design of ring-manifold microwave multiplexers," in *IEEE MTT-S International Microwave Symposium Digest*, Jun. 2006, pp. 689–692.

[34] G. L. Matthaei, S. M. Rohlfing, and R. J. Forse, "Design of HTS, lumped-element, manifold-type microwave multiplexers," *IEEE Trans. Microwave Theory Tech.*, vol. 44, no. 7, pp. 1313–1321, Jul. 1996.

[35] S. J. Fiedziuszko, J. A. Curtis, S. C. Holme, and R. S. Kwok, "Low loss multiplexers with planar dual mode HTS resonators," *IEEE Trans. Microwave Theory Tech.*, vol. 44, no. 7, pp. 1248–1257, Jul. 1996.

[36] R. R. Mansour, "Microwave superconductivity," *IEEE Trans. Microwave Theory Tech.*, vol. 50, no. 3, pp. 750–759, Mar. 2002.

[37] S. B. Cohn, "Direct-coupled-resonator filters," *Proc. IRE*, vol. 45, no. 2, pp. 187–196, Feb. 1957.

[38] A. E. Atia and A. E. Williams, "Narrow-bandpass waveguide filters," *IEEE Trans. Microwave Theory Tech.*, vol. 20, no. 4, pp. 258–265, Apr. 1972.

[39] S. Bila, D. Baillargeat, M. Aubourg, S. Verdeyme, P. Guillon, F. Seyfert, J. Grimm, L. Baratchart, C. Zanchi, and J. Sombrin, "Direct electromagnetic optimization of microwave filters," *IEEE Microwave Magazine*, vol. 2, no. 1, pp. 46–51, Mar. 2001.

[40] J.-S. Hong and M. J. Lancaster, *Microstrip Filters for RF/Microwave Applications*. New York, NY: Wiley, 2001.

[41] A. García-Lampérez, S. Llorente-Romano, M. Salazar-Palma, and T. K. Sarkar, "Efficient electromagnetic optimization of microwave filters and multiplexers using rational models," *IEEE Trans. Microwave Theory Tech.*, vol. 52, no. 2, pp. 508–521, Feb. 2004.

[42] C. Rauscher, "Logarithmic-periodic contiguous-channel microwave multiplexers," in *IEEE MTT-S International Microwave Symposium Digest*, Jun. 1989, pp. 675–678.

[43] ——, "Logarithmic-periodic microwave multiplexer," U.S. Patent 5 101 181, March 31, 1992.

[44] ——, "Efficient design methodology for microwave frequency multiplexers using infinite-array prototype circuits," *IEEE Trans. Microwave Theory Tech.*, vol. 42, no. 7, pp. 1337–1346, Jul. 1994.

[45] P. Dallos, A. Popper, and R. Fay, "The Cochlea," in *Springer Handbook of Auditory Research*. New York: Springer, 1996, vol. 8.

[46] A. Parthasarathi, "Numerical modeling and electro-acoustic stimulus response analysis for cochlear mechanics," Ph.D. dissertation, The University of Michigan, Ann Arbor, MI, 2000.

[47] C. D. Geisler, *From Sound to Synapse: Physiology of the Mammalian Ear*. New York, NY: Oxford University Press, 1998.

[48] L. Watts, "Cochlear mechanics: Analysis and analog VLSI," Ph.D. dissertation, California Institute of Technology, Pasadena, CA, 1993.

[49] J. Lazzaro and C. Mead, "Circuit models of sensory transduction in the cochlea," in *Analog VLSI Implementation of Neural Networks*, Mead and Ismail, Eds.

[50] S. M. Zhak, S. Mandal, and R. Sarpeshkar, "A proposal for an RF cochlea," in *Proceedings of the Asia Pacific Microwave Conference*, Dec. 2004.

[51] S. Mandal, S. M. Zhak, and R. Sarpeshkar, "Circuits for an RF cochlea," in *IEEE International Symposium on Circuits and Systems Digest*, May 2006, pp. 3610–3613.

[52] C. P. Womack, "The use of exponential transmission lines in microwave components," *IEEE Trans. Microwave Theory Tech.*, vol. 10, no. 2, pp. 124–132, Mar. 1962.

[53] E. de Boer and E. van Bienema, "Solving cochlear mechanics problems with higher-order differential equations," *Journal of the Acoustical Society of America*, vol. 72 (5), pp. 1427–1434, 1982.

[54] A. Parthasarathi, K. Grosh, and A. Nuttall, "Three-dimensional numerical modeling for global cochlear dynamics," *Journal of the Acoustical Society of America*, vol. 107 (1), pp. 474–485, 2000.

[55] T. Ren, "Longitudinal pattern of basilar membrane vibration in the sensitive cochlea," in *Proceedings of the National Academy of Science*, vol. 99, 2002, pp. 17 101–17 106.

[56] L. Robles and M. A. Ruggero, "Mechanics of the mammalian cochlea," *Physiol. Rev.*, vol. 81, pp. 1305–1352, 2001.

[57] *Advanced Design System 2006A*, Agilent Technologies, Inc., Palo Alto, CA, 2006.

[58] *Sonnet 10.52*, Sonnet Software, Inc., North Syracuse, NY, 2005.

[59] C. Galbraith, R. D. White, K. Grosh, and G. M. Rebeiz, "A mammalian cochlea-based RF channelizing filter," in *IEEE MTT-S International Microwave Symposium Digest*, Jun. 2005, pp. 1935–1938.

[60] M. Gouker, K. Konistis, J. Knecht, L. Kushner, and L. Travis, "Multi-layer spiral inductors in a high-precision, fully-planar MCM-D process," in *IEEE MTT-S International Microwave Symposium Digest*, Jun. 2000, pp. 1055–1058.

[61] I. J. Bahl, *Lumped elements for RF and microwave circuits*. Norwood, MA: Artech House, 2003.

[62] C. Galbraith, R. D. White, L. Cheng, K. Grosh, and G. M. Rebeiz, "Cochlea-based RF channelizing filters," *IEEE Transactions on Circuits and Systems I*, vol. (Accepted for publication, August 2007).

[63] C. Galbraith, G. M. Rebeiz, and R. Drangmeister, "A cochlea-based preselector for UWB applications," in *IEEE Radio Frequency Integrated Circuit Symposium Digest*, Jun. 2007, pp. 219–222.

[64] D. Swanson, "Thin-film lumped-element microwave filters," in *IEEE MTT-S International Microwave Symposium Digest*, Jun. 1989, pp. 671–674.

[65] *Modelithics CLR Library*, Modelithics, Inc., Tampa, FL, 2007.

[66] *Temperature Rise Estimations in Rogers High Frequency Circuit Boards Carrying Direct or RF Current*, Rogers Corporation, Chandler, AZ USA.

[67] J.-T. Kuo and E. Shih, "Microstrip stepped impedance resonator bandpass filter with an extended optimal rejection bandwidth," *IEEE Trans. Microwave Theory Tech.*, vol. 51, no. 5, pp. 1554–1559, May 2003.

[68] R. E. Collin, *Foundations for Microwave Engineering*, 2nd ed. New York, NY: McGraw-Hill, 1992.

[69] M. Sagawa, M. Makimoto, and S. Yamashita, "Geometrical structures and fundamental characteristics of microwave stepped-impedance resonators," *IEEE Trans. Microwave Theory Tech.*, vol. 45, no. 7, pp. 1078–1085, Jul. 1997.

[70] M. Makimoto and S. Yamashita, "Bandpass filters using parallel coupled stripline stepped impedance resonators," *IEEE Trans. Microwave Theory Tech.*, vol. 28, no. 12, pp. 1413–1417, Dec. 1980.

[71] H. Uchida, Y. Furukawa, T. Ohwada, N. Yoneda, and M. Miyazaki, "Low-spurious coaxial-line bandpass filter with saucer-loaded stepped-impedance resonators," in *IEEE MTT-S International Microwave Symposium Digest*, Jun. 2002, pp. 1785–1787.

[72] H. Wang and L. Zhu, "Microstrip bandpass filters with ultra-broad rejection band using stepped impedance resonator and high-impedance transformer," in *IEEE MTT-S International Microwave Symposium Digest*, Jun. 2005, pp. 683–686.

[73] A. Abbaspour-Tamijani, "Novel components for integrated millimeter-wave front-ends," Ph.D. dissertation, The University of Michigan, Ann Arbor, MI, 2004.

[74] *MATLAB 7.1*, The Mathworks, Inc., Natick, MA, 2005.

[75] C. J. Galbraith and G. M. Rebeiz, "Higher-order cochlear channelizers," *IEEE Trans. Microwave Theory Tech.*, vol. (Submitted, September 2007).

[76] J. Smith, *Modern Communication Circuits*. New York, NY: McGraw-Hill, 1986.

[77] G. Valley, Jr. and G. Wallman, *Vacuum Tube Amplifiers, MIT Radiation Laboratory Series*. New York, NY: McGraw-Hill, 1948.

[78] C. B. Aiken, "Two mesh tuned coupled circuit filters," *Proc. IRE*, vol. 25, no. 2, pp. 230–272, Feb. 1937.